Washington University in St. Louis

DEPARTMENT OF PHYSICS

Dissertation Examination Committee:
Ralf Wessel, Chair
Mark Alford
Anders Carlsson
Edward Gruberg
Zohar Nussinov
Kurt Thoroughman

ON THE DYNAMICS OF DELAYED NEURAL FEEDBACK LOOPS

by

Sebastian F. Brandt

A dissertation presented to the
Graduate School of Arts and Sciences
of Washington University in Saint Louis
in partial fulfillment of the the
requirements for the degree of
Doctor of Philosophy in Physics

December 2007

Saint Louis, Missouri

Acknowledgments

I am indebted to Ralf Wessel for the opportunity to prepare this dissertation under his supervision. His scientific passion, his broad interdisciplinary knowledge, and his truly encouraging personality have been highly inspiring and enjoyable to me.

Next, I want to thank the other members of my dissertation examination committee: Mark Alford, Anders Carlsson, Edward Gruberg, Zohar Nussinov, and Kurt Thoroughman.

I owe thanks to Axel Pelster for a fruitful collaboration. His advice has been helpful and valuable.

I thank John Clark for his advice and support. I am deeply grateful to Carl Bender for our inspiring collaboration.

I thank Jing Shao, Matthew Caudill, Saurish Chakrabarty, Babette Dellen, and Adam Eggebrecht for good and enjoyable collaborations.

I thank Harald Luksch and Ulrike Meyer for hospitality during a stay at the Rheinisch-Westfälische Technische Hochschule Aachen, Germany during the summer of 2006.

Julia Hamilton, Sarah Hedley, and Sai Iyer have been helpful, and I thank them for their assistance.

Last but not least, I thank my family for their caring support.

Contents

List of Figures

List of Tables

Abstract

The computational potential of neural circuits arises from the interconnections and interactions between their elements. Feedback is a universal feature of neuronal organization and has been shown to be a key element in neural signal processing. In biological neural circuits, delays arise from finite axonal conduction speeds and at the synaptic level due to transmitter release dynamics. In this work, the influence of temporal delay on neural network dynamics is investigated. The basic feedback mechanisms involved in the regulation of neural activity consist of small circuits composed of two to three neurons. We analyze a system of two interconnected neurons and show that finite delays can induce oscillations in the system. Employing a perturbative approach in combination with a resummation scheme, we evaluate the limit cycle dynamics of the system. We show that synchronous oscillations can arise when the delays are asymmetric. Furthermore, distributed delays can stabilize the system and lead to an increased range of parameters for which the system converges to a stable fixed point. We next consider a delayed neural triad with a characteristic topology commonly found in neural feedback circuits. We show that the system can be both robust and sensitive in regard to small parameter changes and examine the significance of the different projections. We then address the functional role of a particular feedback loop found in the visual system of nonmammalian vertebrates. We show that the system can function as a 'winner-take-all' and novelty detector and examine the influence of temporal delays on the system's performance. Biological systems are subject to stochastic influences and display some degree of disorder. We examine the role of noise and its effect on the stability of the synchronized state in a system of two coupled active rotators. Finally, we show that disordering the driving forces in arrays of coupled oscillators can lead to synchronization in these systems.

Chapter 1

Introduction

The computational potential of neural circuits arises from the interconnections and interactions between their elements. Among the cells found in living organisms, neurons are remarkable in their ability to generate electrical signals in response to chemical and other inputs, and transmitting them to other cells. They achieve rapid signal propagation over large distances by generating characteristic electrical pulses called action potentials or spikes, which travel down nerve fibers. Neurons are nonlinear elements, which is evident from the fact that they have a threshold for producing spikes. A weak stimulation may have no effect, while several weak stimuli together can produce an action potential, and thus cause a dramatic change in the neuron's membrane potential.

The nervous systems of higher animals are complex. These intricate networks of synaptic connections among neurons of diverse phenotypes take incoming sensory data, encode them into various biophysical variables, and subsequently perform different operations on these variables to extract relevant features from the input. The outcome of some of these computations is stored for later access and will, ultimately, control the motor output of the animal in various ways [1]. The remarkable effectiveness of biological information processing depends on both the nonlinear response of the neurons and the large connectivity among them [2].

The flow of information in neural circuits is not unidirectional. Rather, feedfoward connections, which bring input to a given region from another region located at an earlier stage along a particular processing pathway, are often paralleled by descending feedback connections. In fact, many neural pathways are dominated by feedback [3]. Often pairs of reciprocally connected regions in the nervous system are spatially separate. For instance, the primate corticothalamic feedback loop

extends over a distance of approximately 100 mm. Thus, for a typical action potential speed of 1 m/s we expect a signal delay of 100 ms. In addition to the delays arising from the propagation of action potentials, delays occur at the synaptic level due to transmitter release dynamics and due to the integration time of post-synaptic potentials at the dendritic tree level where post-synaptic potentials have a finite conduction speed to the soma [4]. It is well-known that time delay can cause an otherwise stable system to oscillate [5–7]. In particular, it has been shown that when signal delays are larger than the neural response time, complex loop dynamics emerge [8–10]. Therefore, finite delays are an essential property of any realistic model of a population of neurons [11].

Nonlinear dynamics is a powerful analytical tool for understanding and predicting behaviors of complex systems. In 1952, Hodgkin and Huxley developed the nonlinear differential equations that explain the generation of action potential in neurons [12]. Since then, dynamical modeling of neural systems has had a history of success. For instance, features of neural rhythmic behavior have been explained and predicted, and many interesting dynamical models of learning and memory have been suggested. Often, the study of bifurcations in neural models and in *in vitro* experiments is a keystone for understanding the dynamical origin of single-neuron and circuit phenomena involved in neural information processing [13].

The equations that arise in the description of the dynamics of complex systems cannot usually be solved in closed form. Fortunately, many different approximation techniques have been developed in order to treat systems that cannot be solved analytically. These methods can be roughly classified into two different categories: numerical methods, which exploit the possibility to rapidly execute calculations on a computer, and analytical approximation methods, where certain assumptions are made in order to simplify the original problem. Numerical methods have proven to be an enormously powerful and successful tool to describe even the most complicated physical scenarios. Nevertheless, the accuracy of numerical methods is not always superior to that of analytical ones, and usually more insight into the underlying system is obtained by means of analytical approximation approaches.

In this work, analytical and computational methods are applied to examine the dynamical behavior of neural feedback loops. Special emphasis is given to the delays present in such systems. Additionally, the effects of noise and disorder on systems of coupled oscillators are investigated. This dissertation contains eight chapters based on the following papers published in scientific jour-

nals, and manuscripts submitted for publication or in preparation:

- Chapter 2: S. F. Brandt, A. Pelster, and R. Wessel, *Variational calculation of the limit cycle and its frequency in a two-neuron model with delay*, Phys. Rev. E **74**, 036201/1-14 (2006).

- Chapter 3: S. F. Brandt, A. Pelster, and R. Wessel, *Synchronization in a neuronal feedback loop through asymmetric temporal delays*, Europhys. Lett. **79**, 38001/1-5 (2007).

- Chapter 4: U. Meyer, J. Shao, S. Chakrabarty, S. F. Brandt, H. Luksch, and R. Wessel, *Distributed delays stabilize neural feedback systems* (submitted). arXiv:0712.0036 [physics.bio-ph].

- Chapter 5: M. Caudill, S. F. Brandt, and R. Wessel, *Dynamics of neural feedback triads with delays* (in preparation).

- Chapter 6: S. F. Brandt and R. Wessel, *Winner-take-all selection in a neural system with delayed feedback*, Biol. Cybern. **97**, 221-228 (2007).

- Chapter 7: S. F. Brandt and R. Wessel, *The isthmotectal feedback loop as a winner-take-all and novelty detection circuit* (in preparation).

- Chapter 8: S. F. Brandt, A. Pelster, and R. Wessel, *Noise-dependent stability of the synchronized state in a coupled system of active rotators* (in preparation).

- Chapter 9: S. F. Brandt, B. K. Dellen, and R. Wessel, *Synchronization from disordered driving forces in arrays of coupled oscillators*, Phys. Rev. Lett. **96**, 034104/1-4 (2006). [1]

Many anatomical, histochemical, and physiological observations show that neurons are incorporated into functional circuits, or modular units [3, 14–16]. The basic feedback mechanisms involved in the regulation of neural activity arise from small neural circuits composed of 2 to 3 neurons [11], which constitute the building blocks out of which larger modular units are constructed. In Chap. 2, we consider a system of two neurons with delayed coupling, where the couplings are of opposite signs. We show that the system of delay differential equations (DDE's) that describes the dynamics of our two-neuron model has a stable stationary point, as long as the sum of the delays does not

---

[1]A reprint of this publication has also been included in: B. K. Dellen, *Computing Visual Context*, Ph.D. thesis, Washington University in St. Louis, 2006.

exceed a critical value. Once the delays are increased beyond this value, the fixed point looses its stability and a stable limit cycle emerges via supercritical Hopf bifurcation. We apply a perturbative approach to evaluate the frequency and trajectory of these oscillations as power series in the delay. The perturbation expansions yield accurate results for delays close to the bifurcation. For delays far away from the bifurcation, however, the perturbative results are useless. Therefore, we apply two different resummation methods to the perturbation expansions in order to obtain results that hold for larger delays. We first apply the Shohat expansion method [17], which allows us to evaluate the frequency of the oscillations and the limit cycle trajectory for larger delays. However, with increasing delays, the accuracy of the Shohat expansion worsens. In order to improve the accuracy of our results, we then apply variational perturbation theory (VPT). This method is based on a variational approach due to Feynman and Kleinert [18], which has been systematically extended to the nonperturbative approximation scheme now called VPT. It is capable of converting divergent weak-coupling into convergent strong-coupling expansions and has been successfully applied in various quantum or statistical field theories [19–22]. A first application of VPT in the field of nonlinear dynamics is found in Ref. [23], while the publication reprinted in Chap. 2 extends the use of VPT for the first time to a system described by DDE's. After the variational resummation of our perturbation expansions, we have very reliable results even in low orders and for large delays for both the angular frequency and the limit cycle of the oscillations.

For simplicity, we take the delays to be equal for both legs of the feedback loop in our model of Chap. 2. In real feedback systems this is not necessarily the case. Indeed, in the isthmotectal feedback loop, a feedback structure in the visual system of nonmammalian vertebrates, which we examine in Chaps. 4 to 7, the axons for the feedforward projection are relatively thin and unmyelinated, whereas they are thick and myelinated for the feedback projection. Since the conduction velocity along unmyelinated axons is 0.1–1.5 m/s, whereas it is 30–50 m/s in myelinated axons [24], it can be expected that the action potential propagation delays for the two directions could differ significantly. Chapter 3 extends the two-neuron model considered in Chap. 2 to the case where the delays are asymmetric. We show that for couplings of opposite signs, asymmetric delays lead to synchronous oscillations in the feedback loop. Employing an approach similar to the procedure in Chap. 2, we first evaluate the phase shift between the oscillations of the two neurons perturbatively. The accuracy of the results that we obtain is only good as long as the sum of the two delays in the

feedback system is close to the bifurcation point, and we again apply VPT to resum our perturbation expansion. The VPT results that we obtain are very accurate even in low orders and for large delays.

The optic tectum (TeO, mammalian homolog: superior colliculus, SC) is the primary visual center in the midbrain of non-mammalian vertebrates. It is reciprocally connected to and strongly affected by a smaller midbrain nucleus called the nucleus isthmi (NI) in nonmammalian and para-bigeminal nucleus in mammalian vertebrates [25]. In the avian visual pathway, the NI consists of three subnuclei: the nucleus pars parvocellularis (Ipc), the nucleus pars magnocellularis (Imc), and the nucleus pars semilunaris [26, 27]. In both Ipc and Imc the projection from the tectum is topo-graphically organized such that the retinotopic map is preserved in both nuclei, with the projection to the Imc being somewhat coarser than for the Ipc. In contrast, the isthmic projections back to the TeO are very different for Ipc and Imc. Ipc neurons project back to the TeO in a precise homotopic manner, i.e., the axons of each Ipc neuron terminate in that part of the optic tectum from which their visual inputs come. Imc, on the other hand, has two populations of neurons. One of the populations makes heterotopic projections onto the TeO whereas the other one projects heterotopically onto the Ipc. Anatomical studies furthermore indicate that a given cell in the Imc does not project back to the locus in the TeO, or to the corresponding locus in the Ipc, from which it receives input, whereas it does project to all other locations [26, 27]. In this sense, the feedback from the Imc can be termed 'antitopographic.'

Experimental results obtained by U. Meyer, J. Shao, H. Luksch, and R. Wessel for the delays between the different components of the isthmotectal feedback loop are given in Chap. 4. These results show that the delays in the isthmic system exhibit considerable variability. We therefore extend our two-neuron model from Chaps. 2 and 3 to accommodate the case of distributed delays in Chap. 4. In this approach, the model can be considered to describe the interactions between two populations of neurons. We model the distribution of the delays with a Gamma distribution, which is characterized by its mean and standard deviation. We show that the introduction of nonzero variance in the delays leads to increased stability of the system, in the sense that the mean delay at which the fixed point of the system looses its stability grows with increasing standard deviation of the delay distribution. We demonstrate that this increased stability can be attributed to the contribution from shorter delays in the Gamma distribution.

In Chap. 5, we consider a three-neuron system representing the feedback system between TeO,

Ipc, and Imc. As pointed out above, this topology consists of two delayed feedback loops with an asymmetric lateral connection between them. We observe that this feedback triad topology appears to have evolved independently in different vertebrate neural feedback circuits. A simple model in terms of finite difference equations of the feedback triad has five connection strength parameters. We show that, under certain circumstances, the system dynamics depend only on two effective parameters that are given by algebraic combinations of subsets of the five original parameters. Thus, equivalent system dynamics can be observed with widely differing parameter settings. When the lateral connection between the two elements of the feedback loop is not present, one of the effective parameters vanishes and geometrical convergence to a fixed point occurs for many choices of the synaptic strengths. The parameter space of synaptic weights in the feedback triad has regions with robustness towards parameter changes, where shifts in the weights do not lead to changes in the activity state of the circuit. However, the parameter space also contains regions in which small changes in synaptic strength lead to drastically different network activity. This is reminiscent, of neural central pattern generators, which are small microcircuits capable of producing rhythmic outputs without rhythmic sensory inputs [28, 29]. The activity states of these circuits can be changed by sensory afferents and neuromodulators making the circuits multifunctional and dynamically plastic [30].

Chapter 6 contains a computational study of the isthmotectal feedback loop in regard to its functioning as a 'winner-take-all' (WTA) network. In models of selective visual attention, the stimulus is encoded in a 'saliency map' that topographically represents the conspicuity of the stimulus over the visual scene. The most salient location is then chosen by a WTA network, i.e., by a neurally implemented maximum detector [31]. The isthmotectal feedback loop has been conjectured to perform WTA selection by different authors [32, 33]. However, divergent views of which elements in the isthmic system mediate excitation or inhibition were expressed. In Chap. 6 these different scenarios are studied and their efficiency for WTA selection is evaluated. We show that the delays in the feedback loop can be crucial, as they may induce WTA behavior to the circuit.

The investigation presented in Chap. 6 employs a model for the neuronal firing rates. In Chap. 7 we use a spiking-neuron model to further examine under what circumstances the isthmotectal feedback loop can function as a WTA system. Furthermore, recent results [34] that demonstrate the sensitivity of the isthmic system to novel stimuli are taken into account. Our neural network model contains a large number of free parameters. We restrict some of these parameters according to re-

sults obtained in anatomical and electrophysiological experiments. The remaining free parameters are then optimized by applying a genetic algorithm. Our algorithm uses the performance of the network model in a WTA and novelty detection task as a fitness function for the optimization procedure. We show that for optimized parameter values the isthmotectal feedback network can perform the specified WTA and novelty detection tasks almost perfectly. Examining the convergence of the algorithm to certain regions of the parameter space, we demonstrate what relative combinations of different parameters can be expected in the biological system. We compare these findings with available experimental data.

A common feature of both biological and model neurons is that sufficiently strong input causes them to fire periodically; the neuron displays oscillatory activity. For subthreshold inputs, on the other hand, the neuron is quiescent. When a subthreshold input is combined with a noisy input, however, the neuron will be pushed above threshold from time to time and fire spikes in a stochastic manner. In this regime, the neuron acts as an excitable element. The dynamics of such a system can be described by the active rotator model developed by Kuramoto and coworkers [35, 36]. In Chap. 8 we examine the influence of noise in a system of two coupled active rotators. Depending on both the coupling strength and the noise, the two rotators can be in a synchronized or desynchronized state. We distinguish between the two states by considering the probability density of the system that we obtain as the stationary solution to the corresponding Fokker-Planck equation. The synchronized state of the system is most stable for intermediate noise intensity in the sense that the coupling strength required to desynchronize the system is maximal at this noise level. We evaluate the phase boundary between synchronized and desynchronized states through numerical and analytical calculations.

Networks of coupled nonlinear oscillators provide useful model systems for the study of a variety of phenomena in physics and biology [37]. Among many others, examples from physics include solid-state lasers [38] and coupled Josephson junctions [39, 40]. In biology, the central nervous system can be described as a complex network of oscillators [41], and cultured networks of heart cells are examples of biological structures with strong nearest-neighbor coupling [42]. In particular, the emergence of synchrony in such networks has received increased attention in recent years [43, 44]. Disorder and noise in physical systems tend to destroy spatial and temporal regularity. However, in nonlinear systems, often the opposite effect is found and intrinsically noisy processes, such as ther-

mal fluctuations or mechanically randomized scattering, lead to surprisingly ordered patterns [45]. In Chap. 9 we consider an array of coupled oscillators. When driven synchronously, i.e., all driving forces have the same phase, the networks display chaotic dynamics. We show that random phases in the driving forces result in regular, periodic network behavior. Intermediate phase disorder can produce network synchrony. Specifically, there is an optimal amount of phase disorder, which can induce the highest level of synchrony. These results demonstrate that the spatiotemporal structure of external influences can control chaos and lead to synchronization in nonlinear systems.

References

[1] C. Koch, *Biophysics of Computation: Information Processing in Single Neurons* (Oxford Univ. Press, New York, 1999).

[2] J. J. Hopfield and D. W. Tank, Biol. Cybern. **52**, 141 (1985).

[3] G. M. Shepherd, *The Synaptic Organization of the Brain* (Oxford Univ. Press, New York, 2003).

[4] C. W. Eurich, M. C. Mackey, and H. Schwegler, J. Theor. Bio. **216**, 31 (2002).

[5] U. an der Heiden, J. Math. Bio. **8**, 345 (1979).

[6] B. D. Coleman and G. H. Renninger, SIAM J. Appl. Math. **31**, 111 (1976); J. Theor. Bio. **51**, 243 (1975).

[7] K. P. Hadeler and J. Tomiuk, Arch. Rat. Mech. Anal. **65**, 87 (1977).

[8] J. Foss, A. Longtin, B. Mensour, and J. Milton, Phys. Rev. Lett. **76**, 708 (1996).

[9] J. Foss, F. Moss, and J. Milton, Phys. Rev. E **55**, 4536 (1997).

[10] J. Foss and J. Milton, J. Neurophysiol. **84**, 975 (2000).

[11] J. Milton, *Dynamics of Small Neural Populations* (Amer. Math. Soc., Providence, 1996).

[12] A. L. Hodgkin and A. F. Huxley, J. Physiol. **117**, 500 (1952).

[13] M. I. Rabinovich, P. Varona, A. I. Selverston, and H. D. I. Abarbanel, Rev. Mod. Phys. **78**, 1213 (2006).

[14] M. Abeles, *Corticonics: Neural Circuits of the Cerebral Cortex* (Cambridge Univ. Press, New York, 1991).

[15] A. Brodal, *Neurological Anatomy in Relation to Clinical Medicine* (Oxford Univ. Press, New York, 1981).

[16] E. L. White, *Cortical Circuits: Synaptic Organization of the Cerebral Cortex – Structure, Function, and Theory* (Birkäuser, Boston, 1989).

[17] J. Shohat, J. App. Phys. **14**, 568 (1943).

[18] R. P. Feynman and H. Kleinert, Phys. Rev. A **34**, 5080 (1986).

[19] H. Kleinert, Phys. Lett. A **173**, 332 (1993).

[20] H. Kleinert, *Path Integrals in Quantum Mechanics, Statistics, Polymer Physics, and Financial Markets*, Third Edition (World Scientific, Singapore, 2004); Phys. Rev. D **57**, 2264 (1998).

[21] H. Kleinert and V. Schulte-Frohlinde, *Critical Properties of Φ^4-Theories* (World Scientific, Singapore, 2001); Chap. 19.

[22] W. Janke, A. Pelster, H.-J. Schmidt, and M. Bachmann (Eds.), *Fluctuating Paths and Fields – Dedicated to Hagen Kleinert on the Occasion of his 60th Birthday* (World Scientific, Singapore, 2001).

[23] A. Pelster, H. Kleinert, and M. Schanz, Phys. Rev. E **67**, 016604 (2003).

[24] J. E. Desmedt and G. Cheron, Electro. Clin. Electroencephalog. **50**, 382 (1980).

[25] E. Gruberg, E. Dudkin, Y. Wang Y, G. Marín, C. Salas, E. Sentis, J. C. Letelier, J. Mpodozis, J. Malpeli, H. Cui, R. Ma, D. Northmore, and S. Udin, J. Neurosci. **26** 10368 (2006).

[26] Y. Wang, D. E. Major, and H. J. Karten, J. Comp. Neurol. **469**, 275 (2004).

[27] Y. Wang, H. Luksch, N. C. Brecha, and H. J. Karten, J. Comp. Neurol. **494**, 7 (2006).

[28] E. Marder and R. L. Calabrese, Physiol. Rev. **76**, 687 (1996).

[29] S. G. Stein, S. Grillner, A. I. Selverston, and G. S. Douglas (Eds.), *Neurons, Networks, and Motor Behavior* (MIT Press, Cambridge, 1997).

[30] P. Goldman-Rakic, Neuron **14**, 477 (1995).

[31] C. Koch and S. Ullman, Hum. Neurobiol. **4**, 219 (1985).

[32] G. Marín, J. Mpodozis, E. Sentis, T. Ossandón, and J. C. Letelier, J. Neurosci. **25**, 7081 (2005).

[33] S.-R. Wang, Brain. Res. Rev. **41**, 13, (2003).

[34] G. Marín, C. Salas, E. Sentis, X. Rojas, J. C. Letelier, and J. Mpodozis, J. Neurosci. **27**, 8112 (2007).

[35] S. Shinomoto and Y. Kuramoto, Prog. Theor. Phys. **75**, 1105 (1986).

[36] H. Sakaguchi, S. Shinomoto, and Y. Kuramoto, Prog. Theor. Phys. **79**, 600 (1988).

[37] J. F. Heagy, T. L. Carroll, and L. M. Pecora, Phys. Rev. E **50**, 1874 (1994) and references therein.

[38] R. Roy and K. S. Thornburg, Jr., Phys. Rev. Lett. **72**, 2009 (1994).

[39] A.V. Ustinov, M. Cirillo, and B. Malomed, Phys. Rev. B **47**, 8357 (1993).

[40] K. Wiesenfeld, P. Colet, and S. H. Strogatz, Phys. Rev. Lett. **76**, 404 (1996).

[41] D. Amit, *Modelling Brain Function* (Cambridge Univ. Press, Cambridge, UK, 1989); J. Hertz, A. Krogh, and R. Palmer, *Introduction to the Theory of Neural Computation* (Addison-Wesley, Redwood City, 1991).

[42] Y. Soen, N. Cohen, D. Lipson, and E. Braun, Phys. Rev. Lett. **82**, 3556 (1999).

[43] A. Pikovsky, M. Rosenblum, and J. Kurths, *Synchronization: A Universal Concept in Nonlinear Sciences* (Cambridge Univ. Press, Cambridge, 2003).

[44] S. Strogatz, *Sync: The Emerging Science of Spontaneous Order* (Hyperion, New York, 2003).

[45] T. Shinbrot and F. J. Muzzio, Nature (London) **410**, 251 (2001).

Chapter 2

Variational calculation of the limit cycle and its frequency in a two-neuron model with delay

We consider a model system of two coupled Hopfield neurons, which is described by delay differential equations taking into account the finite signal propagation and processing times. When the delay exceeds a critical value, a limit cycle emerges via a supercritical Hopf bifurcation. First, we calculate its frequency and trajectory perturbatively by applying the Poincaré-Lindstedt method. Then, the perturbation series are resummed by means of the Shohat expansion in good agreement with numerical values. However, with increasing delay, the accuracy of the results from the Shohat expansion worsens. We thus apply variational perturbation theory (VPT) to the perturbation expansions to obtain more accurate results, which moreover hold even in the limit of large delays.

2.1 Introduction

Feedback in biological systems has received increased attention in recent years [1]. In particular, the role of delayed recurrent loops in models of population dynamics, epidemiology, physiology, immunology, neural networks, and cell kinetics has been studied extensively [2]. Neural network

systems are complex and large-scale nonlinear dynamical systems, and the dynamics of a delayed network are yet richer and more complicated [3]. Hopfield [4] proposed a simplified model of a neural network in which each neuron is represented by a linear circuit consisting of a resistor and a capacitor, coupled to other neurons via nonlinear sigmoidal activation functions. From this model, he derived a system of first-order ordinary differential equations to describe the network dynamics. Extending Hopfield's model, Marcus and Westervelt [5] considered the effect of including a temporal delay in the model to account for finite propagation and signal processing times.

In networks of real neurons, delays occur at the synaptic level due to transmitter release dynamics and the integration time of post-synaptic potentials at the dendritic tree level where post-synaptic potentials have a finite conduction speed to the soma, and in the axons due to the finite axonal conduction speed of action potentials [6]. It is well-known that time delay can cause an otherwise stable system to oscillate [7–9] and may lead to bifurcation scenarios resulting in chaotic dynamics [10, 11]. On the other hand, delayed feedback permits the control of chaos [12], where it can be used to stabilize unstable periodic orbits in chaotic attractors [13, 14]. Experimentally, time-delayed chaos control was successfully applied, for instance, to electronic oscillators [15], mechanical pendula [16], lasers [17], and chemical systems [18]. Furthermore, a recently proposed scheme for the treatment of neurological disorders employs delayed feedback in order to efficiently desynchronize the activity of oscillatory neurons [19]. Therefore, finite delays are an essential property of any realistic model of a neuron population [20].

In the vast majority of cases, information about a physical system can only be obtained by means of numerical or analytical approximation methods. Numerical methods constitute a powerful and effective tool to describe even extremely complicated physical scenarios. Nevertheless, their accuracy is not always superior to that of analytical approximations, and usually more insight into the physical principles that govern the system is obtained by pursuing an analytical approach. Often, perturbation expansions are easily accessible, but they are usually divergent and need resummation. A recently developed, powerful method to perform such a resummation is variational perturbation theory (VPT), which has been successfully applied in various quantum or statistical field theories [21–25]. A first application of VPT in the field of deterministic nonlinear dynamics is found in Ref. [26], while the present work extends the use of VPT for the first time to a system described by delay differential equations (DDE's).

In Sect. 2.2, we introduce the two-neuron model and the system of DDE's that we consider. The results of a linear stability analysis of the model system are reported in Sect. 2.3, and it is shown that a limit cycle emerges via a supercritical Hopf bifurcation when the delay exceeds a critical value. In Sect. 2.4, the Poincaré-Lindstedt Method is applied to derive the perturbation expansions for the delay-induced limit cycle and its angular frequency. In Sect. 2.5, we apply the Shohat expansion to the perturbation series of the limit cycle and its angular frequency as a first crude resummation approach. In Sect. 2.6, we resum the perturbation expansions using VPT, which allows us to improve the quality of our results significantly and to obtain results which are reasonable even in the limit of large delays.

2.2   Model

Neural circuits composed of two or three neurons form the basic feedback mechanisms involved in the regulation of neural activity [20]. Many researchers have used bifurcation analysis and numerical simulations in order to analyze a system of two Hopfield-like neurons with discrete or distributed time delays [27–35]. In this investigation, we apply analytical approximation methods to a two-neuron system with delay, described by the coupled first-order DDE's

$$\begin{aligned}
\frac{du_1(t)}{dt} &= -u_1(t) + a_1 \tanh[u_2(t - \tau^{(2)})] \\
\frac{du_2(t)}{dt} &= -u_2(t) + a_2 \tanh[u_1(t - \tau^{(1)})].
\end{aligned} \tag{2.1}$$

Here, u_1 and u_2 denote the voltages of the Hopfield neurons and $\tau^{(1)}$ and $\tau^{(2)}$ are the signal propagation or processing time delays, while a_1 and a_2 describe the couplings between the two neurons.

2.3   Linear Stability Analysis

The system of DDE's (2.1) has a trivial stationary point at $u_1 = u_2 = 0$ and we first analyze its stability. Near the equilibrium point, linearizing the DDE system yields

$$\begin{aligned}
\dot{u}_1(t) &= -u_1(t) + a_1 u_2(t - \tau^{(2)}), \\
\dot{u}_2(t) &= -u_2(t) + a_2 u_1(t - \tau^{(1)}).
\end{aligned} \tag{2.2}$$

Setting

$$\mathbf{u}(t) = e^{\lambda t} \begin{pmatrix} c_1 \\ c_2 \end{pmatrix} \tag{2.3}$$

in the last equation, where λ is a complex number, and c_1 and c_2 are constants, we get a nontrivial solution if and only if

$$(\lambda + 1)^2 - a_1 a_2 e^{-\lambda(\tau^{(1)} + \tau^{(2)})} = 0 \,. \tag{2.4}$$

This equation has been analyzed in detail in Ref. [28]. For $a_1 a_2 \leq -2$ the conditions of Theorem 2 in Ref. [28] are met. Defining $\tau = (\tau^{(1)} + \tau^{(2)})/2$ and

$$\tau_j \equiv \frac{1}{2\omega_0} \left[\sin^{-1} \left(-\frac{2\omega_0}{a_1 a_2} \right) + 2j\pi \right] \,, \qquad j = 0,\, 1,\, 2,\, \cdots, \tag{2.5}$$

where $\omega_0 = \sqrt{|a_1 a_2| - 1}$, this theorem states that:

- If $\tau \in [0,\, \tau_0)$, then the zero solution of (2.1) is asymptotically stable.

- If $\tau > \tau_0$, then the zero solution of (2.1) is unstable.

- τ_j, with $j = 0,\, 1,\, 2 \cdots$, are Hopf bifurcation values of (2.1).

Furthermore, Theorem 3 in Ref. [28] states that the Hopf bifurcation at $\tau = \tau_0$ is supercritical. Note that $i\omega_0$ is the solution to (2.4) when $\tau = \tau_0$, and the period of the limit cycle at the Hopf bifurcation is thus $T_0 = 2\pi/\omega_0$.

2.4 Poincaré-Lindstedt Method

Figure 2.1 shows numerical solutions of the system of DDE's (2.1) for the two cases in which the delay τ is either smaller or greater than its critical value. Below the critical value τ_0 of the delay τ no periodic solution exists, while above $\tau = \tau_0$ there is such a solution. We now consider the case $\tau^{(1)} = \tau^{(2)} = \tau$, $a_1 a_2 \leq -2$ and seek to calculate the period and trajectory of the periodic solution approximately. To this end, we apply the Poincaré-Lindstedt method [36]. Since a supercritical

a)

b)
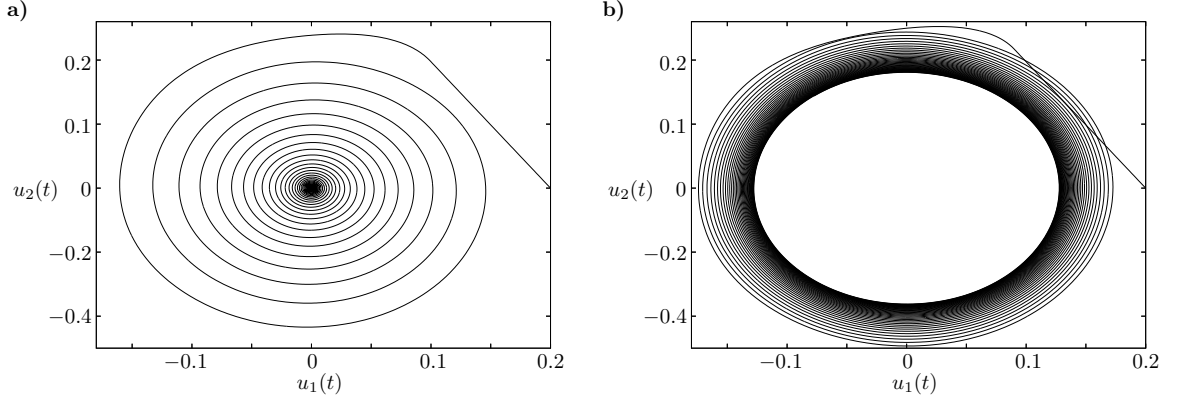
Figure 2.1: Numerical solutions of the system of DDE's (2.1) with $a_1 = -1$, $a_2 = 2$ and $\tau^{(1)} = \tau^{(2)} = \tau$. For this choice of parameters, the critical value of the delay is $\tau_0 = \pi/4 \approx 0.7854\ldots$. In **(a)** the delay is $\tau = 0.7$, and the origin is a stable fixed point. In **(b)** the delay exceeds the critical value: $\tau = 0.8$. In this case, the origin is unstable and the trajectory approaches a limit cycle. In both cases the initial conditions are $u_1(t) = 0.2$, $u_2(t) = 0$ for $t \in [-\tau, 0]$.

Hopf bifurcation occurs at $\tau = \tau_0$, we assume that the amplitude and frequency of the new periodic states are analytic in $\epsilon = \sqrt{\tau - \tau_0}$ and expand them as

$$
\begin{aligned}
\mathbf{u}(t) &= \epsilon \mathbf{U}(t) = \epsilon \left[\mathbf{U}^{(0)}(t) + \epsilon \mathbf{U}^{(1)}(t) + \cdots \right], &\quad (2.6)\\
\omega(\epsilon) &= \omega_0 + \epsilon \omega_1 + \epsilon^2 \omega_2 + \cdots. &\quad (2.7)
\end{aligned}
$$

It is convenient to rescale the argument of these functions so that they become periodic with period 2π. We thus introduce the new independent variable ξ according to $\xi = \omega(\epsilon)t$, and we write $\mathbf{U}(t) = \mathbf{V}(\xi)$, Applying the perturbation expansion (2.6) to the system of DDE's (2.1) and performing this change of variables, we obtain

$$
\begin{aligned}
\omega(\epsilon)\frac{dV_1(\xi)}{d\xi} &= -V_1(\xi) + \frac{a_1}{\epsilon}\tanh\left\{ \epsilon V_2[\xi - \alpha(\epsilon)] \right\}, \\
\omega(\epsilon)\frac{dV_2(\xi)}{d\xi} &= -V_2(\xi) + \frac{a_2}{\epsilon}\tanh\left\{ \epsilon V_1[\xi - \alpha(\epsilon)] \right\},
\end{aligned} \quad (2.8)
$$

in which

$$
\alpha(\epsilon) = \omega(\epsilon)\tau = \omega(\epsilon)(\tau_0 + \epsilon^2) = \omega_0\tau_0 + \epsilon\omega_1\tau_0 + \epsilon^2(\omega_0 + \omega_2\tau_0) + \cdots. \quad (2.9)
$$

The delayed variable $V_{1/2}[\xi - \alpha(\epsilon)]$ is written as

$$\mathbf{V}[\xi - \alpha(\epsilon)] = \mathbf{V}^{(0)}(\xi, \alpha) + \epsilon \mathbf{V}^{(1)}(\xi, \alpha) + \cdots, \tag{2.10}$$

corresponding to the expansion in (2.6), which is equivalent to

$$\mathbf{V}(\xi) = \mathbf{V}^{(0)}(\xi) + \epsilon \mathbf{V}^{(1)}(\xi) + \cdots. \tag{2.11}$$

In order to take into account (2.9), each term in the expansion of $\mathbf{V}(\xi - \alpha)$ is expanded as a Taylor series:

$$\mathbf{V}^{(j)}(\xi, \alpha) = \mathbf{V}^{(j)}(\xi - \omega_0 \tau_0) - \epsilon \omega_1 \tau_0 \left. \frac{d\mathbf{V}^{(j)}(\xi')}{d\xi'} \right|_{\xi' = \xi - \omega_0 \tau_0} + \cdots. \tag{2.12}$$

Applying the expansions for $\mathbf{V}(\xi)$ and $\mathbf{V}(\xi - \alpha)$ to (2.8) we obtain to zeroth order in ϵ

$$
\begin{aligned}
\frac{dV_1^{(0)}(\xi)}{d\xi} &= -\frac{V_1^{(0)}(\xi)}{\omega_0} + \frac{a_1}{\omega_0} V_2^{(0)}(\xi - \omega_0 \tau_0), \\
\frac{dV_2^{(0)}(\xi)}{d\xi} &= -\frac{V_2^{(0)}(\xi)}{\omega_0} + \frac{a_2}{\omega_0} V_1^{(0)}(\xi - \omega_0 \tau_0).
\end{aligned}
\tag{2.13}
$$

Imposing the initial conditions $V_1^{(0)}(0) = A_0$, $V_2^{(0)}(0) = B_0$ on the periodic solution $\mathbf{V}^{(0)}(\xi)$, we find the general solution to the system of homogeneous differential equations (2.13) as

$$
\begin{aligned}
V_1^{(0)}(\xi) &= A_0 \cos \xi + B_0 a_1 \sin(\omega_0 \tau_0) \sin \xi, \\
V_2^{(0)}(\xi) &= B_0 \cos \xi - \frac{A_0}{a_1 \sin(\omega_0 \tau_0)} \sin \xi.
\end{aligned}
\tag{2.14}
$$

The periodic solution $\mathbf{V}(\xi)$ to (2.8) can only be determined up to an arbitrary phase. Without loss of generality we can thus choose $B_0 = 0$ in (2.14), which fixes the phase of the zeroth order solution, at least up to a shift of π.

In general, to order ϵ^n, we have to solve the system of differential equations

$$\frac{dV_1^{(n)}(\xi)}{d\xi} = -\frac{V_1^{(n)}(\xi)}{\omega_0} + \frac{a_1}{\omega_0} V_2^{(n)}(\xi - \omega_0 \tau_0) + f_1^{(n)}(\xi),$$

$$\frac{dV_2^{(n)}(\xi)}{d\xi} = -\frac{V_2^{(n)}(\xi)}{\omega_0} + \frac{a_2}{\omega_0} V_1^{(n)}(\xi - \omega_0\tau_0) + f_2^{(n)}(\xi), \tag{2.15}$$

where the inhomogeneity $\mathbf{f}^{(n)}(\xi)$ is determined by the solutions to previous orders. Since we require that the solution $\mathbf{V}^{(n)}(\xi)$ be periodic in ξ with period 2π, we can impose certain conditions on the inhomogeneity $\mathbf{f}^{(n)}(\xi)$. Namely, we demand that $\mathbf{f}^{(n)}(\xi)$ not contain terms that would lead to non-periodic solutions for $\mathbf{V}^{(n)}(\xi)$, i.e., $\mathbf{f}^{(n)}(\xi)$ must not contain secular terms. In order to identify the conditions that must be satisfied by $\mathbf{f}^{(n)}(\xi)$, we expand $\mathbf{V}^{(n)}(\xi)$ and $\mathbf{f}^{(n)}(\xi)$ as Fourier series:

$$\begin{pmatrix} V_1^{(n)}(\xi) \\ V_2^{(n)}(\xi) \end{pmatrix} = \sum_{k=1}^{\infty} \left[\begin{pmatrix} a_{1,k}^{(n)} \\ a_{2,k}^{(n)} \end{pmatrix} \cos k\xi + \begin{pmatrix} b_{1,k}^{(n)} \\ b_{2,k}^{(n)} \end{pmatrix} \sin k\xi \right], \tag{2.16}$$

$$\begin{pmatrix} f_1^{(n)}(\xi) \\ f_2^{(n)}(\xi) \end{pmatrix} = \sum_{k=1}^{\infty} \left[\begin{pmatrix} \alpha_{1,k}^{(n)} \\ \alpha_{2,k}^{(n)} \end{pmatrix} \cos k\xi + \begin{pmatrix} \beta_{1,k}^{(n)} \\ \beta_{2,k}^{(n)} \end{pmatrix} \sin k\xi \right]. \tag{2.17}$$

By inserting the expansions (2.16), (2.17) into the systems of equations (2.15), we find that the coefficient of the the terms with $k = 1$ in the inhomogeneity $\mathbf{f}^{(n)}(\xi)$ must satisfy the conditions

$$a_2 \sin(\omega_0\tau_0)\alpha_{1,1}^{(n)} + \beta_{2,1}^{(n)} = 0, \tag{2.18}$$

$$\alpha_{2,1}^{(n)} - a_2 \sin(\omega_0\tau_0)\beta_{1,1}^{(n)} = 0. \tag{2.19}$$

The derivation of these two conditions is demonstrated in the appendix.

After this general result, we now consider the first-order expansion of the system (2.8). Taking into account the result (2.14) and the choice $B_0 = 0$, we obtain the inhomogeneity $\mathbf{f}^{(1)}$ to be given by

$$f_1^{(1)}(\xi) = A_0\omega_1 \left(\tau_0 \cos\xi + \frac{1+\tau_0}{\omega_0} \sin\xi \right) \tag{2.20}$$

and

$$f_2^{(1)}(\xi) = -A_0\omega_1 \left[\frac{a_2(1+\tau_0)}{\omega_0} \sin(\omega_0\tau_0) \cos\xi + \frac{\tau_0}{a_1 \sin(\omega_0\tau_0)} \sin\xi \right]. \tag{2.21}$$

Thus, according to the conditions (2.18), (2.19), we must demand

$$-\frac{2A_0\omega_1\tau_0}{a_1\sin^2(\omega_0\tau_0)} = 0 \qquad \text{and} \qquad -\frac{4A_0\omega_1(1+\tau_0)}{a_1\sin(2\omega_0\tau_0)} = 0\,. \tag{2.22}$$

We must thus have either $A_0 = 0$ or $\omega_1 = 0$. If we choose $A_0 = 0$, we only obtain the trivial solution. Thus, we choose $\omega_1 = 0$, and the coefficient A_0 is yet to be determined. The solution for $\mathbf{V}^{(1)}(\xi)$ is then simply given by the solution to the homogeneous system:

$$
\begin{aligned}
V_1^{(1)}(\xi) &= A_1\cos\xi\,, \\
V_2^{(1)}(\xi) &= -\frac{A_1}{a_1\sin(\omega_0\tau_0)}\sin\xi\,,
\end{aligned}
\tag{2.23}
$$

where A_1 is to be determined in higher orders.

Expanding (2.8) up to order ϵ^2 while taking into account the zeroth- and first-order result, we obtain the inhomogeneity $\mathbf{f}^{(2)}(\xi)$ as given by the expansion (2.17). For the first component we have

$$
\begin{aligned}
\alpha_{1,1}^{(2)} &= -\frac{A_0^3(1+\omega_0^2)}{4a_1^2\omega_0} + A_0(\omega_0 + \tau_0\omega_2)\,, \\
\beta_{1,1}^{(2)} &= \frac{A_0^3(1+\omega_0^2)}{4a_1^2} + \frac{A_0(1+\tau_0)\omega_2}{\omega_0} + A_0\,, \\
\alpha_{1,3}^{(2)} &= \frac{A_0^3(3\omega_0^2-1)}{12a_1^2}\,, \\
\beta_{1,3}^{(2)} &= \frac{A_0^3(3-\omega_0^2)}{12a_1^2}\,.
\end{aligned}
\tag{2.24}
$$

And for the second component we have

$$
\begin{aligned}
\alpha_{2,1}^{(2)} &= -a_2\sin(\omega_0\tau_0)\left[\frac{A_0^3}{4} + \frac{A_0(1+\tau_0)\omega_2}{\omega_0} + A_0\right]\,, \\
\beta_{2,1}^{(2)} &= -a_2\sin(\omega_0\tau_0)\left[\frac{A_0^3}{4\omega_0} + A_0(\omega_0 + \tau_0\omega_2)\right]\,, \\
\alpha_{2,3}^{(2)} &= -a_2\sin(\omega_0\tau_0)\frac{A_0^3}{12}\left[2\cos(2\omega_0\tau_0) - 1\right]\,, \\
\beta_{2,3}^{(2)} &= -a_2\sin(\omega_0\tau_0)\frac{A_0^3}{12\omega_0}\left[2\cos(2\omega_0\tau_0) + 1\right]\,,
\end{aligned}
\tag{2.25}
$$

while all other coefficients vanish. Imposing the conditions (2.18), (2.19) on the inhomogeneity

18

n	ω_n
2	$-\dfrac{4}{2+\pi}$
4	$\dfrac{4(341+108\pi)}{27(2+\pi)^3}$
6	$-\dfrac{8(73843+40773\pi+5832\pi^2)}{729(2+\pi)^5}$
8	$\dfrac{1440729464+3\pi(359606308+92814567\pi+8398080\pi^2)}{98415(2+\pi)^7}$
10	$-\dfrac{2(1885638326848+9\pi(193375795408+3\pi(22966214893+4\pi(952738307+62985600\pi))))}{13286025(2+\pi)^9}$
12	$(48294520193761504+3\pi(17432699637100336+3\pi(2577825095210584$ $+\pi(596088219927028+72959354094441\pi+3809369088000\pi^2)))))/(8370195750(2+\pi)^{11})$
14	$-(137083613818976067424+3\pi(56352224911533618320+3\pi(9835626348748269040$ $+3\pi(949130678879606440+3\pi(54285350368574420$ $+\pi(5287281140608997+228562145280000\pi))))))/(1129976426250(2+\pi)^{13})$
16	$(290578164278923471719089408+9\pi(44452665928743252091582336$ $+3\pi(8868376426577693217600640+3\pi(1013305929108995195501920+$ $9\pi(24272564564656648301080+\pi(3331148075811324207916+\pi(270489187825118497343$ $+9983594505830400000\pi)))))))/(111054083171850000(2+\pi)^{15})$

Table 2.1: Expansion coefficients for the angular frequency of the limit cycle for $a_1=-1$, $a_2=2$ up to order ϵ^{16}.

$\mathbf{f}^{(2)}(\xi)$, we obtain the system of equations

$$A_0^2(1+a_1^2+\omega_0^2)-8a_1^2\omega_0(\omega_0+\omega_2\tau_0) = 0\,,$$
$$A_0^2\omega_0(1+a_1^2+\omega_0^2)+8a_1^2\omega_0+8a_1^2(1+\tau_0)\omega_2 = 0\,. \tag{2.26}$$

Its solutions read

$$\omega_2=-\frac{\omega_0+\omega_0^3}{1+\tau_0+\tau_0\omega_0^2}\qquad\text{and}\qquad A_0=\pm\sqrt{\frac{8a_1^2\omega_0^2}{(1+a_1^2+\omega_0^2)(1+\tau_0+\omega_0^2\tau_0)}}\,. \tag{2.27}$$

Choosing the sign of A_0 to be positive fixes the phase of our zeroth order solution definitively.

$a_{1,k}^{(n)}$	$k=1$	$k=3$	$b_{1,k}^{(n)}$	$k=1$	$k=3$
$n=0$	$\dfrac{4}{\sqrt{3(2+\pi)}}$	0	$n=0$	0	0
$n=2$	$-\dfrac{5\sqrt{3}(116+33\pi)}{81(2+\pi)^{5/2}}$	$-\dfrac{2\sqrt{3}}{27(2+\pi)^{3/2}}$	$n=2$	0	$\dfrac{14\sqrt{3}}{27(2+\pi)^{3/2}}$

$a_{2,k}^{(n)}$	$k=1$	$k=3$	$b_{2,k}^{(n)}$	$k=1$	$k=3$
$n=0$	0	0	$n=0$	$\dfrac{4\sqrt{2}}{\sqrt{3(2+\pi)}}$	0
$n=2$	0	$\dfrac{10\sqrt{6}}{27(2+\pi)^{3/2}}$	$n=2$	$-\dfrac{\sqrt{6}(436+93\pi)}{81(2+\pi)^{5/2}}$	$-\dfrac{2\sqrt{6}}{27(2+\pi)^{3/2}}$

Table 2.2: Fourier expansion coefficients of the limit cycle for $a_1 = -1$, $a_2 = 2$ up to the second order in ϵ.

This procedure can easily be carried to higher orders, where only even orders lead to nonzero terms for both the corrections to the angular frequency ω_n and the expansion of the limit cycle $\mathbf{V}^{(n)}(\xi)$. Expanding (2.8) to order ϵ^{2n}, we find the coefficient $A_{2(n-1)}$ and the correction ω_{2n} from the conditions (2.18), (2.19).

From here on, we consider the choice of parameters $a_1 = -1$, $a_2 = 2$. These parameter values lead to $\omega_0 = 1$, $\tau_0 = \pi/4$ and the solution (2.27) reduces to

$$\omega_2 = -\frac{4}{2+\pi} \qquad \text{and} \qquad A_0 = \frac{4}{\sqrt{3(2+\pi)}}\,. \tag{2.28}$$

Table 2.1 shows the first eight nonvanishing corrections to the angular frequency. Note that the signs of the expansion coefficients ω_n alternate and that their absolute value grows rapidly. This indicates that the perturbation series for ω is a divergent Borel series. Table 2.2 shows the expansion coefficients of the first two nonvanishing orders of the Fourier expansion of the limit cycle as given by (2.16). Figure 2.2(a) shows the first eight orders of the perturbatively calculated angular frequency $\omega^{(N)}$,

$$\omega^{(N)} = \sum_{n=0}^{N} \omega_{2n}\epsilon^{2n}\,, \tag{2.29}$$
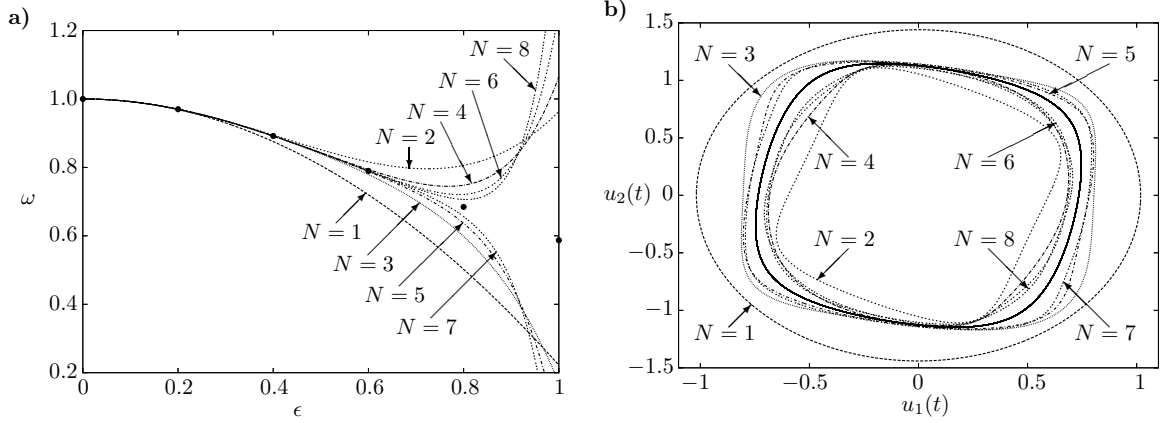
Figure 2.2: Perturbative results for the angular frequency ω and the limit cycle $\{u_1(t),\, u_2(t)\}$. In **(a)** the angular frequency is shown as a function of ϵ. The dashed lines represent the perturbative results as given by (2.29) and Tab. 2.1. Numerical results are shown by dots. In **(b)** the limit cycle $\{u_1(t),\, u_2(t)\}$ is shown for $\epsilon = 1$. Dashed lines represent perturbative results according to (2.30); the numerical result is shown by the solid line.

as a function of ϵ. Note that odd and even perturbation orders yield results which are respectively smaller and larger than the numerical values. For small values of the delay, the perturbative solution is in good agreement with the numerical data. However, as ϵ grows, the perturbative solution becomes unacceptable. Figure 2.2(b) shows an example of the perturbatively calculated limit cycle given by

$$\mathbf{u}^{(N)}(t) = \epsilon \sum_{n=0}^{N-1} \mathbf{V}^{(2n)}(\xi/\omega)\epsilon^{2n} , \tag{2.30}$$

where we count the order N of our perturbation expansion such that in the Nth order we obtain the Nth nonvanishing corrections ω_{2N} and $\mathbf{V}^{(2(N-1))}(\xi)$. For the value $\epsilon = 1$ chosen in Fig. 2.2(b), the limit cycle can still be obtained with good precision from the perturbation series (2.30) and as in the case of the angular frequency we observe that the perturbative approximations approach the numerical result in an alternating manner. However, as ϵ increases, the perturbative solution (2.30) becomes useless as in the case of the angular frequency. Thus, if we want to obtain analytical results for larger values of the temporal delay τ, we must resum our perturbation series. In the next section, we apply a Shohat transformation to the perturbative results for both the angular frequency $\omega^{(N)}$ and the limit cycle $\mathbf{u}^{(N)}(t)$.

2.5 Shohat Expansion

Now, we resum our perturbative results by performing a Shohat expansion. This method was first introduced for calculating the period of a Van der Pol oscillator in Ref. [37] and it has been conjectured that the expansion yields results which are valid for all values of the perturbation parameter [37, 38]. Furthermore, it has been stated that the Shohat expansion is successful when the periodic solution to the differential equation in question is of softening type, i.e., the angular frequency ω decreases with ϵ [39], which is the case for our system as is evident from Fig. 2.2(a).

The basic idea of the Shohat expansion is to map the perturbation parameter $\epsilon \in [0, \infty)$ to a new parameter $\mu \in [0, 1)$. In order to perform the resummation of the angular frequency, we introduce the new expansion parameter μ according to the transformation suggested by Shohat in Ref. [37] and thus set

$$\mu = \frac{\epsilon^2}{1 + \epsilon^2}\,, \tag{2.31}$$

where we explicitly take into account that the perturbation series for the angular frequency depends only on even powers of ϵ. Inverting (2.31), we have

$$\epsilon^2 = \frac{\mu}{1 - \mu}\,. \tag{2.32}$$

We now obtain the Shohat expansion of our perturbative result by replacing ϵ^2 in (2.29) according to the last identity and re-expanding the series in μ up to order μ^N. The Shohat expansion of the angular frequency is thus given by

$$\omega_{\mathrm{S}}^{(N)} = \sum_{n=0}^{N} \mu^n \sum_{k=0}^{n} \binom{n-1}{k} \omega_{2(n-k)}\,. \tag{2.33}$$

The resummation of the limit cycle (2.30) is performed in a similar manner and we obtain

$$\mathbf{u}_{\mathrm{S}}^{(N)}(t) = \epsilon \sum_{n=0}^{N-1} \mu^n \sum_{k=0}^{n} \binom{n-1}{k} \mathbf{V}^{(2(n-k))}(t)\,. \tag{2.34}$$

Finally, in order to evaluate the resummed angular frequency and limit cycle for a certain value of
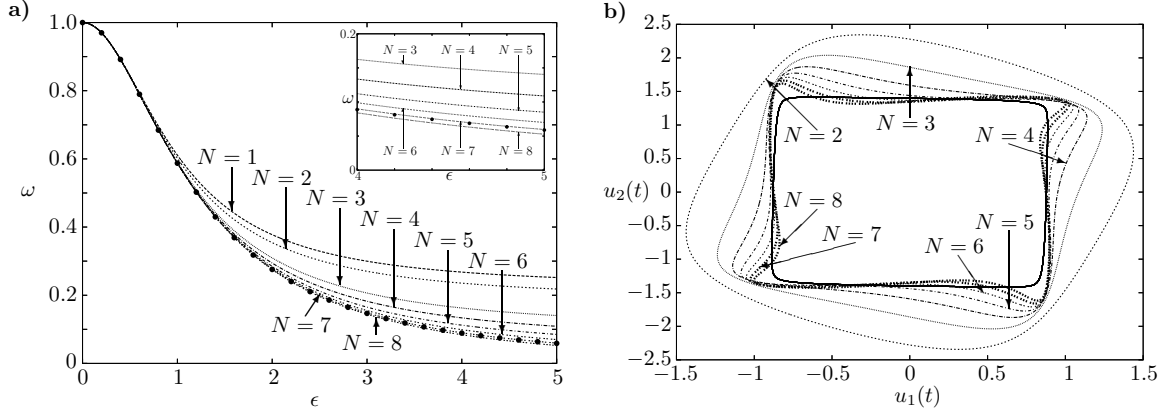
Figure 2.3: Angular frequency and limit cycle after Shohat resummation. In **(a)** the angular frequency is shown as a function of ϵ. Results from the Shohat expansion as given by (2.33) are shown by dashed lines. Numerical results are shown by dots. The inset shows a magnification of the interval $4 \leq \epsilon \leq 5$. In **(b)** the limit cycle is shown for $\epsilon = 2$. Dashed lines represent results from the Shohat expansion as given by (2.34); the numerical result is shown by the solid line.

ϵ, we replace μ in (2.33) and (2.34) according to (2.31).

Figure 2.3(a) shows the angular frequency after Shohat resummation as a function of the delay parameter ϵ. We find that, if we go to sufficiently high orders, the resummed expansion yields reasonably good results for all values of ϵ. Figure 2.3(b) shows an example of the limit cycle after resummation. Note that for the value of the delay parameter in Fig. 2.3(b) the perturbative result prior to resummation would be completely useless.

Figure 2.4(a) shows the convergence of the angular frequency obtained from the Shohat expansion versus the perturbation order N for different values of the temporal delay. For small values of the delay, the convergence seems to be exponentially fast, at least up to the eighth order. For larger delays, the convergence appears to be less regular. In order to examine the convergence of the limit cycle results, we consider the error measure

$$\delta^{(N)} = \frac{\int_{T_0}^{T_0+T} dt \, \left\| \mathbf{u}(t) - \mathbf{u}^{(N)}(t) \right\|_2}{\int_{T_0}^{T_0+T} dt \, \left\| \mathbf{u}(t) \right\|_2}, \tag{2.35}$$

where we rescale the argument of our analytic solution so that its period is identical to the period of the numerical solution and shift the phase of the analytic solution according to the phase of the numerical solution. Figure 2.4(b) shows the convergence of the results for the limit cycle. As in the case of the angular frequency, the results from the Shohat expansion and their convergence with

23
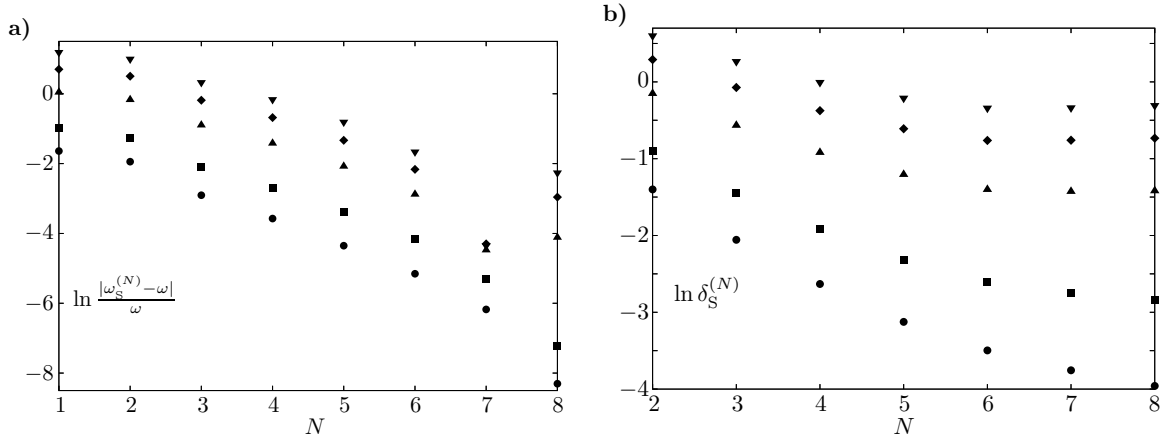
Figure 2.4: Convergence of the angular frequency and the limit cycle after Shohat resummation. In **(a)** the logarithm of the relative deviation of the angular frequency as given by (2.33) from the numerical value and in **(b)** the logarithm of the error measure for the limit cycle as given by (2.35) are shown versus the perturbation order. In both **(a)** and **(b)** different symbols indicate different values of ϵ (dots: $\epsilon = 1.6$; squares: $\epsilon = 2.0$; triangles: $\epsilon = 3.0$; diamonds: $\epsilon = 4.0$, upside-down triangles: $\epsilon = 5.0$).

the perturbation order are best as long as the delay is not too large. In the next section, we thus use a more efficient method to resum the perturbation series. It yields accurate results already in low orders, allows us to obtain more precise results, and its convergence depends less crucially on the size of the delay parameter.

2.6 Variational Perturbation Theory

In this section, we improve the resummation of the perturbation series of the angular frequency and the limit cycle by applying VPT to the perturbation series (2.29) and (2.30). This method is based on a variational approach due to Feynman and Kleinert [21], which has been systematically extended to the nonperturbative approximation scheme now called VPT [22–25].

2.6.1 Basic Principles

VPT is capable of converting divergent weak-coupling into convergent strong-coupling expansions and has been applied successfully in various fields, such as quantum mechanics, quantum statistics, condensed matter physics, and the theory of critical phenomena. In fact, the most accurate critical exponents come from this theory [40], as verified by recent satellite experiments [41]. First appli-

cations of VPT in the field of Markov processes and nonlinear dynamics are found in Refs. [47, 48] and Ref. [11], respectively.

The convergence of VPT has been analyzed up to very high orders for the ground-state energy of the anharmonic oscillator

$$V(x) = \frac{1}{2}\omega^2 x^2 + gx^4 \tag{2.36}$$

and was found to be exponentially fast [42, 43]. This surprising result has been confirmed later by studying other physical systems and was proven to hold in general [23, 24]. Furthermore, the exponential convergence seems to be uniform with respect to other system parameters. The variational resummation of perturbation series thus yields approximations which are generically reasonable for all temperatures [44, 45], space and time coordinates [46–48], magnetic field strengths [49], coupling constants [26, 50, 51], spatial dimensions [52], etc.

VPT permits the evaluation of a divergent series of the form

$$f^{(N)}(g) = \sum_{n=0}^{N} a_n g^n \tag{2.37}$$

and yields a strong-coupling expansion of the generic form

$$f(g) = g^{p/q} \sum_{m=0}^{M} b_m g^{-2m/q} . \tag{2.38}$$

Here, p and q are real growth parameters and characterize the strong-coupling behavior. Introducing a scaling parameter κ, which is afterwards set to one, Eq. (2.37) can be rewritten as

$$f^{(N)}(g) = \kappa^p \sum_{n=0}^{N} a_n \left(\frac{g}{\kappa^q}\right)^n \Bigg|_{\kappa=1} . \tag{2.39}$$

Applying Kleinert's square-root trick [23], i.e. setting

$$\kappa = K\sqrt{1+gr} , \qquad \text{with} \qquad r = \frac{\kappa^2 - K^2}{gK^2} \tag{2.40}$$

in (2.39), the variational parameter K is introduced into the perturbation series:

$$f^{(N)}(g) = \sum_{n=0}^{N} a_n g^n K^{p-nq}(1 + gr)^{(p-nq)/2}\Big|_{\kappa=1}. \tag{2.41}$$

The Taylor series of $(1 + gr)^\alpha$ with $\alpha \equiv (p - nq)/2$ reads

$$(1 + gr)^\alpha\Big|_{\kappa=1} = \sum_{k=0}^{N-n} \binom{\alpha}{k} \left(\frac{1}{K^2} - 1\right)^k + \mathcal{O}\left(g^{N-n+1}\right), \tag{2.42}$$

where the generalized binomial coefficient is defined by

$$\binom{\alpha}{k} \equiv \frac{\Gamma(\alpha + 1)}{\Gamma(k + 1)\Gamma(\alpha - k + 1)}. \tag{2.43}$$

The series (2.42) is truncated after $k = N - n$ since the original function $f^{(N)}(g)$ is only known up to order g^N. As a result of this truncation, the function $f^{(N)}(g)$ becomes dependent on the variational parameter K:

$$f^{(N)}(g, K) = \sum_{n=0}^{N} a_n g^n K^{p-nq} \sum_{k=0}^{N-n} \binom{(p - nq)/2}{k} \left(\frac{1}{K^2} - 1\right)^k. \tag{2.44}$$

The influence of the variational parameter is then optimized according to the *principle of minimal sensitivity* [53], i.e., one evaluates the function (2.44) at that value of the variational parameter K for which it has an extremum or turning point. In the following, we set $g = \epsilon^2$ in (2.29) and (2.30).

2.6.2 Resummation of the Angular Frequency

We now apply VPT to obtain an improved resummation of the angular frequency (2.29). VPT is applicable when the physical quantity in question has a strong-coupling expansion of the form (2.38) [23, 24]. Therefore, we first consider our numerical data for the angular frequency in the case of large delays and determine the growth parameter p and q in (2.38). To this end, we a analyze our numerical data in two steps. First, in Fig. 2.5(a), we plot our numerical results for $\ln \omega$ versus $\ln g = \ln(\tau - \tau_0)$. Fitting our data to a function of the form

$$f(\ln g) = p/q \ln g + \ln b_0, \tag{2.45}$$

26

a)

b)
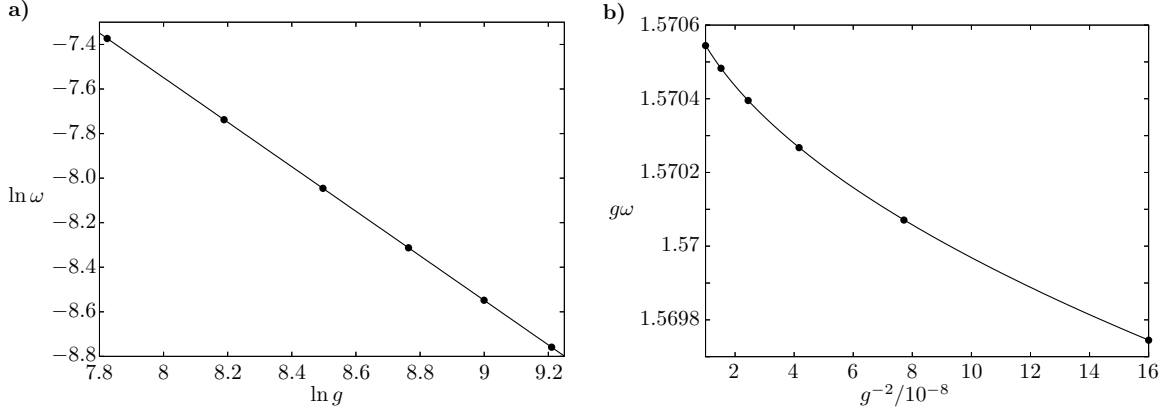
Figure 2.5: Angular frequency for large delays ($\sqrt{\tau - \tau_0} \in [50, 100]$). In **(a)** the logarithm of the angular frequency is shown versus the logarithm of the delay parameter g. Numerical data are represented by dots; the solid line represents a fit of the data to a function of the form (2.45). In **(b)** the product of the delay parameter and the angular frequency is shown versus the inverse square of the delay parameter. Numerical data are represented by dots; the solid line represents a fit of the data to a function of the form (2.46).

we find $p/q = -0.9997$ and $b_0 = 1.565$. We expect the growth parameters to be integers and thus set $p/q = -1$. For large delays, the leading asymptotic behavior of ω is thus given by $\omega \sim g^{-1}$. In order to determine not only the ratio of p to q but the individual values of the growth parameters, we then fit our data for $g\omega$ to a function of the form

$$f(g^{-2}) = b_0 + b_1 g^{-2/q}, \tag{2.46}$$

which is shown in Fig. 2.5(b). The numerical results from the fit are: $b_0 = 1.571$, $b_1 = -2.7$, and $q = 1.993$. Thus, we assume $q = 2$ and from our previous result we then have $p = -2$. In order to determine b_0 and b_1 numerically with better accuracy, we can now perform a hierarchy of approximations to order M by fitting $g\omega$ to functions of the form

$$f(g^{-1}) = \sum_{m=0}^{M} b_m g^{-m}. \tag{2.47}$$

From this procedure we obtain the more precise numerical values $b_0 = 1.57081$ and $b_1 = -2.66$. Now, we can introduce the variational parameter K to the perturbation series (2.29) according to

(2.44) with $p = -2$, $q = 2$:

$$\omega_{\text{VPT}}^{(N)}(g, K) = \sum_{n=0}^{N} \omega_{2n} g^n K^{p-nq} \sum_{k=0}^{N-n} \binom{(p-nq)/2}{k} \left(\frac{1}{K^2} - 1\right)^k . \tag{2.48}$$

To first order we obtain

$$\omega_{\text{VPT}}^{(1)}(g, K) = \frac{(2+\pi)(2K^2 - 1) - 4g}{K^4(2+\pi)} , \tag{2.49}$$

which has a minimum at

$$K^{(1)} = \sqrt{1 + \frac{4g}{2+\pi}} . \tag{2.50}$$

Evaluating (2.49) at the optimized value of the variational parameter then yields

$$\omega_{\text{VPT}}^{(1)}(g, K^{(1)}) = \frac{2+\pi}{4g + 2 + \pi} . \tag{2.51}$$

In the limit of large delays, $g \to \infty$, we thus have

$$\omega_{\text{VPT}}^{(1)}(g, K^{(1)}) \sim b_0^{(1)} g^{-1} + b_1^{(1)} g^{-2} , \tag{2.52}$$

with

$$b_0^{(1)} = \frac{2+\pi}{4} \approx 1.28540 \qquad \text{and} \qquad b_1^{(1)} = -\frac{(2+\pi)^2}{16} \approx -1.6522 . \tag{2.53}$$

To second order, Eq. (2.48) yields

$$\omega_{\text{VPT}}^{(2)}(g, K) = \frac{1}{27K^6} \left[27\left(3K^4 - 3K^2 + 1\right) + g \frac{108\left(2 - 3K^2\right)}{2+\pi} + g^2 \frac{4(341 + 108\pi)}{(2+\pi)^3} \right] . \tag{2.54}$$

Since this has no real extremum in the variational parameter K, we look for roots of the second derivative.

In general, in order to optimize the influence of the variational parameter, we first look for minima or maxima of $\omega_{\text{VPT}}^{(N)}(g, K)$, and if those do not exist, for positive roots of higher derivatives.

In each order N, the optimized variational parameter $K^{(N)}$ is thus determined from the condition

$$\left.\frac{d\omega_{\text{VPT}}^{(N)}(g,K)}{dK}\right|_{K=K^{(N)}} = 0 \qquad \text{or} \qquad \left.\frac{d^2\omega_{\text{VPT}}^{(N)}(g,K)}{d^2K}\right|_{K=K^{(N)}} = 0, \cdots. \tag{2.55}$$

In cases where a certain derivative has several positive roots, we choose the one which is closest to the optimized value from the previous order $K^{(N-1)}$. The Nth order VPT approximation of the angular frequency is then obtained by evaluating (2.48) for the value of the optimized variational parameter:

$$\omega_{\text{VPT}}^{(N)}(g) = \omega_{\text{VPT}}^{(N)}(g, K^{(N)}). \tag{2.56}$$

Returning to (2.54), we find that for

$$g \leq \frac{3(2+\pi)[24 + 12\pi + 5\sqrt{35(2+\pi)}]}{587 - 144\pi} \approx 14.756 \tag{2.57}$$

$\omega_{\text{VPT}}^{(2)}(g,K)$ has two positive turning points:

$$\tilde{K}_{\pm}^{(2)} = \frac{\sqrt{60 + 15\pi(4+\pi) + 60(2+\pi)g \pm 2\eta}}{3(2+\pi)}, \tag{2.58}$$

with the abbreviation

$$\eta = \sqrt{(2+\pi)[9(2+\pi)^3 + 72(2+\pi)^2 g - (587 - 144\pi)g^2]}. \tag{2.59}$$

Comparing (2.58) to (2.50), we find that $\tilde{K}_-^{(2)}$ is closer to $K^{(1)}$ and thus evaluate (2.54) for $K = \tilde{K}_-^{(2)}$ to obtain

$$\begin{aligned}
\omega_{\text{VPT}}^{(2)}(g, \tilde{K}_-^{(2)}) &= \frac{27(2+\pi)^2}{[15(2+\pi)(2+\pi+4g) - 2\eta]^3}\Big\{4\eta^2 - 42(2+\pi)(2+\pi+4g)\eta \\
&\quad + (2+\pi)[117(2+\pi)^3 + 936(2+\pi)^2 g + 4(1061 + 468\pi)g^2]\Big\}. \tag{2.60}
\end{aligned}$$

However, for delay parameters exceeding the value of g given in (2.57), we cannot use $\tilde{K}_{\pm}^{(2)}$ since in this case η becomes imaginary. Thus, if we want to consider the limit of large delays, we must optimize the variational parameter by considering the third derivative of $\omega_{\text{VPT}}^{(2)}(g,K)$, which turns

out to have two positive roots for all positive g:

$$K_{\pm}^{(2)} = \frac{\sqrt{180 + 45\pi(4 + \pi) + 180(2 + \pi)g \pm \rho}}{3\sqrt{2}(2 + \pi)}, \tag{2.61}$$

with the abbreviation

$$\rho\sqrt{(2 + \pi)[513(2 + \pi)^3 + 4104(2 + \pi)^2 g + 16(513\pi - 724)g^2]}. \tag{2.62}$$

Again, $K_{-}^{(2)}$ is closer to the first-order solution, and we set $K^{(2)} = K_{-}^{(2)}$, to obtain

$$\begin{aligned}
\omega_{\text{VPT}}^{(2)}(g, K^{(2)}) &= \frac{54(2 + \pi)^2}{[45(2 + \pi)(2 + \pi + 4g) - \rho]^3}\Big\{\rho^2 - 72(2 + \pi)(2 + \pi + 4g)\rho \\
&\quad + (2 + \pi)[1323(2 + \pi)^3 + 10584(2 + \pi)^2 g + 16(2771 + 1323\pi)g^2]\Big\}.
\end{aligned} \tag{2.63}$$

Expanding the last result in g^{-1}, we obtain

$$\omega_{\text{VPT}}^{(2)}(g, K^{(2)}) \sim b_0^{(2)}g^{-1} + b_1^{(2)}g^{-2}, \tag{2.64}$$

with

$$b_0^{(2)} = \frac{27(2 + \pi)^3\left[2047 + 1836\pi - 72\sqrt{(2 + \pi)(513\pi - 724)}\right]}{2\left[90 + 45\pi - \sqrt{(2 + \pi)(513\pi - 724)}\right]^3} \approx 1.23174 \tag{2.65}$$

and

$$\begin{aligned}
b_1^{(2)} &= \frac{243(2 + \pi)^5}{8\left[90 + 45\pi - \sqrt{(2 + \pi)(513\pi - 724)}\right]^4}\Bigg\{63213\sqrt{\frac{2 + \pi}{513\pi - 724}} + 162\pi \\
&\quad \times \left[437\sqrt{\frac{2 + \pi}{513\pi - 724}} - 82\right] + 426\sqrt{(2 + \pi)(513\pi - 724)} - 16193\Bigg\} \approx -1.1229.
\end{aligned} \tag{2.66}$$

It thus turns out that the second order approximation for the leading and subleading large-delay coefficient is actually worse than the first order one. However, the results in higher orders turn out to be improved approximations. For fixed values of the coupling constant, the procedure in higher orders is analogous to the first and second order, where the roots of the first, second, or third
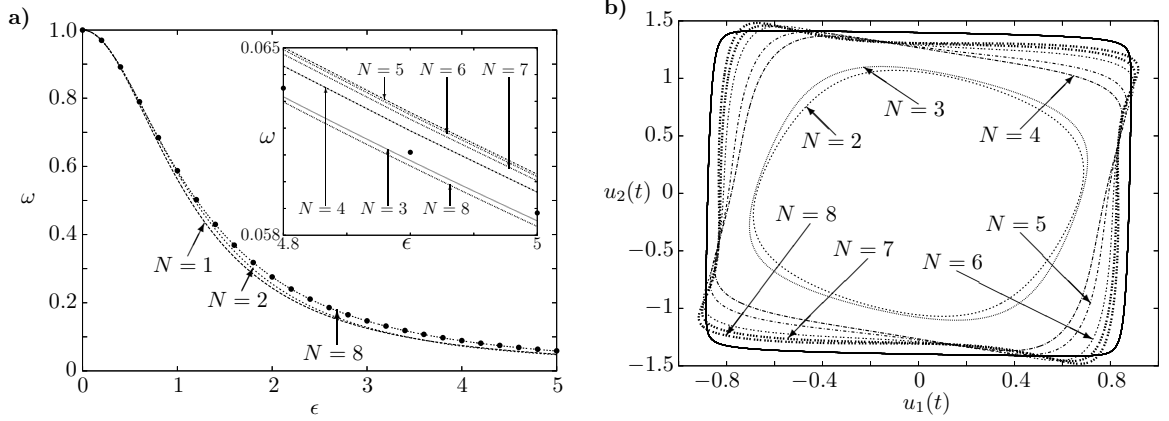
Figure 2.6: Angular frequency and limit cycle from VPT. In **(a)** the angular frequency as given by (2.56) is shown as a function of ϵ for the orders $N = 1, 2, 8$ of VPT (orders three through seven would lie very close to the curve for $N = 8$). Dots represent numerical values. The inset shows a magnification of the interval $4.8 \le \epsilon \le 5$. In **(b)** the limit cycle is shown for $\epsilon = 2$. Dashed lines represent the results from VPT as given by (2.70). The numerical result is shown by the solid line.

derivative of $\omega_{\text{VPT}}^{(N)}(g, K)$ have to be determined numerically. Furthermore, in order to obtain the coefficients $b_0^{(N)}$ and $b_1^{(N)}$, we expand the derivatives of $\omega_{\text{VPT}}^{(N)}(g, K)$ in g^{-1} and the variational parameter K as

$$K^{(N)} = K_0^{(N)} g^{1/2} + K_1^{(N)} g^{-1/2} + \cdots \tag{2.67}$$

in order to carry out the optimization procedure.

Fig. 2.6(a) shows our VPT results for the angular frequency versus the delay parameter ϵ. The first order result is already in good agreement with the numerical results for a wide range of delays and is far superior to the first order result from the Shohat expansion (compare Fig. 2.3(a)). Figure 2.7(a) shows the convergence of our VPT results for five different values of the delay. The accuracy of our VPT results improves with increasing order; however, not as regularly as in the case of the Shohat expansion for small delays. Figure 2.8(a) shows a comparison of the eighth order results obtained from Shohat resummation and VPT. In particular, for larger values of the delay, the results from VPT are far superior to the ones from Shohat resummation. Table 2.3 shows our results for the leading large-delay coefficients b_0 and the subleading coefficient b_1; again, the convergence is not monotonic, but we do observe a general trend towards improved results in higher orders.
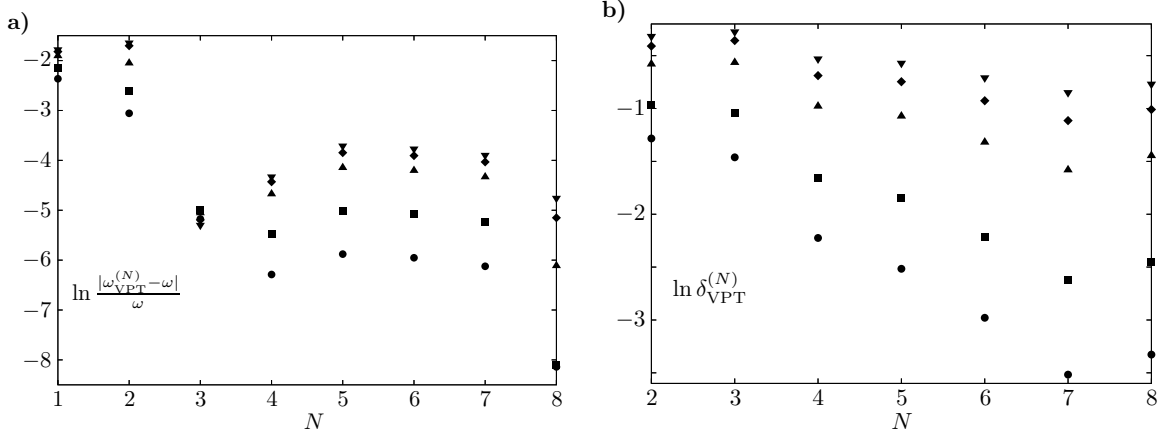
Figure 2.7: Convergence of the angular frequency and the limit cycle after resummation with VPT. In **(a)** the logarithm of the relative deviation of the angular frequency as given by (2.56) from the numerical values and in **(b)** the logarithm of the error measure for the limit cycle as given by (2.35) are shown versus the perturbation order. In both **(a)** and **(b)** different symbols indicate different values of ϵ (dots: $\epsilon = 1.6$; squares: $\epsilon = 2.0$; triangles: $\epsilon = 3.0$; diamonds: $\epsilon = 4.0$, upside-down triangles: $\epsilon = 5.0$).

2.6.3   Resummation of the Limit Cycle

We now proceed to perform a variational resummation of the limit cycle following the approach of Ref. [54]. To this end, we consider the perturbation series of each coefficient in the Fourier expansion of $\mathbf{V}(\xi)$ as given by (2.16)

$$
\begin{aligned}
A_{1/2,k}^{(N)} &= \sum_{n=0}^{N-1} a_{1/2,k}^{(2n)} g^n , \\
B_{1/2,k}^{(N)} &= \sum_{n=0}^{N-1} b_{1/2,k}^{(2n)} g^n .
\end{aligned}
\tag{2.68}
$$

We introduce the variational parameter K into the perturbation series for $A_{1/2,k}^{(N)}$ and $B_{1/2,k}^{(N)}$ in the same way as for the angular frequency, and obtain by applying (2.44) to the Fourier expansions (2.68)

$$
\begin{aligned}
A_{1/2,k,\mathrm{VPT}}^{(N)}(g,K) &= \sum_{n=0}^{N-1} a_{1/2,k}^{(2n)} g^n K^{p-nq} \sum_{k=0}^{N-n} \binom{(p-nq)/2}{k} \left(\frac{1}{K^2} - 1 \right)^k , \\
B_{1/2,k,\mathrm{VPT}}^{(N)}(g,K) &= \sum_{n=0}^{N-1} b_{1/2,k}^{(2n)} g^n K^{p-nq} \sum_{k=0}^{N-n} \binom{(p-nq)/2}{k} \left(\frac{1}{K^2} - 1 \right)^k .
\end{aligned}
\tag{2.69}
$$
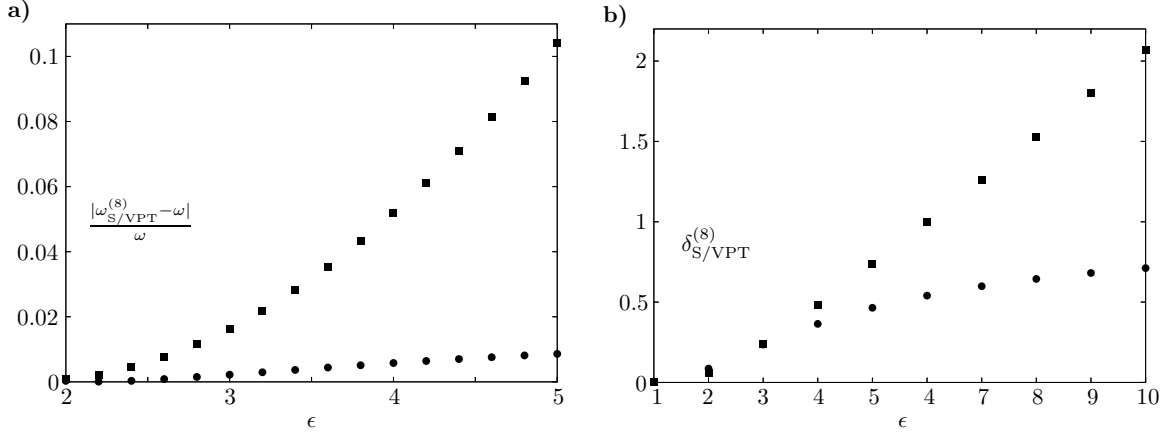
Figure 2.8: Comparison of the eighth order results for **(a)** the angular frequency and **(b)** the limit cycle obtained from the Shohat expansion and VPT. The relative deviations of the analytical results from the corresponding numerical values are shown versus the delay parameter (Shohat expansion: squares; VPT: circles).

Instead of optimizing (2.69) according to the principle of minimal sensitivity, we obtain our VPT result for the limit cycle more easily by evaluating all Fourier expansion coefficients for that value of the variational parameter K which was determined through the optimization procedure of the frequency, i.e., our VPT result for the limit cycle reads:

$$
\begin{pmatrix} V_{1,\mathrm{VPT}}^{(N)}(\xi) \\ V_{2,\mathrm{VPT}}^{(N)}(\xi) \end{pmatrix} = \sum_{k=1}^{\infty} \left[\begin{pmatrix} A_{1,k,\mathrm{VPT}}^{(N)}(g, K^{(N-1)}) \\ A_{2,k,\mathrm{VPT}}^{(N)}(g, K^{(N-1)}) \end{pmatrix} \cos k\xi + \begin{pmatrix} B_{1,k,\mathrm{VPT}}^{(N)}(g, K^{(N-1)}) \\ B_{2,k,\mathrm{VPT}}^{(N)}(g, K^{(N-1)}) \end{pmatrix} \sin k\xi \right],
$$
(2.70)

where $K^{(N-1)}$ is determined from the condition (2.55) and we use $K^{(N-1)}$ instead of $K^{(N)}$, since the Nth term in the series for $\mathbf{V}(\xi)$ is a correction of order g^{N-1}.

As an example, we consider the lowest order in which we can perform the VPT resummation of the limit cycle. To order g our solution for $\mathbf{V}(\xi)$ reads

$$
V_1(\xi) = \frac{4\cos\xi}{\sqrt{3(2+\pi)}} - g\left\{ \frac{5\sqrt{3}(116+33\pi)\cos\xi}{81(2+\pi)^{5/2}} + \frac{2\sqrt{3}}{27(2+\pi)^{3/2}}[\cos 3\xi - 7\sin 3\xi] \right\} + \mathcal{O}(g^2),
$$
$$
V_2(\xi) = \frac{4\sqrt{2}\sin\xi}{\sqrt{3(2+\pi)}} - g\left\{ \frac{\sqrt{6}(436+93\pi)\sin\xi}{81(2+\pi)^{5/2}} - \frac{2\sqrt{6}}{27(2+\pi)^{3/2}}[5\cos 3\xi - \sin 3\xi] \right\} + \mathcal{O}(g^2).
$$
(2.71)

N	1	2	3	4	5	6	7	8	Numerical
$b_0^{(N)}$	1.2854	1.23174	1.56495	1.59507	1.61990	1.61806	1.61139	1.54478	1.57081
$b_1^{(N)}$	-1.65	-1.12	-2.72	-2.79	-3.05	-3.03	-2.98	-2.21	-2.66

Table 2.3: Leading and subleading coefficients for the large-delay behavior of the angular frequency.

Introducing the variational parameter K according to (2.69), we obtain

$$
\begin{aligned}
V_{1,\text{VPT}}^{(2)}(\xi, K) &= \frac{4(2K^2 - 1)\cos\xi}{K^4\sqrt{3(2+\pi)}} \\
&\quad - \frac{g}{K^4}\left\{\frac{5\sqrt{3}(116 + 33\pi)}{81(2+\pi)^{5/2}}\cos\xi + \frac{2\sqrt{3}}{27(2+\pi)^{3/2}}[\cos 3\xi - 7\sin 3\xi]\right\}, \\
V_{2,\text{VPT}}^{(2)}(\xi, K) &= \frac{4(2K^2 - 1)\sqrt{2}\sin\xi}{K^4\sqrt{3(2+\pi)}} \\
&\quad - \frac{g}{K^4}\left\{\frac{\sqrt{6}(436 + 93\pi)}{81(2+\pi)^{5/2}}\sin\xi - \frac{2\sqrt{6}}{27(2+\pi)^{3/2}}[5\cos 3\xi - \sin 3\xi]\right\}. \quad (2.72)
\end{aligned}
$$

The optimal value of the variational parameter for the angular frequency to first order is given by (2.50). Inserting this value into (2.72), we find the following VPT result for the limit cycle:

$$
\begin{aligned}
V_{1,\text{VPT}}^{(2)}(\xi) &= \frac{1}{27\sqrt{3(2+\pi)}(2+\pi+4g)^2}\left\{108(2+\pi)^2\cos\xi \right. \\
&\quad \left. + g\left[(1148 + 699\pi)\cos\xi - 6(2+\pi)(\cos 3\xi - 7\sin 3\xi)\right]\right\}, \\
V_{2,\text{VPT}}^{(2)}(\xi) &= \frac{2}{27\sqrt{6(2+\pi)}(2+\pi+4g)^2}\left\{108(2+\pi)^2\sin\xi \right. \\
&\quad \left. + g\left[(1292 + 771\pi)\sin\xi + 6(2+\pi)(5\cos 3\xi - \sin 3\xi)\right]\right\}. \quad (2.73)
\end{aligned}
$$

The procedure in higher order is analogous. Figure 2.6(b) shows our VPT results for the limit cycle for $\epsilon = 2$ up to the eighth order. Figure 2.7(b) shows the logarithm of the error measure (2.35) for the VPT limit cycle versus the order N for different values of ϵ. In Fig. 2.8(b) the accuracy of the eighth order results from the Shohat expansion and VPT are compared. Again, we find that our VPT results are more reliable than those from the Shohat expansion, especially for larger delays.

2.7 Summary

We have performed a perturbative calculation of the limit cycle and its frequency in a two-neuron model with delay. A Shohat resummation of the respective perturbation expansions yields results which are in good agreement with numerical values but whose accuracy decreases drastically with larger values of the delay parameter. Resumming the perturbation series with VPT yields more uniformly converging results, which are reliable even in low orders, and furthermore permits the extraction of the leading large-delay behavior with sufficient accuracy. The present work constitutes the first application of VPT to a system of DDE's. Moreover, it establishes a method for the variational resummation of perturbatively calculated limit cycles in nonlinear dynamical systems.

2.8 Acknowledgments

Appendix: Elimination of Secular Terms

We now demonstrate how the conditions (2.18), (2.19) are obtained by considering the Fourier decompositions of the periodic solution and the inhomogeneity. Inserting (2.16) and (2.17) into the system of equations (2.15) and comparing coefficients of $\sin k\xi$ and $\cos k\xi$ in both components, we obtain the following system of four equations:

$$\frac{a_{1,k}^{(n)}}{\omega_0} + kb_{1,k}^{(n)} - \frac{a_1 a_{2,k}^{(n)}}{\omega_0}\cos(k\omega_0\tau_0) + \frac{a_1 b_{2,k}^{(n)}}{\omega_0}\sin(k\omega_0\tau_0) - \alpha_{1,k}^{(n)} = 0\,, \qquad (2.74)$$

$$\frac{b_{1,k}^{(n)}}{\omega_0} - ka_{1,k}^{(n)} - \frac{a_1 b_{2,k}^{(n)}}{\omega_0}\cos(k\omega_0\tau_0) - \frac{a_1 a_{2,k}^{(n)}}{\omega_0}\sin(k\omega_0\tau_0) - \beta_{1,k}^{(n)} = 0\,, \qquad (2.75)$$

$$\frac{a_{2,k}^{(n)}}{\omega_0} + kb_{2,k}^{(n)} - \frac{a_2 a_{1,k}^{(n)}}{\omega_0}\cos(k\omega_0\tau_0) + \frac{a_2 b_{1,k}^{(n)}}{\omega_0}\sin(k\omega_0\tau_0) - \alpha_{2,k}^{(n)} = 0\,, \qquad (2.76)$$

$$\frac{b_{2,k}^{(n)}}{\omega_0} - k a_{2,k}^{(n)} - \frac{a_2 b_{1,k}^{(n)}}{\omega_0} \cos(k\omega_0\tau_0) - \frac{a_2 a_{1,k}^{(n)}}{\omega_0} \sin(k\omega_0\tau_0) - \beta_{2,k}^{(n)} = 0. \qquad (2.77)$$

It turns out that for $k > 1$ the coefficients $\mathbf{a}_k^{(n)}$, $\mathbf{b}_k^{(n)}$ can be uniquely determined for any inhomogeneity, i.e., for arbitrary $\boldsymbol{\alpha}_k^{(n)}$, $\boldsymbol{\beta}_k^{(n)}$. For $k > 1$ the solution of the system $(2.74) - (2.77)$ is

$$a_{1,k}^{(n)} = \frac{1}{D}\Big\{(\alpha_{1,k}^{(n)} - k\omega_0\beta_{1,k}^{(n)})(\omega_0 + k^2\omega_0^3) - a_1\omega_0^2 \sin(k\omega_0\tau_0)(2k\alpha_{2,k}^{(n)} - (1 + k^2)\omega_0\beta_{2,k}^{(n)})$$
$$+ a_1\omega_0 \cos(k\omega_0\tau_0)(2\alpha_{2,k}^{(n)} - 2k\omega_0\beta_{2,k}^{(n)} + (1 - k^2)\omega_0^2\alpha_{2,k}^{(n)})$$
$$+ (\omega_0 + \omega_0^3)\Big[\sin(2k\omega_0\tau_0)(\beta_{1,k}^{(n)} - k\omega_0\alpha_{1,k}^{(n)}) + \cos(2k\omega_0\tau_0)(\alpha_{1,k}^{(n)} + k\omega_0\beta_{1,k}^{(n)})\Big]\Big\},$$

$$b_{1,k}^{(n)} = \frac{1}{D}\Big\{(\beta_{1,k}^{(n)} + k\omega_0\alpha_{1,k}^{(n)})(\omega_0 + k^2\omega_0^3) - a_1\omega_0^2 \sin(k\omega_0\tau_0)(2k\beta_{2,k}^{(n)} + (1 + k^2)\omega_0\alpha_{2,k}^{(n)})$$
$$+ a_1\omega_0 \cos(k\omega_0\tau_0)(2\beta_{2,k}^{(n)} + 2k\omega_0\alpha_{2,k}^{(n)} + (1 - k^2)\omega_0^2\beta_{2,k}^{(n)})$$
$$+ (\omega_0 + \omega_0^3)\Big[\cos(2k\omega_0\tau_0)(\beta_{1,k}^{(n)} - k\omega_0\alpha_{1,k}^{(n)}) - \sin(2k\omega_0\tau_0)(\alpha_{1,k}^{(n)} + k\omega_0\beta_{1,k}^{(n)})\Big]\Big\},$$

$$a_{2,k}^{(n)} = \frac{1}{D}\Big\{(\alpha_{2,k}^{(n)} - k\omega_0\beta_{2,k}^{(n)})(\omega_0 + k^2\omega_0^3) + (\omega_0 + \omega_0^3)\Big[\frac{\omega_0}{a_1} \sin(k\omega_0\tau_0)(2k\alpha_{1,k}^{(n)} - \omega_0(1 + k^2)\beta_{1,k}^{(n)})$$
$$- \cos(k\omega_0\tau_0)(2\alpha_{1,k}^{(n)} - 2k\omega_0\beta_{1,k}^{(n)} + (1 - k^2)\omega_0^2\alpha_{1,k}^{(n)})$$
$$+ \sin(2k\omega_0\tau_0)(\beta_{2,k}^{(n)} - k\omega_0\alpha_{2,k}^{(n)}) + \cos(2k\omega_0\tau_0)(\alpha_{2,k}^{(n)} + k\omega_0\beta_{2,k}^{(n)})\Big]\Big\},$$

$$b_{2,k}^{(n)} = \frac{1}{D}\Big\{(\beta_{2,k}^{(n)} + k\omega_0\alpha_{2,k}^{(n)})(\omega_0 + k^2\omega_0^3) + (\omega_0 + \omega_0^3)\Big[\frac{\omega_0}{a_1} \sin(k\omega_0\tau_0)(2k\beta_{1,k}^{(n)} + \omega_0(1 + k^2)\alpha_{1,k}^{(n)})$$
$$- \cos(k\omega_0\tau_0)(2\beta_{1,k}^{(n)} + 2k\omega_0\alpha_{1,k}^{(n)} + (1 - k^2)\omega_0^2\beta_{1,k}^{(n)})$$
$$- \sin(2k\omega_0\tau_0)(\alpha_{2,k}^{(n)} + k\omega_0\beta_{2,k}^{(n)}) + \cos(2k\omega_0\tau_0)(\beta_{2,k}^{(n)} - k\omega_0\alpha_{2,k}^{(n)})\Big]\Big\}, \qquad (2.78)$$

where

$$D = 2 + 2\omega_0^2(1 + k^2) + \omega_0^4(1 + k^4)$$
$$+ (\omega_0 + \omega_0^3)\big[2(1 - k^2\omega_0^2)\cos(2\omega_0\tau_0)/\omega_0 - 4k\sin(2k\tau_0\omega_0)\big]. \qquad (2.79)$$

Note that D vanishes for $k = 1$. We must thus reconsider the system $(2.74) - (2.77)$ for the case $k = 1$ and it turns out that $\boldsymbol{\alpha}_1^{(n)}$, $\boldsymbol{\beta}_1^{(n)}$ must satisfy certain conditions for a solution to exist. For $k = 1$, we add $a_2 \sin(\omega_0\tau_0) \times (2.74)$ to (2.77) and subtract $\omega_0 \times (2.76)$ from $a_2 \cos(\omega_0\tau_0) \times (2.75)$. Using the identities $a_1 a_2 = -(\omega_0^2 + 1)$ and $\omega_0 = \cot(\omega_0\tau_0)$, we obtain the two conditions (2.18), (2.19) that must be satisfied by the inhomogeneity $\mathbf{f}^{(n)}(\xi)$. Imposing (2.18), (2.19) on $\mathbf{f}^{(n)}(\xi)$, we

obtain the following solution to the system of equations (2.74) – (2.77) for $k = 1$:

$$b_{1,1}^{(n)} = \cos(\omega_0\tau_0)\left[a_2\cos(\omega_0\tau_0)\alpha_{1,1}^{(n)} + \frac{\alpha_{2,1}^{(n)}}{a_2}\right]\frac{a_{2,1}^{(n)}}{a_2\sin(\omega_0\tau_0)}, \quad (2.80)$$

$$b_{2,1}^{(n)} = a_2\sin(\omega_0\tau_0)\left[a_{1,1}^{(n)} - \alpha_{1,1}^{(n)}\sin(\omega_0\tau_0)\cos(\omega_0\tau_0)\right] + \alpha_{2,1}^{(n)}\cos^2(\omega_0\tau_0). \quad (2.81)$$

Here, the coefficients $a_{1,1}^{(n)}$, $a_{2,1}^{(n)}$ are undetermined and follow from the initial conditions. We set $a_{1,1}^{(n)} = A_n$ and $a_{2,1}^{(n)} = 0$.

References

[1] J. Bechhoefer, Rev. Mod. Phys. **77**, 783 (2005).

[2] G. A. Bocharov and F. A. Rihan, J. Comput. Appl. Math. **125**, 183 (2000).

[3] J. Wu, *Introduction to Neural Dynamics and Signal Transmission Delay* (Walter de Gruyter, Berlin, 2001).

[4] J. J. Hopfield, Proc. Natl. Acad. Sci. U.S.A. **81**, 3088 (1984).

[5] C. M. Marcus and R. M. Westervelt, Phys. Rev. A **39**, 347 (1989).

[6] C. W. Eurich, M. C. Mackey, and H. Schwegler, J. Theor. Bio. **216**, 31 (2002).

[7] U. an der Heiden, J. Math. Bio. **8**, 345 (1979).

[8] B. D. Coleman and G. H. Renninger, SIAM J. Appl. Math. **31**, 111 (1976); J. Theor. Bio. **51**, 243 (1975).

[9] K. P. Hadeler and J. Tomiuk, Arch. Rat. Mech. Anal. **65**, 87 (1977).

[10] W. Wischert, A. Wunderlin, A. Pelster, M. Olivier, and J. Groslambert, Phys. Rev. E **49**, 203 (1994).

[11] M. Schanz and A. Pelster, Phys. Rev. E **67**, 056205 (2003).

[12] E. Ott, C. Grebogi, and J. A. Yorke, Phys. Rev. Lett. **64**, 1196 (1990).

[13] K. Pyragas, Phys. Lett. A **170**, 421 (1992).

[14] K. Pyragas, Phys. Rev. Lett. **86**, 2265 (2001).

[15] K. Pyragas and A. Tamašiavičius, Phys. Lett. A **180**, 99 (1993).

[16] D. J. Christini, V. In, M. L. Spano, W. L. Ditto, and J. J. Collins, Phys. Rev. E **56**, R3749 (1997).

[17] S. Bielawski, D. Derozier, and P. Glorieux, Phys. Rev. E **49**, R971 (1994).

[18] P. Parmananda, R. Madrigal, M. Rivera, L. Nyikos, Z. Kiss, and V. Gaspar, Phys. Rev. E **59**, 5266 (1999).

[19] O. V. Popovych, C. Hauptmann, and P. A. Tass, Phys. Rev. Lett. **94**, 164102 (2005).

[20] J. Milton, *Dynamics of Small Neural Populations* (Amer. Math. Soc., Providence, 1996).

[21] R. P. Feynman and H. Kleinert, Phys. Rev. A **34**, 5080 (1986).

[22] H. Kleinert, Phys. Lett. A **173**, 332 (1993).

[23] H. Kleinert, *Path Integrals in Quantum Mechanics, Statistics, Polymer Physics, and Financial Markets*, Third Edition (World Scientific, Singapore, 2004); Phys. Rev. D **57**, 2264 (1998).

[24] H. Kleinert and V. Schulte-Frohlinde, *Critical Properties of Φ^4-Theories* (World Scientific, Singapore, 2001); Chap. 19.

[25] W. Janke, A. Pelster, H.-J. Schmidt, and M. Bachmann (Eds.), *Fluctuating Paths and Fields – Dedicated to Hagen Kleinert on the Occasion of his 60th Birthday* (World Scientific, Singapore, 2001).

[26] A. Pelster, H. Kleinert, and M. Schanz, Phys. Rev. E **67**, 016604 (2003).

[27] K. L. Babcock and R. M. Westervelt, Physica D **28**, 305 (1987).

[28] J. Wei and S. Ruan, Physica D **130**, 255 (1999).

[29] S. Ruan and R. S. Filfil, Physica D **191**, 323 (2004).

[30] L. P. Shayer and S. A. Campbell, SIAM J. Appl. Math. **61**, 673 (2000).

[31] K. Gopalsamy and I. Leung, Physica D **89**, 395 (1996).

[32] X. Liao, S. Li, and G. Chen, Neural Networks **17**, 545 (2004).

[33] L. Olien and J. Bélair, Physica D **102**, 349 (1997).

[34] N. C. Majee and A. B. Roy, Appl. Math. Modelling **21**, 673 (1997).

[35] X. Liao, S. Li, and K.-W. Wong, Nonlinear Dynam. **31**, 299 (2003).

[36] N. MacDonald, *Time Lags in Biological Models*, Lecture Notes in Biomathematics Vol. 27 (Springer-Verlag, Berlin, 1978).

[37] J. Shohat, J. App. Phys. **14**, 568 (1943).

[38] R. Bellman, *Perturbation Techniques in Mathematics, Physics, and Engineering* (Holt, Rinehart and Winston, New York, 1964).

[39] M. S. Sarma and B. Nageswara Rao, J. Sound Vib. **209**, 879 (1998).

[40] H. Kleinert, Phys. Rev. D 60, 085001 (1999)

[41] J. A. Lipa, J. A. Nissen, D. A. Stricker, D. R. Swanson, and T. C. P. Chui, Phys. Rev. B **68**, 174518 (2003).

[42] W. Janke and H. Kleinert, Phys. Rev. Lett. **75**, 2787 (1995).

[43] H. Kleinert and W. Janke, Phys. Lett. A **206**, 283 (1995).

[44] H. Kleinert and H. Meyer, Phys. Lett. A **184**, 319 (1994).

[45] F. Weißbach, A. Pelster, and B. Hamprecht, Phys. Rev. E **66**, 036129 (2002).

[46] H. Kleinert, M. Bachmann, and A. Pelster, Phys. Rev. A **60**, 3429 (1999).

[47] H. Kleinert, A. Pelster, and M. Putz: Phys. Rev. E **65**, 066128 (2002).

[48] J. Dreger, A. Pelster, and B. Hamprecht, Eur. Phys. J. B **45**, 355 (2005).

[49] M. Bachmann, H. Kleinert, and A. Pelster, Phys. Rev. A **62**, 52509 (2000); Phys. Lett. A **279**, 23 (2001).

[50] C.M. Bender, A. Pelster, and F. Weißbach, J. Math. Phys. **43**, 4202 (2002).

[51] S. F. Brandt, H. Kleinert, and A. Pelster, J. Math. Phys. **46**, 032101 (2005).

[52] S. F. Brandt and A. Pelster, J. Math. Phys. **46**, 112105 (2005).

[53] P. M. Stevenson, Phys. Rev. D **23**, 2916 (1981).

[54] A. Pelster, A. Novikov, M. Schreiber, and U. Kleinekathöfer (unpublished result).

[55] The AnT 4.669 software package is available online at `http://www.ant4669.de`

Chapter 3

Synchronization in a neuronal feedback loop through asymmetric temporal delays

We consider the effect of asymmetric temporal delays in a system of two coupled Hopfield neurons. For couplings of opposite signs, a limit cycle emerges via a supercritical Hopf bifurcation when the sum of the delays reaches a critical value. We show that the angular frequency of the limit cycle is independent of an asymmetry in the delays. However, the delay asymmetry determines the phase difference between the periodic activities of the two components. Specifically, when the connection with negative coupling has a delay much larger than the delay for the positive coupling, the system approaches in-phase synchrony between the two components. Employing variational perturbation theory (VPT), we achieve an approximate analytical evaluation of the phase shift, in good agreement with numerical results.

Synchronization phenomena among coupled systems are abundant in nature [1, 2]. The coupling is often not instantaneous; rather finite time delays exist. In general, time delays can cause an otherwise stable system to oscillate [3–5] and may lead to bifurcation scenarios resulting in chaotic dynamics [6, 7]. For example, delay-induced oscillations have been reported for neural networks [8], genetic regulatory networks [9], and models of population dynamics [10] to name just a few.

The delays for the different coupling mechanisms in such networks do not need to be uniform, which may have an important effect on the system dynamics. For instance, it has been shown that distributed delays can stabilize a dynamical system [11], and the influence of delayed inhibitory feedback has been studied [12]. In regard to network synchrony, the question arises under what conditions this special form of network behavior can be maintained when the temporal delays are nonuniform.

Asymmetric time delays in the visual pathway can be a pathological condition, as they are associated with many diseases [13]. However, when feedback loops in biological systems have evolved to feature different latencies for feed-forward and feedback projections, this might provide a hint that asymmetric delays can also be beneficial to a system's functioning. In the avian visual system, the optic tectum is reciprocally coupled with the nucleus pars parvocellularis (Ipc), a subnucleus of the nucleus isthmi [14]. The coupled systems, tectum and Ipc, respond with synchronized oscillatory bursts to visual stimulation [15]. Remarkably, the Ipc axons projecting to the tectum are thick and myelinated (fast action potential propagation), whereas tectal neurons projecting to the Ipc possess comparatively thin axons and are unmyelinated (slow action potential propagation) [14]. The Ipc-to-tectum delay may thus be as short as a fraction of a millisecond, whereas the delay for the tectum-to-Ipc projection can be expected to be of the order of tens of milliseconds. It therefore seems natural to conjecture that the asymmetry in the delays may play a functional role in the feedback system.

To explore this conjecture we investigate a model system of two coupled Hopfield neurons [16] with asymmetric delays, described by the coupled first-order delay differential equations (DDE's)

$$
\begin{aligned}
\frac{du_1(t)}{dt} &= -u_1(t) + a_1 \tanh\left[u_2(t - \tau_2)\right], \\
\frac{du_2(t)}{dt} &= -u_2(t) + a_2 \tanh\left[u_1(t - \tau_1)\right].
\end{aligned}
\tag{3.1}
$$

Here, u_1 and u_2 denote the voltages of the Hopfield neurons and τ_1 and τ_2 are the signal propagation or processing time delays, while a_1 and a_2 describe the couplings between the two neurons. The system of DDE's (3.1) has a trivial stationary point at $u_1 = u_2 = 0$, the stability of which has been analyzed in detail, e.g., in ref. [17]. For $a_1 a_2 < -1$ the fixed point at the origin is asymptotically stable as long as the mean of the time delays $\tau \equiv (\tau_1 + \tau_2)/2$ does not exceed the critical value

41
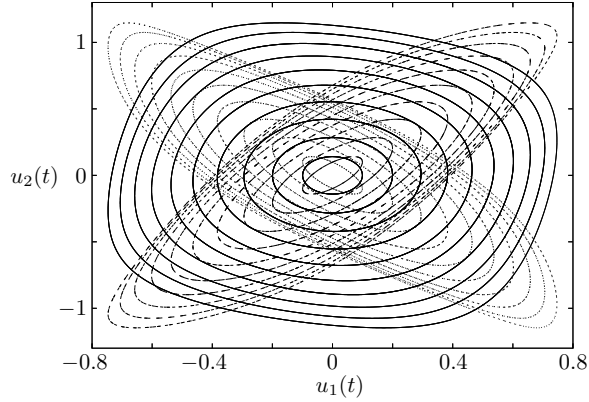
Figure 3.1: Numerical solutions to the system of DDE's (3.1) for the choice of parameters $a_1 = -1$ and $a_2 = 2$ and for different values of the time delays τ_1, τ_2 (transients not shown). Solutions for the case $\tau_1 = \tau_2$ are represented by solid lines. Dashed and dotted lines represent solutions for the cases $\tau_1 = 0$ and $\tau_2 = 0$, respectively. For each set of lines the value of the delay parameter $\epsilon = \sqrt{\tau - \tau_0}$ increases from the innermost limit cycle ($\epsilon = 0.1$) to the outermost limit cycle ($\epsilon = 1.0$) in increments of $\Delta\epsilon = 0.1$.

$\tau_0 \equiv \sin^{-1}[-2\omega_0/(a_1 a_2)]/(2\omega_0)$, where $\omega_0 = \sqrt{|a_1 a_2| - 1}$. When the sum of the delays is increased, the origin becomes unstable and a limit cycle emerges via a supercritical Hopf bifurcation at $\tau = \tau_0$. Note that the characteristic equation for the system (3.1), which determines the condition for a periodic solution to exist, only depends on the sum of the two delays. A linear stability analysis can thus provide no insight toward a possible role of asymmetry in the delays. Furthermore, standard methods for bifurcation analysis, as described, e.g., in refs. [6, 18] are only suitable for examining the nonlinear dynamical system in the immediate neighborhood of the bifurcation. In contrast to that, in this letter we aim at obtaining results that also hold for large delays, i.e., far away from the bifurcation.

We first investigate the effect of asymmetric time delays through numerical simulations. For a subsequent perturbation expansion we define the expansion parameter $\epsilon = \sqrt{\tau - \tau_0}$. Figure 3.1 shows numerical solutions of the system of DDE's (3.1) for different values of the time delays τ_1 and τ_2 and for the choice of parameters $a_1 = -1$, $a_2 = 2$. The amplitude of the limit cycle is only determined by the value of ϵ and thus remains unchanged when the temporal delays are chosen to be different. However, we observe that the phase between the periodic activities of $u_1(t)$ and $u_2(t)$ does depend on the asymmetry of the delays. In order to quantify this phase difference, we consider
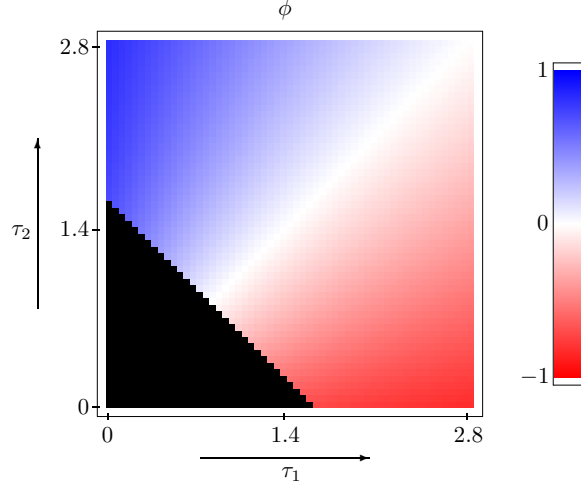
Figure 3.2: (Color) Plot of the phase shift between $u_1(t)$ and $u_2(t)$. Numerical results for the scalar product ϕ as given by (3.2) are color coded for combinations of τ_1 and τ_2 with $0 \leq \tau_{1/2} \leq 2.8$. Red and blue indicate negative and positive values of ϕ, respectively. In the black region, no periodic solution exists.

the normalized scalar product

$$\phi = \frac{\int_{T_0}^{T_0+T} dt \, u_1(t) u_2(t)}{\left[\int_{T_0}^{T_0+T} dt \, u_1(t) u_1(t) \int_{T_0}^{T_0+T} dt \, u_2(t) u_2(t) \right]^{1/2}} . \tag{3.2}$$

Numerical results for this quantity are shown in Fig. 3.2. We find that for time delays which are equal or at least not too asymmetric the scalar product ϕ is approximately zero, which corresponds to a phase shift of $\pi/2$ between $u_1(t)$ and $u_2(t)$, assuming that they can be described by sinusoidal functions. However, when the delays are asymmetric, the scalar product ϕ becomes larger in magnitude, being negative for $\tau_1 > \tau_2$ and positive for $\tau_2 > \tau_1$. Specifically, for $\tau_1 = 0$ the scalar product approaches unity for a growing delay τ_2, corresponding to in-phase synchronization between the the two components.

We now aim at achieving an approximate analytical calculation of ϕ. To this end, we first derive the perturbation series for the periodic solution $\mathbf{u}(t)$ and its angular frequency ω of the system (3.1) by applying the Poincaré-Lindstedt method [19]. Since a supercritical Hopf bifurcation occurs at $\tau = \tau_0$, we assume that the amplitude and frequency of the new periodic states are analytic in ϵ and expand them as $\mathbf{u}(t) = \epsilon \mathbf{U}(t) = \epsilon \left[\mathbf{U}^{(0)}(t) + \epsilon \mathbf{U}^{(1)}(t) + \ldots \right], \omega(\epsilon) = \omega_0 + \epsilon \omega_1 + \epsilon^2 \omega_2 + \ldots$. Furthermore, for convenience we introduce the rescaled independent variable $\xi = \omega(\epsilon)t$ and write
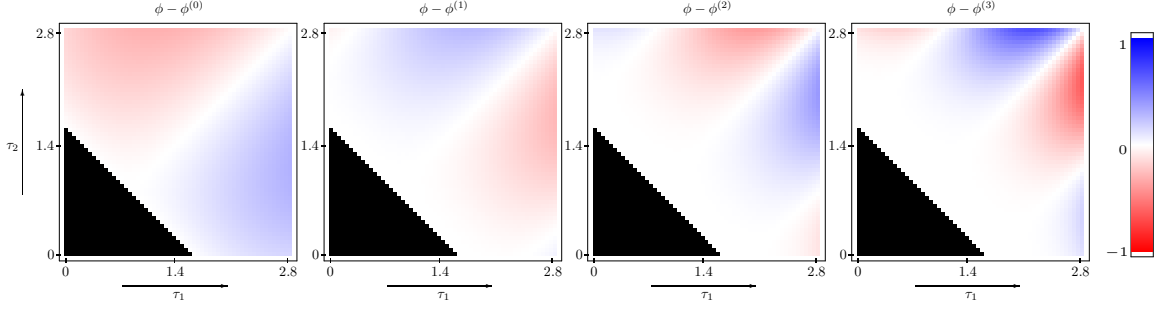
Figure 3.3: (Color) Perturbative results for the phase shift between $u_1(t)$ and $u_2(t)$. The color-coded plots show the difference between the numerical result from Fig. 3.2 and the perturbative results up to order g^3.

$\mathbf{U}(t) = \mathbf{V}(\xi)$. The expansion then proceeds in a way very similar to the approach in ref. [20], where the frequency of the limit cycle is calculated perturbatively for increasing mean of time delays. However, we introduce an additional parameter $\tilde{\tau}_1$, which is defined as the τ_1-value of the intersection point in the τ_1-τ_2 plane between the line that marks the boundary between the regions in which a periodic solution does or does not exist, and a line perpendicular to this boundary through a given point (τ_1, τ_2). To nth order in ϵ, we have to solve a system of differential equations of the form

$$
\begin{aligned}
\frac{dV_1^{(n)}(\xi)}{d\xi} &= -\frac{V_1^{(n)}(\xi)}{\omega_0} + \frac{a_1}{\omega_0} V_2^{(n)}[\xi - \omega_0(2\tau_0 - \tilde{\tau}_1)] + f_1^{(n)}(\xi) \,, \\
\frac{dV_2^{(n)}(\xi)}{d\xi} &= -\frac{V_2^{(n)}(\xi)}{\omega_0} + \frac{a_2}{\omega_0} V_2^{(n)}(\xi - \omega_0\tilde{\tau}_1) + f_2^{(n)}(\xi) \,,
\end{aligned}
\tag{3.3}
$$

where the inhomogeneity $\mathbf{f}^{(n)}(\xi)$ is determined by the solutions to previous orders. Since we require that the solution $\mathbf{V}^{(n)}(\xi)$ be periodic in ξ with period 2π, we can impose certain conditions on the inhomogeneity $\mathbf{f}^{(n)}(\xi)$. Namely, we demand that $\mathbf{f}^{(n)}(\xi)$ not contain terms that would lead to non-periodic solutions for $\mathbf{V}^{(n)}(\xi)$, i.e., $\mathbf{f}^{(n)}(\xi)$ must not contain secular terms. These conditions, which can be derived by expanding both the nth order limit cycle solution $\mathbf{V}^{(n)}(\xi)$ and the inhomogeneity $\mathbf{f}^{(n)}(\xi)$ into a Fourier series, read

$$
\begin{aligned}
a_2 \sin(\omega_0\tau_0)\alpha_{1,1}^{(n)} + \alpha_{2,1}^{(n)} \sin[\omega_0(\tau_0 - \tilde{\tau}_1)] + \beta_{2,1}^{(n)} \cos[\omega_0(\tau_0 - \tilde{\tau}_1)] &= 0 \,, \\
\alpha_{2,1}^{(n)} \cos[\omega_0(\tau_0 - \tilde{\tau}_1)] - \beta_{2,1}^{(n)} \sin[\omega_0(\tau_0 - \tilde{\tau}_1)] - a_2 \sin(\omega_0\tau_0)\beta_{1,1}^{(n)} &= 0 \,.
\end{aligned}
\tag{3.4}
$$

Here $\alpha_{1/2,1}^{(n)}$ and $\beta_{1/2,1}^{(n)}$ denote the coefficients of the cosine and sine terms in the Fourier expansion of the inhomogeneity $f_{1/2}^{(n)}(\xi)$, respectively. Imposing these conditions on the inhomogeneity in (3.3) allows us to determine the angular frequency correction ω_n and the Fourier expansion coefficients for $\mathbf{V}^{(n-2)}(\xi)$. To second order in ϵ we find

$$\omega_2 = -\frac{\omega_0^2}{\omega_0\tau_0 + \cos(\omega_0\tau_0)\sin(\omega_0\tau_0)} \,, \tag{3.5}$$

while ω_1 vanishes. This value is identical to the one found in ref. [20] depending only on ω_0 and τ_0 but not on τ_1 or τ_2. Since this observation holds to all orders, we thus find that the period of the oscillations is independent of any asymmetry in the time delays. Furthermore, we find that only even perturbative orders lead to nonvanishing contributions for both the angular frequency ω and the limit cycle $\mathbf{V}(\xi)$; we therefore define the new expansion parameter $g = \epsilon^2$. Denoting the expansion to order g^N of the quantity (3.2) by $\phi^{(N)}$, we find

$$
\begin{aligned}
\phi^{(1)} &= \frac{\cos[\omega_0(2\tau_0 - \tilde{\tau}_1)] - \omega_0\sin[\omega_0(2\tau_0 - \tilde{\tau}_1)]}{\text{sign}(a_1)\sqrt{1+\omega_0^2}} \\
&+ g\frac{2(\tau_0 - \tilde{\tau}_1)\omega_0^2\{\sin[\omega_0(2\tau_0 - \tilde{\tau}_1)] + \omega_0\cos[\omega_0(2\tau_0 - \tilde{\tau}_1)]\}^3}{\text{sign}(a_1)[\sin(2\omega_0\tau_0) + 2\omega_0\tau_0](1+\omega_0^2)^{3/2}} \,.
\end{aligned}
\tag{3.6}
$$

Focusing on the choice of parameters $a_1 = -1$, $a_2 = 2$, which leads to $\omega_0 = 1$, $\tau_0 = \pi/4$, we can determine the expansion coefficients for $\phi^{(N)}$ up to the third order. Figure 3.3 shows a comparison of our perturbative results and the numerical result from Fig. 3.2. For small time delays, the accuracy of the results from the perturbation expansion is good and improves with increasing order. However, as g increases, the perturbative results cease to converge and no longer provide an acceptable approximation. As is typical for perturbative methods, our approach has yielded a divergent series. In order to improve the quality of our results, we now perform a resummation of the perturbative expansion employing variational perturbation theory (VPT).

VPT is a nonperturbative approximation scheme based on a variational approach due to Feynman and Kleinert [21], which has been systematically developed over the last few years, establishing its applicability in various fields of physics [20, 22–26]. VPT permits the evaluation of a divergent series of the form $f^{(N)}(g) = \sum_{n=0}^{N} a_n g^n$ and yields a strong-coupling expansion of the generic form $f(g) = g^{p/q}\sum_{m=0}^{M} b_m g^{-2m/q}$. Here, p and q are real growth parameters characterizing the
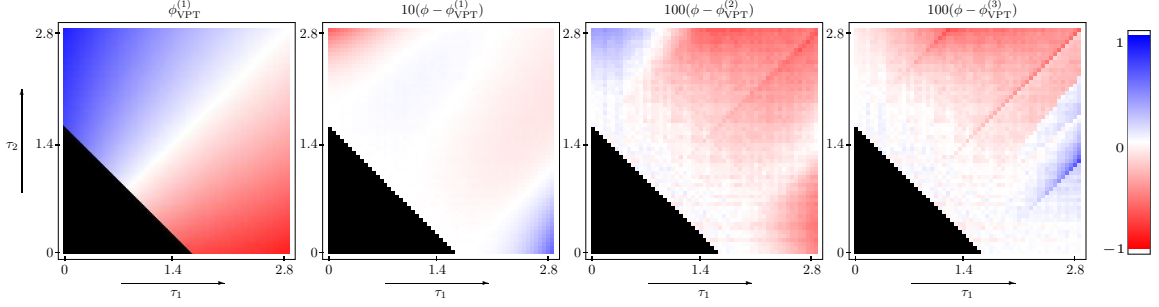
Figure 3.4: (Color) VPT results for the phase shift between $u_1(t)$ and $u_2(t)$. The first color-coded plot shows the first-order-VPT result as given by (3.8). The three other plots show the difference between the numerical result and the results from the first three orders in VPT. For clarity, this difference has been augmented by a factor of 10 and 100 in the results for the first and for both the second and third order, respectively

strong-coupling behavior. The convergence of the series after resummation is exponentially fast and uniform with respect to other system parameters such as temperature, coupling constants, spatial dimensions, etc. [27].

In order to perform the resummation, one introduces a variational parameter K for the perturbation series according to Kleinert's square-root trick [23]. The series is thus transformed to the expression

$$f^{(N)}(g, K) = \sum_{n=0}^{N} a_n g^n K^{p-nq} \sum_{k=0}^{N-n} \binom{(p-nq)/2}{k} \left(\frac{1}{K^2} - 1\right)^k,$$ (3.7)

derived in detail in ref. [20]. The influence of the variational parameter K is then optimized according to the principle of minimal sensitivity [28]; i.e., the optimized value $K^{(N)}$ is determined by solving for the roots of the first or higher derivatives of $f^{(N)}(g, K)$ with respect to K. The Nth order VPT approximation is then obtained by evaluating (3.7) at this optimized value: $f_{\mathrm{VPT}}^{(N)}(g) = f^{(N)}(g, K^{(N)})$. This variational result generally holds for all values of the coupling constant g. Furthermore, by considering the limit of large g, it allows the extraction of the strong-coupling coefficients b_m.

In our case of the perturbation series for ϕ, the values of the growth parameters p and q turn out to be the same as those that we determined in ref. [20] for the angular frequency, namely $p = -2$,

$q = 2$. Our first-order result after resummation then reads

$$\phi_{\text{VPT}}^{(1)}(g) = \frac{(2+\pi)(1 - 2\cos\tilde{\tau}_1 \sin\tilde{\tau}_1)}{\sqrt{2}}$$
$$[(2+\pi)(\cos\tilde{\tau}_1 - \sin\tilde{\tau}_1) + g(\pi - 4\tilde{\tau}_1)](\cos\tilde{\tau}_1 + \sin\tilde{\tau}_1)]^{-1}. \qquad (3.8)$$

The first color-coded plot in Fig. 3.4 shows a graphical representation of this result. The agreement with the numerical result from Fig. 3.2 is excellent. While the second VPT order provides a significant improvement when compared with the first order result, third order results are slightly superior to those of second order.

In conclusion, our investigation of a neuronal model system shows that asymmetric temporal delays can control the phase in a feedback loop and lead to synchronous oscillations. Specifically, in-phase and anti-phase synchrony arises when the delays are maximally asymmetric. Furthermore, after a variational resummation of the perturbation series for ϕ, we have a very accurate approximate result for this quantity even in low orders and throughout the full τ_1-τ_2 plane.

References

[1] A. Pikovsky, M. Rosenblum, and J. Kurths, *Synchronization: A Universal Concept in Nonlinear Sciences* (Cambridge Univ. Press, Cambridge, 2003).

[2] S. Strogatz, *Sync: The Emerging Science of Spontaneous Order* (Hyperion, New York, NY, 2003).

[3] U. an der Heiden, J. Math. Bio. **8**, 345 (1979).

[4] B. D. Coleman and G. H. Renninger, SIAM J. Appl. Math. **31**, 111 (1976); J. Theor. Bio. **51**, 243 (1975).

[5] K. P. Hadeler and J. Tomiuk, Arch. Rat. Mech. Anal. **65**, 87 (1977).

[6] W. Wischert, A. Wunderlin, A. Pelster, M. Olivier, and J. Groslambert, Phys. Rev. E **49**, 203 (1994).

[7] M. Schanz and A. Pelster, Phys. Rev. E **67**, 056205 (2003).

[8] E. L. Babcock and R. M. Westervelt, Physica D **28**, 305 (1987); J. Bélair, J. Dyn. Differ. Equ. **5**, 607 (1993); K. Gopalsamy and X. He, Physica D **76**, 344 (1994); J. Bélair, S. A. Campbell, and P. van den Driessche, SIAM J. Appl. Math. **56**, 245 (1996); R. Ritz and T. J. Sejnowski, Curr. Opin. Neurobiol. **7**, 536 (1997).

[9] L. Chen and K. Aihara, IEEE T. Circuits-I **49**, 602 (2002); J. Lewis, Curr. Biol. **13**, 1398 (2003); N. A. M. Monk, Curr. Biol. **13**, 1409 (2003).

[10] K. Gopalsamy, *Stability and Oscillations in Delay Differential Equations of Population Dynamics* (Kluwer, Dordrecht, 1992); R. M. Nisbet and W. S. C. Gurney *Modelling Fluctuating Populations* (Wiley, Chichester, 1982).

[11] C. W. Eurich, A. Thiel, and L. Fahse, Phys. Rev. Lett. **94**, 158104 (2005); J. Pomplun, A. G. Balanov, and E. Schöll, Phys. Rev. E **75**, 040101 (2007).

[12] L. Glass and M. C. Mackey, *From Clocks to Chaos: The Rhythms of Life* (Princeton University Press, Princeton, 1988); J. Foss, F. Moss, and J. Milton, Phys. Rev. E **55**, 4536 (1997); B. Doiron, M. J. Chacron, L. Maler, A. Longtin, and J. Bastian, Nature **421**, 539, (2003); B. Lindner, B. Doiron, and A. Longtin, Phys. Rev. E **72**, 061919 (2005).

[13] D. S. Mojon, K. M. Rösler, and H. Oetliker, Ophthalmology **105**, 1337 (1998).

[14] Y. Wang, H. Luksch, N. C. Brecha, and H. J. Karten, J. Comp. Neurol. **494**, 7 (2006).

[15] G. Marín, J. Mpodozis, E. Sentis, T. Ossandón, and J. C. Letelier, J. Neurosci. **25**, 7081 (2005).

[16] J. J. Hopfield, Proc. Natl. Acad. Sci. U.S.A. **81**, 3088 (1984); C. M. Marcus and R. M. Westervelt, Phys. Rev. A **39**, 347 (1989).

[17] J. Wei and S. Ruan, Physica D **130**, 255 (1999).

[18] B. F. Redmond, V. G. LeBlanc, and A. Longtin, Physica D **166**, 131 (2002).

[19] N. MacDonald, *Time Lags in Biological Models*, Lecture Notes in Biomathematics Vol. 27 (Springer-Verlag, Berlin, 1978).

[20] S. F. Brandt, A. Pelster, and R. Wessel, Phys. Rev. E **74**, 036201 (2006).

[21] R. P. Feynman and H. Kleinert, Phys. Rev. A **34**, 5080 (1986).

[22] H. Kleinert, Phys. Lett. A **173**, 332 (1993).

[23] H. Kleinert, *Path Integrals in Quantum Mechanics, Statistics, Polymer Physics, and Financial Markets*, Fourth Edition (World Scientific, Singapore, 2006); Phys. Rev. D **57**, 2264 (1998).

[24] H. Kleinert and V. Schulte-Frohlinde, *Critical Properties of Φ^4-Theories* (World Scientific, Singapore, 2001); Chap. 19.

[25] W. Janke, A. Pelster, H.-J. Schmidt, and M. Bachmann (Eds.), *Fluctuating Paths and Fields – Dedicated to Hagen Kleinert on the Occasion of his 60th Birthday* (World Scientific, Singapore, 2001).

[26] W. Janke and H. Kleinert, Phys. Rev. Lett. **75**, 2787 (1995).

[27] A. Pelster, H. Kleinert, and M. Schanz, Phys. Rev. E **67**, 016604 (2003); M. Bachmann, H. Kleinert, and A. Pelster, Phys. Lett. A **261**, 127 (1999); M. Bachmann, H. Kleinert, and A. Pelster, Phys. Rev. A **62**, 052509 (2000); J. Dreger, A. Pelster, and B. Hamprecht, Eur. Phys. J. B **45**, 355 (2005); F. Weißbach, A. Pelster, and B. Hamprecht, Phys. Rev. E **66**, 036129 (2002); C. M. Bender, A. Pelster, and F. Weißbach, J. Math. Phys. **43**, 4202 (2002); S. F. Brandt, H. Kleinert, and A. Pelster, J. Math. Phys. **46**, 032101 (2005); S. F. Brandt and A. Pelster, J. Math. Phys. **46**, 112105 (2005).

[28] P. M. Stevenson, Phys. Rev. D **23**, 2916 (1981).

Chapter 4

Distributed delays stabilize neural feedback systems

We consider the effect of distributed delays in neural feedback systems. The avian optic tectum is reciprocally connected with the nucleus isthmi. Extracellular stimulation combined with intracellular recordings reveal a range of signal delays from 4 to 9 ms between isthmotectal elements. This observation together with prior mathematical analysis concerning the influence of a delay distribution on system dynamics raises the question whether a broad delay distribution can impact the dynamics of neural feedback loops. For a system of reciprocally connected model neurons, we found that distributed delays enhance system stability in the following sense. With increased distribution of delays, the system converges faster to a fixed point and converges slower toward a limit cycle. Further, the introduction of distributed delays leads to an increased range of the average delay value for which the system's equilibrium point is stable. The enhancement of stability with increasing delay distribution is caused by the introduction of smaller delays rather than the distribution per se.

4.1   Introduction

The signal flow in the brain is not just feedforward; rather, feedback dominates most neural pathways [1]. Often pairs of reciprocally connected neurons are spatially separate by several millimeters.

For instance, the primate corticothalamic feedback loop extends over a distance of approximately 100 mm. Thus, for a typical action potential speed of 1 mm/ms we expect a signal delay of 100 ms. When signal delays are larger than the neural response time, complex loop dynamics emerge [2–4].

For reciprocally connected populations of neurons, large delays can introduce another dimension, namely the distribution of delay times. Such a distribution could be an epiphenomenon in the evolution of larger brains, or it could be of adaptive significance. Work from applied mathematics states an influence of the distribution of delay times on system dynamics [5–10]. Intrigued by the latter possibility, we asked two questions: What is the distribution of delay times in an experimentally accessible neural feedback system? What is the impact of distributed delays on a mathematically tractable neural model feedback system?

We measured the distribution of delay times in the isthmotectal feedback system of birds [Fig. 4.1(a)] [11, 12]. The avian isthmic nuclei (parabigeminal nucleus in mammals) receive a topographically organized projection from the tectum (superior colliculus in mammals), to which they project back and have been conjectured to mediate spatiotemporal attentional mechanisms [13–15]. The isthmic nuclei in birds consist of three substructures: pars parvocellularis (Ipc), pars magnocellularis (Imc), and pars semilunaris (SLu) that are spatially separated from the tectum [16, 17]. In response to visual stimulation, the Ipc neurons undergo a transition from quiescence to rhythmic firing [15, 18]. Delays can drive a neural feedback loop over a stability boundary resulting in oscillatory behavior [19–24]. To elucidate the impact of a delay distribution on the system dynamics, we investigated, through numerical simulations and mathematical analysis, a model of reciprocally coupled neurons with distributed delays.

4.2   Measured distribution of delays

To measure the signal delays between pairs of isthmotectal elements, we obtained intracellular whole-cell recordings from identified neurons in a midbrain slice preparation and stimulated groups of presynaptic neurons or axons with brief electrical pulses delivered extracellularly [Fig. 4.1(b)]. Neurons were identified by their location within the midbrain slice preparation and for a subset of recorded neurons we obtained additional identification via intracellular fills [16, 17].

A subpopulation of tectal layer 10 (L10) neurons project to both the ipsilateral Ipc and Imc in
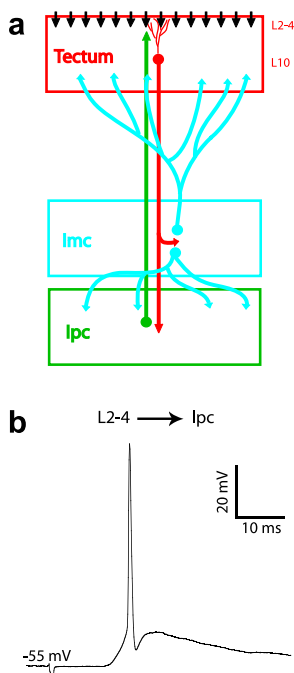
Figure 4.1: (Color) Schematic of the isthmotectal circuitry and representative response to electrical stimulation. **(a)** Schematic of the isthmotectal circuitry. RGC axons (black arrows) enter in upper tectal layers. A subpopulation of tectal L10 neurons (red) projects to Imc and Ipc. The Imc nucleus consists of two populations of neurons (blue); one projecting broadly back to lower tectal layers and one projecting broadly to the Ipc nucleus. Ipc neurons (green) project back to the tectum with axons reaching into upper tectal layers. **(b)** Intracellular recording from an Ipc neuron in response to electrical stimulation in tectal L2-4.

a topographic fashion [16, 17, 25–28]. Their apical dendrite courses straight up to layer 2 with few ramifications, and basal dendrites reach down to the border of layer 13. Retinal axon terminals overlap with the apical dendrite in tectal layers 2 to 7 [29, 30]. We placed a stimulus electrode in layer 2 to 4 (L2-4) and recorded from L10 neurons with whole-cell recordings in response to L2-4 stimulation. The delays from the beginning of the stimulus pulse to the onset of the L10 response ranged from 4 to 15 ms with a mean delay of 6.9 ms and a standard deviation (SD) of 1.3 ms ($n = 15$ cells) [Fig. 4.2(a)]. Tectal L10 neurons are a heterogeneous population [17]. Therefore, only filled L10 neurons with axons originating from the dendrite were included in this analysis. Since L10 neuron dendrites can reach up to L2, the possibility of unwanted direct electrical, rather than synaptic, stimulation of L10 neuron dendritic endings arises. At the end of a recording session, we evaluated the nature of stimulation by blocking chemical synaptic transmission via the block of Ca-channels by replacing Ca^{2+} in the saline with Mg^{2+}.

52
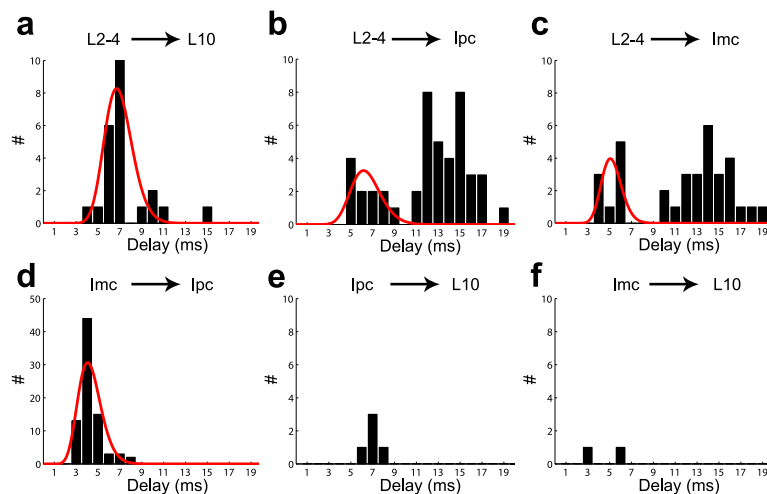
Figure 4.2: (Color) Measured distribution of signal delays between isthmotectal elements and plot of the corresponding gamma distribution [red curves in **(a)** through **(d)**] with the same mean and standard deviation. **(a)** L2-4 to L10. **(b)** L2-4 to Ipc. **(c)** L2-4 to Imc. **(d)** Imc to Ipc. **(e)** Ipc to L10. **(f)** Imc to L10.

We measured signal delays between optic tectum and individual Ipc neurons via RGC axon stimulation or L10 neuron dendrite stimulation, with a stimulus electrode placed in tectal L2-4. In the first case, the group of stimulated RGC axons stimulates a population of L10 neurons, which in turn stimulates a large number of Ipc neurons. In the second case, L10 neurons are stimulated directly. This stimulus paradigm provided a high chance of recording from an Ipc neuron that received tectal synaptic inputs. The delays from the beginning of the stimulus pulse to the onset of the Ipc neuron response ranged from 5 to 19 ms ($n = 17$ cells) [Fig. 4.2(b)]. As expected from the stimulus paradigm, the distribution of delays is bimodal. We suspect that the first bump (5 to 9 ms range) is dominated by direct L10 dendrite stimulation (mono-synaptic pathway L10-Ipc); whereas the second bump (11 to 19 ms range) is dominated by RGC axon stimulation, which initiates the bi-synaptic pathway RGC-L10-Ipc. From the first bump in the histogram we estimate a mean delay of 6.5 ms and a SD of 1.4 ms for the mono-synaptic pathway L10-Ipc. Since Ipc neuron axons can reach up to L2 [17], the possibility of unwanted direct electrical stimulation of Ipc axons arises. At the end of a recording session, we evaluated the nature of stimulation by blocking chemical synaptic transmission via replacing Ca^{2+} in the saline with Mg^{2+}.

Using a stimulus paradigm similar to the one described above, we measured signal delays between L10 and individual Imc neurons. We placed a stimulus electrode in L2-4 for stimulation of

RGC axons or L10 neuron dendrites and recorded from Imc neurons with whole-cell recordings in response to L2-4 stimulation. The signal delays ranged from 4 to 19 ms ($n = 17$ cells) and the distribution was bimodal [Fig. 4.2(c)]. As described above, the first bump is likely to be dominated by the mono-synaptic pathway (L10-Imc), whereas the second bump is likely to be dominated by the bi-synaptic pathway (RGC-L10-Imc). The first bump in the histogram yielded a mean delay of 5.2 ms and a SD of 0.9 ms. Since Imc axons terminate in tectal layers 10 to 13 [16], the possibility of direct Imc axon stimulation via stimulus electrodes in L2-4 does not arise.

The Imc nucleus consists of two cell types, one of which projects to the Ipc nucleus with a broad and dense projection of axonal arbors [16, 31, 32]. We positioned a stimulus electrode in the Imc nucleus and recorded from Ipc neurons with whole-cell recordings in response to Imc stimulation. The signal delays ranged from 3 to 8 ms with a mean delay of 4.3 ms and a SD of 1.1 ms ($n = 12$ cells) [Fig. 4.2(d)]. Care had to be taken about the interpretation of the Imc stimulation experiments. The stimulus electrode in the Imc nucleus stimulates 4 elements: L10 neuron axons, Ipc neuron axons passing through the Imc nucleus, and two populations of Imc neurons; one projecting to tectum and the other projecting to Ipc. To filter out the Imc to Ipc synaptic connection, we stimulated in an area of the Imc nucleus that did not correspond to the topographic location of the recorded Ipc neuron, thus avoiding both antidromic stimulation of the axon from the recorded Ipc neuron as well as avoiding orthodromic stimulation of the L10 axons passing through the Imc nucleus on their way to the same location in the Ipc nucleus. At the end of a recording session, we applied bicuculline to verify that the synaptic inputs to the recorded Ipc neuron were indeed from the stimulated GABAergic Imc neurons (GABA: gamma-aminobutyric acid). The responses disappeared when 100 μM bicuculline was added to the bath (data not shown) thus (i) indicating that the responses were of synaptic origin (rather than antidromic Ipc or L10 axon stimulation) and (ii) confirming that GABA is the transmitter as had been suggested by anatomical studies [16].

The Ipc nucleus has topographical reciprocal connections with the tectum [17, 26, 27, 33, 34]. The efferents from Ipc have large calibre axons and terminate in a columnar manner ranging from layers 2 to 12 [Fig. 4.1(a)] [17, 25–27, 31, 32]. We applied local extracellular electrical stimulation of a group of Ipc neurons with a stimulus electrode placed in the Ipc nucleus. Such extracellular electrical stimulation also stimulates L10 axons antidromically. The fast L10 neuron antidromic responses were distinguishable from the much slower and long-lasting synaptic responses. The

additional direct activation of Imc axons in the Ipc nucleus does not interfere with this experiment, since the population of Imc neurons projecting to the Ipc nucleus is different from the population of Imc neurons projecting to the tectum. The yield for finding Ipc to L10 synaptic responses turned out to be very low. For the few cases we found, the delays ranged from 6 to 8 ms ($n = 5$ cells) [Fig. 4.2(e)].

The projection from individual Imc neurons to tectal layers 10 to 13 is broad and sparse [16]. We positioned a stimulus electrode in the Imc nucleus and recorded from L10 neurons with whole-cell recordings in response to Imc stimulation. The yield for finding Imc to L10 synaptic responses turned out to be very low. For the two connected pairs we found, the signal delays were 3 and 6 ms ($n = 2$ cells) [Fig. 4.2(f)]. The low yield and the interpretation of these experiments require some explanation. As mentioned above, a stimulus electrode in the Imc nucleus will stimulate four elements. To filter out the Imc to L10 synaptic connection, we stimulated in an area of the Imc nucleus that did not correspond to the topographic location of the recorded L10 neuron, thus avoiding both antidromic stimulation of the axon from the recorded L10 neuron as well as avoiding orthodromic stimulation of the Ipc axons passing through the Imc nucleus on their way to the same location of the tectum. At the end of a recording session, we applied bicuculline to verify that the synaptic inputs to the recorded L10 neuron were indeed from the stimulated GABAergic Imc neurons. For the two neurons, the responses disappeared when 100 μM bicuculline was added to the bath (data not shown) thus indicating that the responses were of synaptic origin; rather than antidromic L10 or orthodromic Ipc axon stimulation.

In summary, these data show that the signal delays between isthmotectal elements are distributed ranging from 4 to 9 ms.

4.3   Distributed delays and the dynamics of neural feedback systems

What is the impact of distributed delays on a mathematically tractable neural model feedback system? To interpret the potential impact of the measured distribution of delays on the dynamics of neural feedback systems, we investigated a model system of two coupled Hopfield neurons
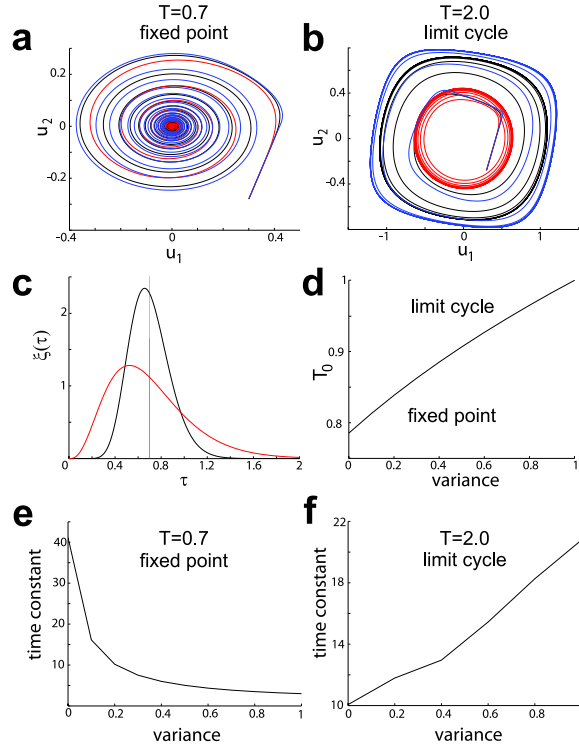
Figure 4.3: (Color) Mean delays and attractors. **(a)**, **(b)** Dynamics of the two-neuron model system for gamma distributions with mean delay values of $T = 0.7$ [**(a)**, fixed point] and [**(b)**, limit cycle], respectively. For both cases, the standard deviation is 0% (blue), 25% (black), and 50% (red) of the mean delay. The initial condition is $u_1(t) = 0.30$ and $u_2(t) = -0.28$ for $-\tau \leq t \leq 0$. **(c)** Gamma distribution for a mean delay value of $T = 0.7$ and a standard deviation of 0% (blue), 25% (black), and 50% (red) of the mean delay. **(d)** Critical mean delay, T_0, where the Hopf bifurcation takes place, plotted against variance. **(e)**, **(f)** Time constant for reaching the attractor for $T = 0.7$ (fixed point) and $T = 2.0$ (limit cycle), respectively, plotted against the variance of the gamma distribution.

[20, 22, 23, 35], described by the first-order delay differential equations

$$
\begin{aligned}
\frac{du_1(t)}{dt} &= -u_1(t) + a_1 \tanh[u_2(t - \tau_2)], \\
\frac{du_2(t)}{dt} &= -u_2(t) + a_2 \tanh[u_1(t - \tau_1)].
\end{aligned}
\tag{4.1}
$$

Here, $u_1(t)$ and $u_2(t)$ denote the voltages of the model neurons and τ_1 and τ_2 are the temporal delays, while a_1 and a_2 describe the coupling strength between the two neurons. In this analysis, the time variable is dimensionless. Translation to real time can be made by multiplying the dimensionless time variable with a membrane time constant, RC. The system of delay differential equations has a trivial stationary point at the origin, $u_1 = u_2 = 0$ [Fig. 4.3(a)]. For $a_1 a_2 \leq -1$, the fixed

point at the origin is asymptotically stable as long as the mean of the time delays $(\tau_1 + \tau_2)/2$ does not exceed a critical value τ_0 [22, 36]:

$$\frac{\tau_1 + \tau_2}{2} < \tau_0 = \frac{1}{2\sqrt{|a_1 a_2| - 1}} \sin^{-1} \frac{2\sqrt{|a_1 a_2| - 1}}{|a_1 a_2|} \,. \tag{4.2}$$

The critical value τ_0 is determined by combinations of the product of the couplings alone [Eq. (4.2)]. For couplings of opposite signs (e.g., $a_1 a_2 \leq -1$) and when the delays are increased, the origin becomes unstable and a limit cycle emerges via a supercritical Hopf bifurcation at $(\tau_1 + \tau_2)/2 = \tau_0$ [Fig. 4.3(b)]. The critical value, τ_0, decreases with decreasing value of the product of the couplings $a_1 a_2$ below -1. In other words, oscillations can be achieved by either increasing the delays or by increasing the absolute value of the coupling strengths of opposite signs.

For a distribution of delays we replace the coupling term in (4.1) with a weighted sum over similar terms but with different delays

$$\begin{aligned}
\frac{du_1(t)}{dt} &= -u_1(t) + a_1 \int_0^\infty d\tau \, \xi(\tau) \tanh[u_2(t - \tau)] \,, \\
\frac{du_2(t)}{dt} &= -u_2(t) + a_2 \int_0^\infty d\tau \, \xi(\tau) \tanh[u_1(t - \tau)] \,.
\end{aligned} \tag{4.3}$$

The delay kernel $\xi(\tau)$ is normalized to satisfy $\int_0^\infty d\tau \, \xi(\tau) = 1$. For simplicity, we chose the delay kernels to be identical for both legs of the loop. We chose the delay kernel to be a gamma distribution,

$$\xi(\tau) = \frac{(T/\nu)^{T^2/\nu}}{\Gamma(T^2/\nu)} \tau^{T^2/\nu - 1} e^{-T\tau/\nu} \,, \tag{4.4}$$

where T is the mean delay, ν is the variance of the gamma distribution, and the gamma function is defined as $\Gamma(x) = \int_0^\infty t^{x-1} e^{-t} dt$. The gamma distribution was chosen because it has the biologically plausible feature to vanish for delays approaching 0 [Fig. 4.3(c)]. For the coupling strengths we chose $a_1 = -2$ and $a_2 = 1$ for all simulations.

The parameters to vary are the mean delay, T, and the variance, ν, of the gamma distribution. As these parameters are changed, the fixed point at the origin changes from a stable fixed point to an unstable fixed point surrounded by a stable limit cycle and vice-versa (Hopf bifurcation). This
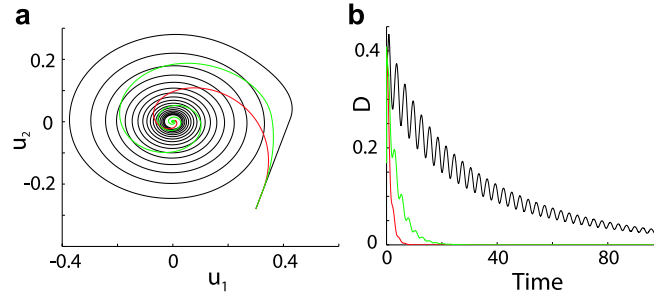
Figure 4.4: (Color) Dynamics of the two-neuron model system with discrete delays. **(a)** Dynamics of the system with two fixed delays of 0.1 and 0.7 (green); one fixed delay of 0.1 (red); and one fixed delay of 0.7 (black). **(b)** Distance $D(t) = \sqrt{u_1^2(t) + u_2^2(t)}$ from (0, 0) vs. time for the above cases.

transition takes place when the roots, λ, of the characteristic equation for the system (4.3),

$$\lambda^2 + 2\lambda + 1 - a_1 a_2 \left(1 + \frac{\lambda \nu}{T}\right)^{2T^2/\nu} = 0 \,, \tag{4.5}$$

are purely imaginary. The characteristic equation is obtained by demanding that the solution to (4.3) behaves as $u_1(t) = Ae^{\lambda t}$, $u_2(t) = Be^{\lambda t}$ near the fixed point. Substituting $\lambda = i\omega$, where ω is real, we have

$$-\omega^2 + 2i\omega + 1 - a_1 a_2 \left(1 + \frac{i\omega \nu}{T}\right)^{-2T^2/\nu} = 0 \,. \tag{4.6}$$

Separating real and imaginary parts, we get two equations from which we can numerically eliminate ω. However, there are multiple solutions for this. For a given variance ν, the solution with the minimum positive mean delay T, determines the critical mean delay T_0 at which the fixed point at the origin loses its stability and a stable limit cycle emerges. Our analysis shows that the introduction of distributed delays (increasing variance) leads to a smaller limit cycle [Fig. 4.3(b)]. Furthermore, the critical mean delay T_0 increases with increasing variance [Fig. 4.3(d)].

To estimate the time constant for reaching an attractor, we calculated the distance $D_\theta(t) = \sqrt{u_1^2(t) + u_2^2(t)}$ from the origin along a given polar angle θ in the u_1-u_2 space. Assuming an exponential dependence, a fit of an exponential function to the simulated $D_\theta(t)$ values provided the time constant for that polar angle. We repeated the procedure for 360 polar angles in 1-deg increments and took the final time constant to be the mean of the 360 time constants at given polar

angles. This analysis shows that increasing variance makes the convergence to the fixed points faster [Fig. 4.3(e)] and the convergence to limit cycles slower [Fig. 4.3(f)].

In summary, distributed delays increase the parameter region with fixed-point behavior and accelerate the convergence to the fixed point.

The enhanced fixed-point stability with distributed delays actually comes from the contribution of the smaller delays, rather than the distribution per se. To illustrate this insight, we compare the dynamics of three systems with delays given by one or two superimposed delta-distributions with peaks at: (i) $\tau = 0.7$, (ii) both $\tau = 0.1$ and $\tau = 0.7$, and (iii) $\tau = 0.1$ (Fig. 4.4). The distributed system (ii) converges faster than system (i), but the distributed system (ii) converges slower than system (iii). In other words, adding a longer delay of $\tau = 0.7$ to the $\tau = 0.1$ system slows the convergence, whereas adding a shorter delay of $\tau = 0.1$ to the $\tau = 0.7$ system accelerates the convergence. Thus, it is not the distribution of delays per se, but the contribution of shorter delays in the distribution that enhances fixed-point stability.

4.4 Discussion

For large brains with finite signal propagation velocities, delays are a fact of life. In some feedforward pathways, such as the vertebrate optic nerve, delays can be specific to the retinal ganglion cell type thus leading to differences of arrival time for different retinal representations of the visual stimulus [37–40]. In other feedforward sensory pathways, such as the avian nucleus laminaris, delays are used explicitly to evaluate interaural time differences [41]. Delays in feedback loops play a fundamentally different role, as they can determine the dynamical behavior of the system [42, 43]. Specifically, for delays smaller than a critical value a neural feedback system may converge toward a steady-state, whereas for delays larger than the critical value the system may oscillate [44, 45]. In nonlinear systems, the distribution of a system parameter can have unexpected effects on the systems dynamics [46–48]. Consequently, if delay is a relevant parameter in neural feedback systems, as stated above, it is important to investigate the impact of delay distributions on the system dynamics.

Parameters in biological system are usually distributed over some range. Therefore, these systems must be robust in the sense that the parameter variability should not detain the biological sys-

tem from functioning correctly. Moreover, a system architecture in which the parameter variability actually enhances the system's performance would be particularly desirable. In this study, we have quantified the distribution of delays in the avian isthmotectal feedback loop. Furthermore, by investigating a mathematical model of coupled neurons with distributed delays, we have demonstrated that distributed delays enhance the stability of the system, where the stabilizing effect arises from the contribution of smaller delays introduced through the delay distribution. Since the functional role of the isthmotectal feedback loop remains mostly unclear to date, it is not obvious whether this stabilizing effect is beneficial to the system's functioning. Further understanding of the neuronal processes in the isthmotectal feedback loop will be necessary to answer this question.

4.5   Experimental methods

White Leghorn chick hatchlings (Gallus gallus) of less than 3 days of age were used in this study. All procedures used in this study were approved by the local authorities and conform to the guidelines of the National Institutes of Health on the Care and Use of Laboratory Animals. Animals were injected with ketamine (40 mg per kg, i.m.). Brain slices of the midbrain were prepared following published protocols [49–53]. Briefly, preparations were done in 0 °C, oxygenated, and sucrose-substituted saline (240 mM sucrose, 3 mM KCl, 5 mM $MgCl_2$, 0.5 mM $CaCl_2$, 1.2 mM NaH_2PO_4, 23 mM $NaHCO_3$, and 11 mM D-glucose). After decapitation, the brains were removed from the skull, and the forebrain, cerebellum, and medulla oblongata were discarded. A midsagittal cut was used to separate the tectal hemispheres. The tectal hemispheres were sectioned at 500 μm on a tissue slicer (Vibroslice, Camden and VF-200, Precisionary Instruments) in either the transverse or the horizontal plane. Slices were collected in oxygenated saline (120 mM NaCl, 3 mM KCl, 1 mM $MgCl_2$, 2 mM $CaCl_2$, 1.2 mM NaH_2PO_4, 23 mM $NaHCO_3$, and 11 mM D-glucose) and kept submerged in a chamber that was bubbled continuously with carbogen (95% oxygen, 5% CO_2) at room temperature. The slice was then transferred to a recording chamber (RC-26G, Warner Instruments) mounted on a fixed stage upright microscope equipped with DIC optics (BX-51WI, Olympus). The slice was held gently to the bottom of the chamber with an anchor of nylon threads, and the chamber was perfused continuously with oxygenated saline at room temperature. The cells in L10, Imc, and Ipc are visible with DIC optics.

Local electrostimulation was achieved by inserting bipolar tungsten electrodes under visual control into either the upper tectal retinorecipient layers (2 to 4), layer 5b, or the isthmic nuclei Ipc or Imc with a three-axis micromanipulator (U-31CF, Narishige). Electrodes were custom-built from 50-μm diameter, insulated tungsten wires (California Fine Wire) that were glued together with cyanoacrylate and mounted in glass microcapillaries for stabilization. The wires protruded several hundred m from the capillaries, and the tips were cut at an angle. Stimulus isolators (Isolated Pulse Stimulator 2100, AM Systems) generated biphasic current pulses (20 - 200 μA, 500 μs).

Whole-cell recordings were obtained with glass micropipettes pulled from borosilicate glass (1.5 mm OD, 0.86 mm ID, AM Systems) on a horizontal puller (P-97, Sutter Instruments and DMZ Universal Puller, Zeitz Instruments) and were filled with a solution containing 100 mM K-Gluconate, 40 mM KCl, 10 mM HEPES, 0.1 mM $CaCl_2$, 2 mM $MgCl_2$, 1.1 mM EGTA, 2 mM Mg-ATP, pH adjusted to 7.2 with KOH. Electrodes were advanced through the tissue under visual guidance with a motorized micromanipulator (MP-285, Sutter Instruments) while constant positive pressure was applied and the electrode resistance was monitored by short current pulses. Once the electrode had attached to a membrane and formed a seal, access to the cytosol was achieved by brief suction. Whole-cell recordings were performed with the amplifier (Axoclamp 2B, Axon Instruments and SEC-05L, npi-electronic) in the bridge mode (current clamp). The series resistance was estimated by toggling between the bridge and the DCC (discontinuous current clamp) mode. The series resistance was compensated with the bridge balance. Analog data were low-pass filtered (4-pole Butterworth) at 1 kHz, digitized at 5 kHz, stored, and analyzed on a PC equipped with an PCI-MIO-16E-4 and LabView software (both National Instruments).

Labeling of a subset of recorded neurons was carried out as described previously [50–52, 54]. In brief, whole-cell patch recordings were obtained as described above. Additionally, the electrode solution contained 0.5% Biocytin (w/v) to label the recorded neurons. Individual cells were filled intracellularly with 2 nA of positive current over 3 minutes. After recording and labeling, slices were kept in oxygenated ACSF for an additional 30 minutes and subsequently fixed by immersion in 4% paraformaldehyde in PB for at least 4 hours. Slices were then washed in phosphate buffer (PB, 0.1 M, pH 7.4) for at least 4 hours, immersed in 15% sucrose in PB for at least 4 hours and then immersed in 30% sucrose in PB for 12 hours, and resectioned at 60 μm on a freezing microtome. The sections were collected in PB and the endogenous peroxidase blocked by a 15-

minute immersion in 0.6% hydrogen peroxide in methanol. The tissue was washed several times in PB, and then incubated in the avidin-biotin complex solution (ABC *Elite* kit, Vector Labs) and the reaction product visualized with a heavy-metal intensified DAB protocol. Following several washes in PB, the 60 μm-thick sections were mounted on gelatin-coated slides, dried, dehydrated, and coverslipped. Sections were inspected for labeled neurons, and only data from cells that could unequivocally be classified according to published criteria [16, 17] were taken for further analysis. Cells were reconstructed at medium magnification (10x to 20x) with a camera lucida on a Leica microscope and projected onto the 2D plane.

4.6   Acknowledgments

References

[1] G. M. Shepherd, *The Synaptic Organization of the Brain* (Oxford Univ. Press, New York, 2003).

[2] J. Foss, A. Longtin, B. Mensour, and J. Milton, Phys. Rev. Lett. **76**, 708 (1996).

[3] J. Foss, F. Moss, and J. Milton, Phys. Rev. E **55**, 4536 (1997).

[4] J. Foss and J. Milton, J. Neurophysiol. **84**, 975 (2000).

[5] K. Gopalsamy, I. K. C. Leung, and P. Liu, Appl. Math. Comput. **94**, 171 (1998).

[6] S. Bernard, J. Belair, and M. C. Mackey, Discrete Cont. Dyn.-B **1**, 233 (2001).

[7] C. W. Eurich, M. C. Mackey, and H. Schwegler, J. Theor. Biol. **216**, 31 (2002).

[8] F. M. Atay, Phys. Rev. Lett. **91**, 094101 (2003).

[9] A. Thiel, H. Schwegler, and C. W. Eurich, Complexity **8**, 102 (2003).

[10] C. W. Eurich, A. Thiel, and L. Fahse, Phys. Rev. Lett. **94**, 158104 (2005).

[11] H. Luksch, Rev. Neuroscience **14**, 85 (2003).

[12] S.-R. Wang, Brain. Res. Rev. **41**, 13, (2003).

[13] E. Gruberg, E. Dudkin, Y. Wang, G. Marín, C. Salas, E. Sentis, J. Letelier, J. Mpodozis, J. Malpeli, H. Cui, R. Ma, D. Northmore, and S. Udin, J. Neurosci. **26**, 10368 (2006).

[14] K. A. Maczko, P. F. Knudsen, and E. I. Knudsen, J. Neurosci. **26**, 12799 (2006).

[15] G. Marín, C. Salas, E. Sentis, X. Rojas, J. C. Letelier, and J. Mpodozis, J. Neurosci. **27**, 8112 (2007).

[16] Y. Wang, D. E. Major, and H. J. Karten, J. Comp. Neurol. **469**, 275 (2004).

[17] Y. Wang, H. Luksch, N. C. Brecha, and H. J. Karten, J. Comp. Neurol. **494**, 7 (2006).

[18] G. Marín, J. Mpodozis, E. Sentis, T. Ossandón, and J. C. Letelier, J. Neurosci. **25**, 7081 (2005).

[19] C. M. Marcus and R. M. Westervelt, Phys. Rev. A **39**, 347 (1989).

[20] K. L. Babcock and R. M. Westervelt, Physica D **28**, 305 (1987).

[21] C. R. Laing and A. Longtin, Neural Comput. **15**, 2779 (2003).

[22] S. F. Brandt, A. Pelster, and R. Wessel, Phys. Rev. E **74**, 036201 (2006).

[23] S. F. Brandt, A. Pelster, and R. Wessel, Europhys. Lett. **79**, 38001 (2007).

[24] S. F. Brandt and R. Wessel, Biol. Cybern. **97**, 221 (2007).

[25] S. Ramón y Cajal, *Histologie du Système Nerveux de l'Homme et des Vertébrés* (Maloine, Paris, 1911).

[26] S. P. Hunt and H. Künzle, J. Comp. Neurol. **170**, 153 (1976).

[27] S. P. Hunt, P. Streit, H. Künzle, and M. Cuenod, Brain Res. **129**, 197 (1977).

[28] W. Woodson, A. Reiner, K. Anderson, and H. J. Karten, J. Comp. Neurol. **305**, 470 (1991).

[29] V. B. Domesick and D. K. Morest, Neuroscience **2**, 477 (1977).

[30] T. Sebestény, D. C. Davies, N. Zayats, A. Németh, and T. Tömböl, J. Anat. **200**, 169 (2002).

[31] T. Tömböl, G. Egedi, and A. Németh, J. Hirnforsch. **36**, 501 (1995).

[32] T. Tömböl and A. Németh, Cell Tissue Res. **291**, 255 (1998).

[33] O. Güntürkün and M. Remy, Neurosci. Lett. **111**, 18 (1990).

[34] B. Hellmann, M. Manns, and O. Güntürkün, J. Comp. Neurol. **436**, 153 (2001).

[35] J. J. Hopfield, Proc. Natl. Acad. Sci. U.S.A. **81**, 3088 (1984).

[36] J. Wei and S. Ruan, Physica D **130**, 255 (1999).

[37] K. P. Hoffman, J. Neurophysiol. **36**, 409 (1973).

[38] J. Mpodozis, J. C. Letelier, M. L. Concha, and H. Maturana Int. J. Neurosci. **81**, 123 (1995).

[39] D. P. Northmore and D. J. Oh, J. Physiol. **506**, 207 (1998).

[40] J. C. Letelier, J. Mpodozis, G. Marín, D. Morales, C. Rozas, C. Madrid, and M. Velasco, Eur. J. Neurosci. **12**, 47 (2000).

[41] C. E. Carr and M. Konishi, J. Neurosci. **10**, 3227 (1990).

[42] J. Milton, *Dynamics of Small Neural Populations* (Amer. Math. Soc., Providence, 1996).

[43] I. Fisher, R. Vicente, J. M. Buldú, M. Peil, C. R. Mirasso, M. C. Torrent, and J. García-Ojalvo, Phys. Rev. Lett. **97**, 123902 (2006).

[44] B. D. Coleman and G. H. Renninger, SIAM J. Appl. Math. **31**, 111 (1976).

[45] U. an der Heiden, J. Math. Biol. **8**, 345 (1979).

[46] Y. Braiman, J. F. Lindner, and W. L. Ditto, Nature **378**, 465 (1995)

[47] S. F. Brandt, B. K. Dellen, and R. Wessel, Phys. Rev. Lett. **96**, 034104 (2006).

[48] R. Chacón and P. J. Martínez, Phys. Rev. Lett. **98**, 224102 (2007).

[49] J. C. Dye and H. J. Karten, Vis. Neurosci. **13**, 747 (1996).

[50] H. Luksch, K. Cox, and H. J. Karten, J. Comp. Neurol. **396**, 399 (1998).

[51] H. Luksch, H. J. Karten, D. Kleinfeld, and R. Wessel, J. Neurosci. **21**, 6440 (2001).

[52] H. Luksch, R. Khanbabaie, and R. Wessel, Nat. Neurosci. **7**, 380 (2004).

[53] R. Khanbabaie, A. Mahani, and R. Wessel, J. Neurophysiol. **97**, 2802 (2007).

[54] A. S. Mahani, R. Khanbabaie, H. Luksch, and R. Wessel, Biol. Cybern. **94**, 276 (2006).

Chapter 5

Dynamics of neural feedback triads

We observe that a number of vertebrate neural feedback circuits follow a characteristic feedback triad topology. This topology consists of two delayed feedback loops with an asymmetric lateral connection between them. A model of the feedback triad has five connection strength parameters. We show that because of the asymmetric lateral connection between the two loops, the system dynamics depend upon two algebraic combinations of subsets of the five parameters. Thus qualitatively equivalent system dynamics can be observed with widely differing parameter settings. We also show that without the asymmetric lateral connection one of the algebraic combinations vanishes and the system effectively reduces to one delayed feedback loop. Our analysis thus highlights the significance of the asymmetric lateral connection in the feedback triad topology that appears to have evolved independently in vertebrate neural feedback circuits.

Biological neural networks are the result of billions of years of evolution, which works by random changes and the survival of organisms with advantageous network properties [1]. Therefore, the networks emerging from the evolutionary process are, to some degree, dependent on temporal sequences of chance and can be laden with detail that seem to require special description in every case. However, because of the enhanced survival of organisms with advantageous networks during the evolutionary process, in biological networks we expect to find characteristic sets of circuit elements that obey general design principles [2]. Here, we present and investigate one such de-
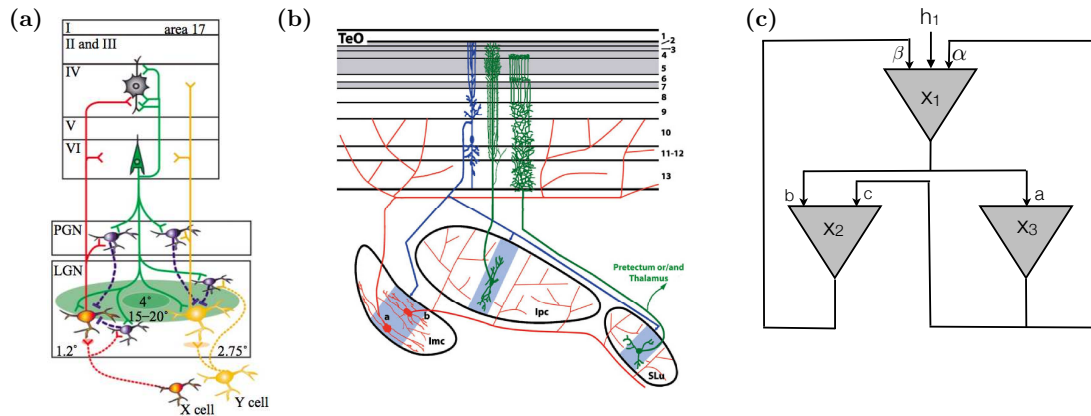
Figure 5.1: (Color) Feedback triad circuitry with asymmetrical lateral connections between the feedback loops. **(a)** Corticothalamic feedback triad of the cat features projections from the lateral geniculate nucleus (LGN) to both the perigeniculate nucleus (PGN) and visual cortex (V1), but receives topologically different feedback from these nuclei. **(b)** In the avian isthmotectal feedback triad, the optic tectum projects to both the Imc and Ipc nuclei of the isthmi, but like the cat receives topologically different feedback from those nuclei. **(c)** Model of feedback triad circuitry with asymmetry between the two feedback loops. Feed-forward synaptic connections are given by Latin graphemes and feedback connections are given by Greek graphemes.

sign principle, the neural feedback triad, which consists of two delayed feedback loops with an asymmetric lateral connection between them.

Feedback dominates neural networks of brains [3] and has been implicated in a number of signal processing tasks [4–9]. Here, we observe that two independently evolved feedback systems, the mammalian corticothalamic [Fig. 5.1(a)] [10] and the avian isthmotectal loops [Fig. 5.1(b)] [11, 12], follow a characteristic feedback triad topology [Fig. 5.1(c)]. This topology consists of two delayed feedback loops with an asymmetric lateral connection between them. In mammals, retinal ganglion cell axons project to the thalamic lateral geniculate nucleus (TH). The TH in turn projects to the thalamic reticular nucleus (RE) and the cortical layer 6 neurons (CX). Both, RE and CX, feed back to TH. The two feedback loops are different in their spatial extent. The CX feedback is broad, whereas the RE feedback is more local. In addition, the CX also projects to RE. In birds, retinal ganglion cell axons project to the optic tectum (TeO). The TeO in turn projects to the nucleus isthmi pars parvocellularis (Ipc) and to the nucleus isthmi pars magnocellularis (Imc). Both Ipc and Imc feed back to the TeO. The two feedback loops are different in their spatial extent. The Imc feedback is broad, whereas the Ipc feedback is more local. In addition, the Imc also projects to Ipc. In summary, the two independently evolved feedback systems, the mammalian corticothalamic and

the avian isthmotectal system, converged onto the same feedback triad topology [Fig. 5.1(c)] that consists of a global and a local feedback loop with a lateral connection from the global to the local loop.

In this study, we present a point model using finite difference equations that take into account both the synaptic weights and the synaptic and transmission delays among the components of the isthmic circuitry. We show that the parameter space of synaptic weights in the nucleus isthmi circuitry has regions with robustness towards parameter changes and regions that are extremely sensitive to parameter changes. First, we develop a set of finite difference equations and show that under certain synaptic weight conditions the output firing rate of the system does not depend upon the individual synaptic weights but upon combinations of them. Next, we examine the tectal output dynamics as a function of the effective weight parameters and finally, we derive a stability condition that confines the stable nonzero fixed points to a region within the parameter space and show that the tectal output converges to the fixed points geometrically.

To model the nucleus isthmi feedback loop we consider three neurons with synaptic connections that reflect the topology established by anatomical studies of the avian isthmotectal circuit [11, 12] [see Fig. 5.1(c)]. To investigate the dynamics of the circuitry we use a nonlinear finite difference map that outputs a graded potential at discrete time steps. The use of finite difference equations leads to a tractable computational model that has been used to study nonlinear microcircuits in electrical engineering [13].

Spatial separation between the different neurons in the circuit results in a signal transmission delay. As a simplification we consider the case in which all delays in the circuit are equal. This delay τ along with the corresponding synaptic weights gives the following set of nonlinear discrete equations

$$x_i(t) = \delta \left[\sum_{j=1}^{3} w_{ij} x_j(t - \tau) + h_i \right],$$ (5.1)

where x_1, x_2 and x_3 are the firing rates of the tectal, Ipc, and Imc neurons, respectively, and δ denotes an input-output transfer function. The synaptic weights w_{ij} and the external input h_i are

given as

$$
w = \begin{pmatrix} 0 & \alpha & \beta \\ b & 0 & c \\ a & 0 & 0 \end{pmatrix}, \qquad \boldsymbol{h} = \begin{pmatrix} h_1 \\ 0 \\ 0 \end{pmatrix}. \tag{5.2}
$$

For the transfer function δ, we make the choice $\delta(s) = \max(s, 0)$. This nonlinear activation function immediately imposes certain constraints on the synaptic weights if the output is to be nontrivial. For the circuit to function as a three-neuron circuit, the synaptic connection onto the Imc neuron must be positive, $a > 0$. In addition, experimental evidence suggests that the synaptic polarity of the connections b and c are similarly positive [14]. With these synaptic constraints the model can be reduced from a 5 dimensional weight parameter space to a two dimensional weight parameter space. The tectal output firing rate, x_1, in terms of previous tectal firing rates is given as

$$
x_1(t) = \delta \left[h_1(t - \tau) + \eta x_1(t - 2\tau) + \xi x_1(t - 3\tau) \right], \tag{5.3}
$$

where the constants η and ξ are the following combinations of the synaptic weights,

$$
\eta = \beta b + \alpha a, \qquad \xi = \beta a c. \tag{5.4}
$$

With a constant external input, $h_1(t) = h_1$, the activity of the tectal neurons given by 5.3 displays a rich variety of firing rate patterns. At different values of the synaptic weights the tectal neurons' firing rate can converge, diverge, oscillate, or exhibit aperiodicity. This type of microcircuit is similar to central pattern generator (CPG) circuits. Central pattern generators are small microcircuits capable of producing rhythmic outputs without rhythmic sensory inputs [15, 16]. They are common in motor systems [17] and have many similarities to circuits found in the brain [18–20]. The activity states of these circuits can be changed by sensory afferents and neuromodulators making the circuit multifunctional and dynamically plastic [21]. To investigate how changes in the synaptic weights by neuromodulators could alter the state of the isthmotectal circuit, we numerically simulated firing rate trajectories for various combinations of the synaptic weights and observed whether the trajectory converged, diverged or oscillated. The parameter space shown in Fig. 5.2 displays the tectal
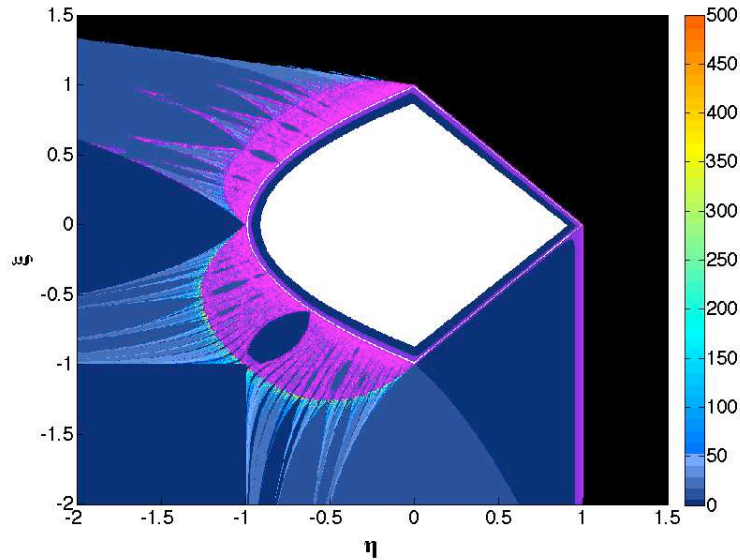
Figure 5.2: (Color) Different forms of dynamics in the feedback triad as a function of the connections strengths. The effective parameter space in η and ξ is shown, and the dynamics that result for the corresponding combinations of coupling strengths are color coded. The delay τ is one time unit, and trajectories were evaluated for 500 time units. The white region corresponds to convergent trajectories, whereas the black region corresponds to diverging trajectories. The cyan region corresponds to aperiodic time traces as shown in Fig. 5.3. All of the other regions in the colormap are oscillatory trajectories with periods as indicated by the colorbar.

neuron firing rate behavior as a function of the effective weight parameters η and ξ, incremented in steps of .001 units. The simulation was run for 500 time steps with the exception of the purple region, in which it was run for 15,000 time steps. The white region corresponds to parameter combinations that lead to stable fixed points for tectal firing rates. The shades of color between 0 and 500 in the color-map indicate periodic firing rates with the color representing the period of oscillation. In addition, oscillatory behavior that occurs after a significant transitory period of up to 15,000 time steps is colored in purple. The black region represent diverging firing rate patterns. The remaining pink region consist of aperiodic trajectories that exhibit irregular oscillations. To determine if these irregular oscillations were actually regular but on a very long time scale we computed the Fourier transform of these time series and found that the oscillations are indeed irregular. Next, we considered whether these aperiodic trajectories could be chaotic. Since chaotic trajectories would be exponentially sensitive to initial conditions, we numerically simulated the trajectories at five different initial conditions. Figure 5.3 shows that the aperiodic trajectories are not chaotic but exhibit
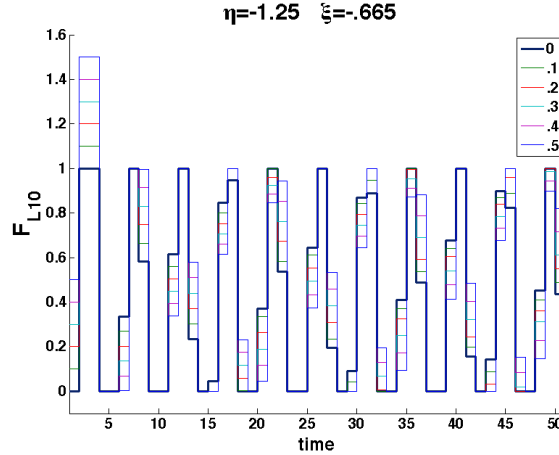
Figure 5.3: (Color) Aperiodic time traces for different initial conditions. Small perturbations from the zero initial condition do not diverge away as would be expected for a chaotic system. The system exhibits multi-stability as changing the initial conditions brings the system to a neighboring attractor.

different firing rate trajectories based on the initial conditions. This switch to a different attractor based on the initial conditions is called multi-stability [22] and is commonly found in CPG circuits.

By examining the weight parameter space, it is immediately apparent that certain regions have highly stable network activity since shifts in the weights as may be induced by neuromodulators, do not lead to changes in the activity state of the circuit. However, other regions show dynamic shifts in network activity with very small changes to the effective weights η and ξ. This dynamic shifting could allow the circuit to transform its activity state making the circuit dynamically plastic.

The nonlinearity of the finite difference equations lends a complicated structure to the parameter space. In particular, the rectifying transfer function allows for inhibitory networks to oscillate given a positive external input stimulus. For oscillations of low period, a table listing the firing rate shows how the periodic trajectories are influenced by the rectification. For example in the region $\eta < -1$ and $\xi < -1$, a table of the firing rates given by 5.3 shows immediate periodicity (cf. Tab. 5.1),

Time	1	2	3	4	5	6	7	8	9	10	11
h_1	1	1	1	1	1	1	1	1	1	1	1
x_1	0	1	1	1	0	0	0	1	1	1	0

Table 5.1: Cyclic behavior in the feedback triad. The firing rate x_1 that results for coupling strengths $\eta < -1$ and $\xi < -1$ is shown for the first eleven time units. The cyclic behavior of x_1 is caused by the by the rectification of the firing rates.

however tabling of higher period oscillations becomes intractable.

The fixed points of the system, shown as white in the parameter space, are determined by (5.3). Since only positive fixed points are considered we can neglect the transfer function δ and obtain the following fixed points.

$$x_1^* = \frac{1}{1 - \eta - \xi}. \tag{5.5}$$

The line $\eta + \xi = 1$ bounds the region where stable fixed points exist. In addition, unstable fixed points above this line diverge monotonically whereas unstable fixed points below this line diverge non-monotonically as a result of the input-output transfer function δ. In addition, the convergent trajectories converge to the fixed points geometrically. This geometrical convergence can be seen in the time traces or by looking at the table values of the firing rates. Thus, the fixed points given in (7) represent the sum of the geometric series for $|\eta + \xi| < 1$

$$\sum_{n=1}^{\infty} (\eta + \xi)^n. \tag{5.6}$$

The convergence of the firing rates to a fixed point has interesting applications to the three-neuron system with an asymmetrical lateral connection between the feedback loops. If the lateral connection in this three neuron model were not present, then the weight parameter ξ would vanish. Along the line $\xi = 0$ in the parameter space many values of the remaining weight parameter η lead to converging firing rates, which is inconsistent with experiments that show oscillatory activity in the tectum [23]. Thus, the asymmetrical lateral connection is crucial for oscillatory behavior of the units within the three-neuron circuit.

The delayed three-neuron feedback circuit with an asymmetrical lateral connection between the feedback loops is common in vertebrate neural circuits. Using constraints of the synaptic strengths observed in the avian feedback triad circuit, we have shown that the five strength connection parameters can be reduced to two effective strength parameters. With this result, the parameter space over the two free synaptic strength parameters exhibits steady, diverging, aperiodic, and oscillating activity states. We have observed that the aperiodic states are not chaotic but rather exhibit multi-stability. In addition, a fixed point analysis has shown that the convergent activity states are confined by a stability condition and that the convergent trajectories converge geometrically to the fixed point.

When the lateral connection between the two elements of the feedback loop is not present, one of the effective parameters vanishes and geometrical convergence to a fixed point occurs for many choices of the synaptic strengths. In addition, the parameter space exhibits regions where qualitatively equivalent system dynamics occurs for widely differing synaptic strength parameters and regions in which small changes in synaptic strength lead to drastically different network activity. In mammals the TH has feed-forward connections to both the CX and the RE. The CX and the RE are connected via an asymmetrical lateral connection with the CX and the RE providing feedback to the TH. The feedback triad model presented here highlights the importance of the asymmetrical connection from the CX to the RE in terms of generating oscillatory behavior in the TH neurons.

References

[1] D. J. Futuyama, *Evolution* (Sinauer, Sunderland, 2005).

[2] U. Alon, *An Introduction to Systems Biology: Design Principles of Biological Circuits* (Chapman & Hall, New York, 2007).

[3] G. M. Shepherd, *The Synaptic Organization of the Brain* (Oxford Univ. Press, New York, 2003).

[4] P. S. Churchland, V. S. Ramachandran, and T. J. Sejnowski, in *Large-Scale Neuronal Theories of the Brain*, edited by C. Koch and J. L. Davis (MIT Press, Cambridge, 1994).

[5] D. Mumford, in *Large-Scale Neuronal Theories of the Brain*, edited by C. Koch and J. L. Davis (MIT Press, Cambridge, 1994).

[6] S. Ullman, in *Large-Scale Neuronal Theories of the Brain*, edited by C. Koch and J. L. Davis (MIT Press, Cambridge, 1994).

[7] D. C. van Essen, C. H. Anderson, and B. A. Olshausen, in *Large-Scale Neuronal Theories of the Brain*, edited by C. Koch and J. L. Davis (MIT Press, Cambridge, 1994).

[8] F. Crick and C. Koch, Nature **391**, 245 (1998).

[9] N. A. B. Yousif and M. Denham, Eur. J. of Neurosci. **22**, 3179 (2005).

[10] A. M. Sillito, J. Cudeiro, and H. E. Jones, Trends Neurosci. **29**, 307 (2006).

[11] Y. Wang, D. E. Major, and H. J. Karten, J. Comp. Neurol. **469**, 275 (2004).

[12] Y. Wang, H. Luksch, N. C. Brecha, and H. J. Karten, J. Comp. Neurol. **494**, 7 (2006).

[13] S. Deutsch, *Understanding the Nervous System: An Engineering Perspective* (IEEE Press, New York, 1993).

[14] J. Shao and R. Wessel (unpublished).

[15] E. Marder and R. L. Calabrese, Physiol. Rev. **76**, 687 (1996).

[16] S. G. Stein, S. Grillner, A. I. Selverston, and G. S. Douglas (Eds.), *Neurons, Networks, and Motor Behavior* (MIT Press, Cambridge, 1997).

[17] M. I. Rabinovich, P. Varona, A. I. Selverston, and H. D. I. Abarbanel, Rev. Mod. Phys. **78** (2006).

[18] S. Grillner, H. Markram, E. D. Schutter, G. Silberberg, and F. E. LeBeau, Trends Neurosci. **28**, 525 (2005).

[19] M. Solis and D. Perkel, J. Neurosci. **25**, 2811 (2005).

[20] R. Yuste, J. N. MacLean, J. Smith, and A. Lansner, Nat. Rev. Neurosci. **6**, 477 (2005).

[21] P. Goldman-Rakic, Neuron **14**, 477 (1995).

[22] J. Foss and J. Milton, J. Neurophysiol. **84**, 975 (2000).

[23] G. Marín, J. Mpodozis, E. Sentis, T. Ossandón, and J. C. Letelier, J. Neurosci. **25**, 7081 (2005).

Chapter 6

Winner-take-all selection in a neural system with delayed feedback

We consider the effects of temporal delay in a neural feedback system with excitation and inhibition. The topology of our model system reflects the anatomy of the avian isthmic circuitry, a feedback structure found in all classes of vertebrates. We show that the system is capable of performing a 'winner-take-all' selection rule for certain combinations of excitatory and inhibitory feedback. In particular, we show that when the time delays are sufficiently large a system with local inhibition and global excitation can function as a 'winner-take-all' network and exhibit oscillatory dynamics. We demonstrate how the origin of the oscillations can be attributed to the finite delays through a linear stability analysis.

6.1   Introduction

In order to identify and react to behaviorally relevant objects in their visual environment, animals must be able to rapidly locate the positions of these objects in visual space. This ability to select and orient towards the most salient part in a visual scene that may be cluttered with other, for the animal's survival less relevant objects, has evolutionary significance, as it permits the organism to detect quickly possible prey, predators, and mates [1]. In standard models of selective visual attention, the stimulus is encoded in a 'saliency map' that topographically represents the conspicuity

of the stimulus over the visual scene. The most salient location is then chosen by a 'winner-take-all' (WTA) network, i.e., by a neurally implemented maximum detector [2]. In neuronal network models, these WTA networks are often realized as networks with lateral inhibition [3–5], global inhibition [6], or local excitation and long distance inhibition [7]. After the most active location, i.e., the 'winner', in the saliency map has been chosen, attention should not, however, continue to be focused onto it. One way of allowing attention to shift, is to transiently inhibit neurons in the saliency map that correspond to the currently attended location, a strategy known as 'inhibition of return' [8].

The homolog of the mammalian superior colliculus in non-mammalian vertebrates is the optic tectum (TeO). It is critically involved in localizing visual objects and in the preparation of orienting responses towards these objects [9, 10]. In all classes of vertebrates, the TeO is reciprocally connected with the nucleus isthmi (NI), which is homologous to the parabigeminal nucleus in mammals [11]. In the avian visual pathway, the NI consists of three subnuclei: the nucleus pars parvocellularis (Ipc), the nucleus pars magnocellularis (Imc), and the nucleus pars semilunaris (SLu) [12, 13]. In both Ipc and Imc the projection from the tectum is topographically organized such that the retinotopic map is preserved in both nuclei, with the projection to the Imc being somewhat coarser than for the Ipc [12]. In contrast, the isthmic projections back to the TeO are very different for Ipc and Imc. Ipc neurons project back to the TeO in a highly precise homotopic manner, i.e., the axons of each Ipc neuron terminate in that part of the optic tectum from which their visual inputs come [13]. Imc, on the other hand, has two populations of neurons, which both make heterotopic projections but only to the TeO or Ipc, respectively [12]. The three-nuclei circuitry consisting of TeO, Ipc, and Imc is shown in Fig. 6.1 [14]. Due to latencies arising from synaptic process and the spatial separation of the nuclei, the coupling between TeO and NI cannot be considered instantaneous. Rather, finite temporal delays exist [12, 13]. Furthermore, delays can arise from the dynamical properties of the systems involved. For instance, the authors of Ref. [15] report stimulus-dependent onset latency of recurrent inhibition in the cat hippocampus, and these findings were later explained in Ref. [16]. It has been known for some time that temporal delays can cause an otherwise stable system to oscillate [17–19] and may lead to bifurcation scenarios resulting in chaotic dynamics [20, 21]. Therefore, finite delays are an essential property of any realistic model of a neuron population [22].

The synaptic effect of the recurrent projections from the Ipc and Imc cells onto their target cells
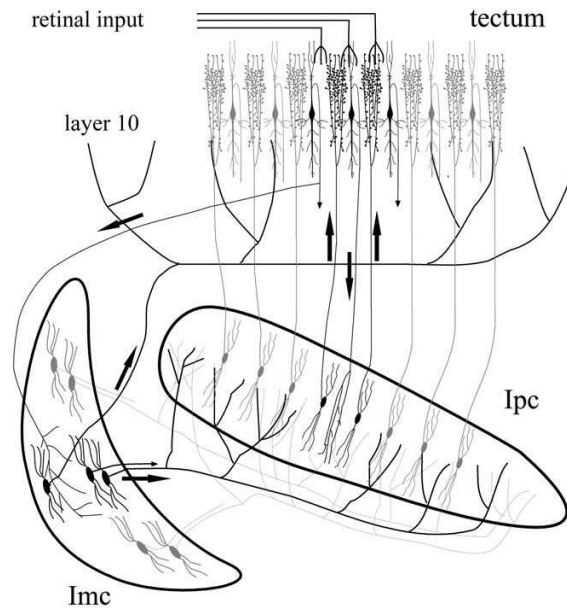
Figure 6.1: Diagram of the isthmotectal feedback loop. The Ipc is reciprocally connected with the TeO in a precise homotopic manner. Tectal neurons project topographically to the Ipc, and Ipc neurons project back to the corresponding tectal loci. Imc receives a coarser topographic projection and projects back to the TeO and Ipc via widely ramifying terminal fields. Black represents visually activated neural elements. Reprinted with permission from Ref. [14].

is less well understood than their anatomical organization. The available evidence suggests that Ipc neurons are cholinergic, whereas Imc neurons have been shown to express gamma-aminobutyric acid (GABA) as their main neurotransmitter. Thus, according to the usual role of acetylcholine and GABA, one might speculate that Ipc and Imc neurons mediate excitation and inhibition onto their target cells, respectively. The authors of Ref. [14] posit that "the three-nuclei circuitry [...] may constitute a winner-take-all network [2] in which local visual inputs to the Ipc are augmented by the re-entrant loop among tectal and Ipc neurons, combined with broad inhibition of the rest of the Ipc by Imc neurons." This argument seems immediately plausible, however, electrophysiological experiments [23–25] suggest that the synaptic effects of Ipc and Imc are actually converse to this scenario and that the Ipc mediates inhibition whereas the Imc has an excitatory effect. Given the anatomical organization of the recurrent projections from Ipc and Imc, it is not fully intuitive how the system could function as a WTA network when Imc is excitatory and Ipc inhibitory. Nevertheless, the author of Ref. [26] considers this possibility: "The positive and negative feedback loops formed between the tectum and NI may work together in a winner-take-all network, so that the positive feedback loop could provide a powerful augmentation of activated loci, while the negative feedback

optic tectum	nucleus isthmi pars parvocellularis	nucleus isthmi pars magnocellularis
TeO	Ipc	Imc
α	β	γ
$1 \ldots N$	$N + 1 \ldots 2N$	$2N + 1$

Table 6.1: Components of the isthmotectal feedback loops and abbreviations. We use the Greek indices α, β, and γ to denote TeO, Ipc, and Imc, respectively. Furthermore, neurons are numbered such that indices 1 through N refer to the TeO, $N + 1$ through $2N$ refer to the Ipc, and the index $2N + 1$ refers to the Imc.

loop may strongly suppress the others [...]. For example, Imc could enhance the visual responses of tectal cells to target locations or stimulus features, while Ipc may suppress those to other locations or features in the visual field." The aim of this work is to investigate possible mechanisms for WTA selection in the isthmotectal feedback loop through a computational model. In this context, we do not refer to the term WTA in its most strict sense, which would imply that only the neuron with the strongest input exhibits a nonzero firing rate; rather, we speak of WTA behavior when the firing rates of neurons with weaker inputs are suppressed relative to those with stronger input.

In Sect. 6.2, we introduce our model of the isthmic system, and we analyze its response dynamics for different temporal delays and different combinations of excitation and inhibition in Sect. 6.3. In Sect. 6.4, we compare the efficiency of WTA selection for these combinations. In Sect. 6.5, we employ a linear stability analysis to show how the oscillatory dynamics that arise in the system can be attributed to the increasing delays. In Sect. 6.6, we summarize our results.

6.2   Model

To explore the conjecture that the isthmotectal feedback loop functions as a WTA network, we consider a model system of coupled Hopfield neurons with temporal delays [27, 28], as described in Ref. [29]. In this model, the temporal evolution of the membrane potential of the ith neuron (taken from rest potential), $V_i(t)$, is given by the first-order delay differential equation (DDE)

$$\tau_i^{(\mathrm{m})} \frac{dV_i(t)}{dt} = -V_i(t) + \sum_j w_{ij} r_j(t - \tau_{ij}) + I_i(t) \,. \tag{6.1}$$
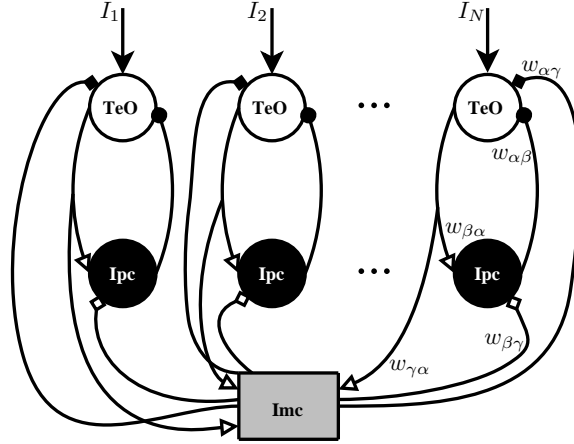
Figure 6.2: Diagrammatic representation of our model for the isthmotectal feedback loop. Neurons in the TeO and Ipc, which project topographically, are modeled as individual units. Due to their diffuse projections, Imc neurons are combined to form a feedback kernel.

Here, the membrane time constant for the ith neuron is denoted by $\tau_i^{(\mathrm{m})}$, the synaptic connection weights for the projection from the jth to the ith neuron are w_{ij}, the temporal delay for this projection is τ_{ij}, r_j is the firing rate for the jth neuron and is linked to its voltage according to a nonlinear firing rate function,

$$r_j = S_j(V_j)\,, \tag{6.2}$$

and $I_i(t)$ denotes an external input to the ith neuron. To model the isthmic system, we assume that N tectal neurons are reciprocally coupled to N Ipc neurons and that the only neurons that receive external input are those in the TeO. Furthermore, due to the broad and heterotopic nature of the projections from Imc, we combine the Imc neurons to a feedback kernel, which then projects globally to both TeO and Ipc. The topological structure of our model is depicted in Fig. 6.2. To simplify our model, we make the following assumptions: The synaptic weights for the projections TeO→Ipc, TeO→Imc, Ipc→TeO, Imc→TeO, Imc→Ipc, are the same for all neurons in each of these groups, and we denote them by $w_{\beta\alpha}$, $w_{\gamma\alpha}$, $w_{\alpha\beta}$, $w_{\alpha\gamma}$, $w_{\beta\gamma}$, respectively; all membrane time constants are identical, $\tau_i^{(\mathrm{m})} = \tau^{(\mathrm{m})}$ for all i, and we rescale time such that $\tau^{(\mathrm{m})} = 1$; all delays are identical, $\tau_{ij} = \tau$; all firing rate functions are identical $S_j(V_j) = S(V_j)$. Furthermore, we number our neurons such that the indices $i = 1, 2, \ldots, N$ refer to tectal neurons, the indices $i = N+1, N+2, \ldots, 2N$ refer to Ipc neurons, and the index $i = 2N+1$ refers to the Imc kernel

(cf. Tab. 6.1). Then, the dynamics of our system are described by the $2N+1$ DDEs:

$$
\begin{aligned}
\frac{dV_i(t)}{dt} &= -V_i(t) + w_{\alpha\beta}r_{i+N}(t-\tau) + w_{\alpha\gamma}r_{2N+1}(t-\tau) + I_i(t), \quad i = 1, 2, \cdots, N, \\
\frac{dV_i(t)}{dt} &= -V_i(t) + w_{\beta\alpha}r_{i-N}(t-\tau) + w_{\beta\gamma}r_{2N+1}(t-\tau), \quad i = N+1, N+2, \ldots, 2N, \\
\frac{dV_{2N+1}(t)}{dt} &= -V_{2N+1}(t) + w_{\gamma\alpha}\sum_{i=1}^{N} r_i(t-\tau).
\end{aligned}
\tag{6.3}
$$

For the firing rate function we choose the piecewise linear function,

$$
r_j = S(V_j) = \begin{cases}
0 & \text{for } V_j < V_T, \\
a(V_j - V_T) & \text{for } V_T \leq V_j \leq V_T + S_{\max}/a, \\
S_{\max} & \text{for } S_{\max}/a + V_T < V_j.
\end{cases}
\tag{6.4}
$$

Finally, we make the simplifying assumptions $|w_{\beta\alpha}| = N|w_{\gamma\alpha}| = |w_{\alpha\beta}| = |w_{\alpha\gamma}| = |w_{\beta\gamma}| = 1/a$ and $V_T = 0$. The signs of the synaptic weights determine whether a projection is excitatory or inhibitory and since the tectal cells mediate excitation, we have $w_{\beta\alpha}, w_{\gamma\alpha} > 0$. The authors of both Ref. [14] and Ref. [26] both discuss scenarios in which WTA behavior arises from an interplay of excitation and inhibition in the isthmotectal feedback loop, and we are therefore interested in the cases where Ipc and Imc have adversary effects onto the TeO. Thus, four cases remain to be studied, which can be characterized according to the signs of $(w_{\alpha\beta}, w_{\alpha\gamma}, w_{\beta\gamma})$ as $(+, -, -)$, $(+, -, +)$, $(-, +, +)$, and $(-, +, -)$. In our model, the first two of these cases correspond to global inhibition and local excitation of tectal cells through feedback, whereas the latter two correspond to global excitation and local inhibition of the cells in the TeO.

6.3 Response dynamics

In the following, we investigate the dynamical response behavior of a network consisting of $N = 200$ (initially quiescent) neurons to a static stimulus. We choose an input consisting of five superimposed Gaussians with peaks at $i = 20, 60, 100, 140,$ and 180, and peak values of $0.75, 0.5, 0.45,$ $0.4,$ and 0.35, respectively. The (normalized) stimulus is shown, e.g., in Fig. 6.3(a). In particular, we are interested in the firing rates of those neurons whose positions coincide with the peaks in the
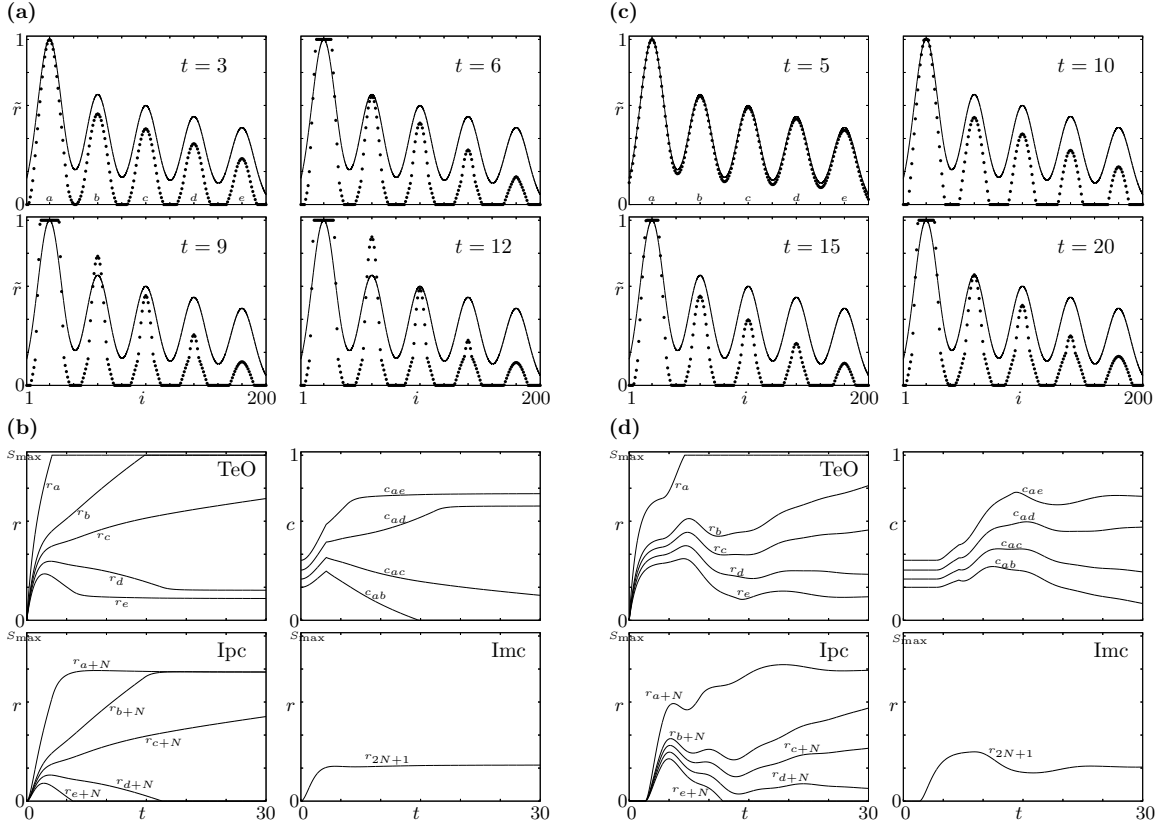
Figure 6.3: WTA behavior and network dynamics for the case $(+, -, -)$, i.e., global inhibition and local excitation. **(a)** and **(b)** are for the undelayed case, $\tau = 0$, while in **(c)** and **(d)** the delay is $\tau = 2$. The dots in the snapshots in **(a)** and **(c)** show the normalized response of tectal cells, i.e., the quantity $\tilde{r}_i = r_i(t)/r_{\max}(t)$, where $r_{\max}(t)$ denotes the maximum of all tectal firing rates at time t, while the solid line shows the normalized input, i.e., the quantity $I_i/I_{\max}$. In both **(b)** and **(d)**, the first plot shows the firing rate dynamics of the neurons a through e in the TeO, the second plot depicts the temporal evolution of the response contrast of tectal neurons b through e when compared with neuron a, the third plot shows the activity of the Ipc neurons receiving input from the tectal neurons a through e, and the fourth plot shows the firing rate of the Imc.

stimulus, and in order to abbreviate our notation we denote their indices as a, b, c, d, and e according to descending strength of their respective inputs.

6.3.1   Global inhibition, local excitation

We first consider the cases $(+, -, -)$ and $(+, -, +)$. In this situation, our network is similar to the circuit considered in Ref. [6]. Therefore, we expect that it can perform a reasonably accurate WTA selection. Figure 6.3 shows the firing rate dynamics in response to the static input. The undelayed case is shown in Figs. 6.3(a) and (b), whereas Figs. 6.3(c) and (d) show the dynamics that result

when $\tau = 2$. To compare differences between firing rates of tectal neurons we consider the contrast measure

$$c_{ij} = \frac{|r_i - r_j|}{r_i + r_j} \,.\tag{6.5}$$

In particular, we are interested in the contrasts c_{ab}, c_{ac}, c_{ad}, and c_{ae}, whose temporal dynamics are depicted in the second plots of Figs. 6.3(b) and (d). From Fig. 6.3 we see that in the case $(+, -, -)$ the weakest inputs are suppressed efficiently, while the neurons receiving the strongest input are driven towards maximum firing. Inputs of intermediate strength (e.g., the one received by neuron b) are not suppressed. Thus, in the configuration $(+, -, -)$ the system can perform a WTA selection, but not with very good 'resolution'. Furthermore, by comparing Figs. 6.3(a) and (b) with Figs. 6.3(c) and (d), we see that the temporal delay in the system has only little effect on its efficiency as a WTA selector. The main effect of the delay is that it causes the system to evolve on a longer time scale, i.e., the steady state is not reached as fast as in the undelayed case.

For the case $(+, -, +)$ it turns out that the inhibition in the system is insufficient to compensate for the positive feedback in the recurrent coupling between TeO and Ipc, and even neurons that receive only weak inputs are driven towards maximum firing. Thus, in the configuration $(+, -, +)$ our model system does not function as a WTA network.

6.3.2 Global excitation, local inhibition

Now we consider the cases $(-, +, +)$ and $(-, +, -)$, which correspond to global excitation of the TeO through the Imc and local inhibition from the Ipc. They thus correspond to the scenario described in Ref. [26] and it does not seem immediately intuitive how WTA behavior could result in this configuration. Indeed, for the case $(-, +, +)$, when there are no delays no WTA selection occurs. The response dynamics for this case are shown in Figs. 6.4(a) and (b). The contrast in the firing rate response of neurons receiving inputs of different strengths is nearly identical to the contrast of the respective inputs during all phases of the system's temporal evolution. Thus, neither are weaker inputs suppressed nor are stronger inputs augmented. When we introduce delay into the system, however, its behavior changes drastically. Figs. 6.4(c) and (d) show the response dynamics for the case $\tau = 2$. Note that the neurons' firing rates, as well as the contrasts between responses now
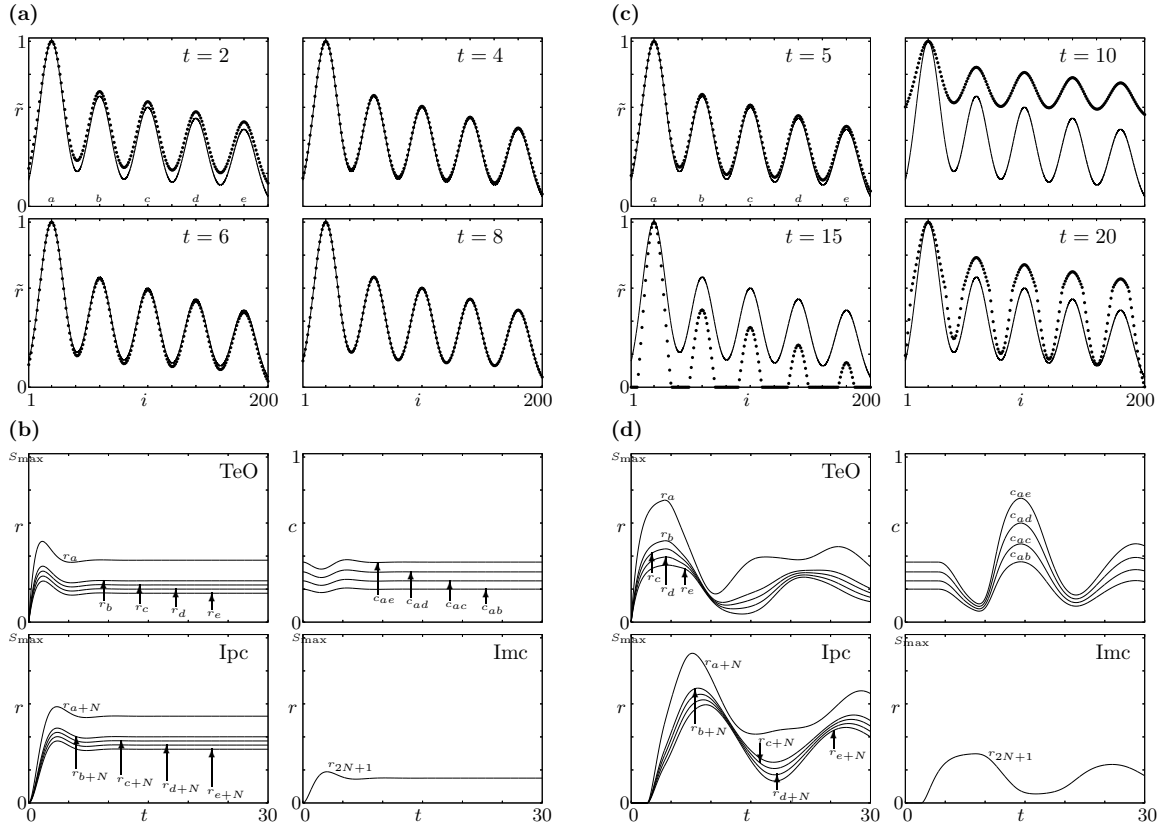
Figure 6.4: WTA behavior and network dynamics for the case $(-, +, +)$, i.e., global excitation and local inhibition. Same as Fig. 6.3, but for inverted signs of $w_{\alpha\beta}$, $w_{\alpha\gamma}$, and $w_{\beta\gamma}$.

exhibit oscillatory behavior. The system can perform a WTA selection with reasonable accuracy, but only transiently, i.e., only during certain phases of its temporal evolution. As a matter of fact, a phase of best WTA selectivity is preceded and followed by phases where the response contrast is even lower than that of the input.

Since standard models of selective attention usually require that the most salient stimulus not be a permanent 'winner', but rather that it be suppressed once attention has been directed to it, the dynamical evolution of the response is an important characteristic. Consequently, it may actually be a desirable feature of a WTA network to only determine the 'winner' transiently.

The case $(-, +, -)$ leads to similar results as in the case $(+, -, +)$. When Ipc neurons are inhibited by the Imc, they cannot provide sufficient negative feedback to the TeO in order to prevent tectal neurons from being saturated through the positive feedback between TeO and Imc. Thus, in the configuration $(-, +, -)$ our model system does not function as a WTA network.
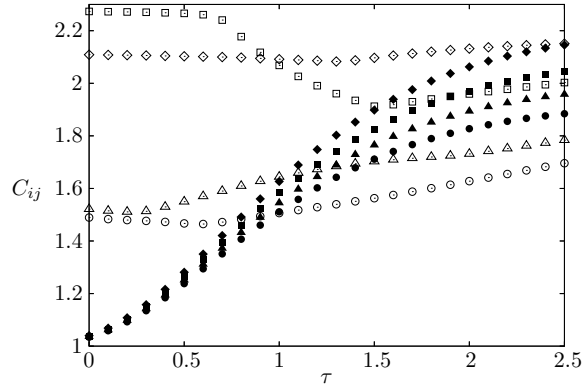
Figure 6.5: Performance of the model system as a WTA network. The maximal response contrast normalized to the input contrast is shown as a function of the delay τ. Open symbols are for the case $(+, -, -)$, and filled symbols are for the case $(-, +, +)$. The contrast C_{ij} is shown for $i = a$ and $j = b$ (circles), $j = c$ (triangles), $j = d$ (squares), and $j = e$ (diamonds).

6.4   Comparison of WTA selectivity

In order to quantify the performance of our model system as a WTA network, we consider the maximum in the response contrast between neurons i and j, normalized to the contrast between the (constant) input I to neurons i and j during the first 30 membrane time constants of the system's temporal evolution:

$$C_{ij} = \frac{I_i + I_j}{|I_i - I_j|} \max_{0 \leq t \leq 30} c_{ij} \,. \tag{6.6}$$

This quantity is shown for the pairs (a, b), (a, c), (a, d), and (a, e) for the cases $(+, -, -)$ and $(-, +, +)$ and for different values of the time delay in Fig. 6.5. As we expect from the results presented in Sec. 6.3, in the case of global inhibition and local excitation, $(+, -, -)$, the system's performance as a WTA network, measured by the value of C_{ij} depends only little on the time delay. Furthermore, we see that the system is efficient in suppressing weak inputs, whereas the response contrast for inputs of intermediate strength is less enhanced. The performance for the case $(-, +, +)$, on the other hand, depends strongly on the temporal delay. Furthermore, the ratio between the maximal response contrast and the input contrast is comparable for weak and intermediate inputs. When the delay is sufficiently large, the model system thus exhibits a better WTA 'resolution' in the case of global excitation and local inhibition than for the inverse scenario, albeit only transiently.

83

We have also investigated the role of parametric disorder in the system and find that it does not change our results qualitatively. For instance, when the projection latencies are drawn randomly from a normal distribution with mean at $\tau = 2$ and standard deviation of 0.2 and the synaptic weights are disordered using normal distributions with means at the default values and standard deviations of 10% of these values, the maximum contrast as measured by C_{ij} is comparable to the case without disorder. Simulating ten different samplings of randomized delays and synaptic weights for the case $(-, +, +)$, we obtain the result $(C_{ab}, C_{ac}, C_{ad}, C_{ae}) = (2.28 \pm 0.25,\ 2.50 \pm 0.30,\ 2.06 \pm 0.13,\ 2.34 \pm 0.12)$ (results are mean $\pm$ standard error of the mean), which is to be compared with the values for the undisordered case $(C_{ab}, C_{ac}, C_{ad}, C_{ae}) = (1.83,\ 1.89,\ 2.00,\ 2.06)$.

6.5   Linear Stability Analysis

We now aim to understand the origin of the delay-induced oscillatory dynamics in the case of global excitation and local inhibition through a stability analysis of the model system. To this end, we make the following ansatz, which, a posteriori, turns out to be correct. We assume that for the chosen input the system of DDEs (6.3) possesses a stationary point $V_i(t) = \bar{V}_i$ with $0 \leq \bar{V}_i \leq S_{\max}/a$ for $1 \leq i \leq 2N + 1$, and we can thus replace the voltages in the system (6.3) according to the linear part of the firing rate function S. The stationary point is then obtained by solving the equation

$$\bar{\mathbf{V}} = aW\bar{\mathbf{V}} + \mathbf{I}. \tag{6.7}$$

Here, $\bar{\mathbf{V}}$ and $\mathbf{I}$ are $2N + 1$ column vectors (only the first N entries of $\mathbf{I}$ are nonvanishing) and W is a $(2N + 1) \times (2N + 1)$ matrix of the form

$$W = \begin{pmatrix} \mathbf{0}_{N \times N} & w_{\alpha\beta}\mathbb{1}_{N \times N} & w_{\alpha\gamma}\mathbb{1}_{N \times 1} \\ w_{\beta\alpha}\mathbb{1}_{N \times N} & \mathbf{0}_{N \times N} & w_{\beta\gamma}\mathbb{1}_{N \times 1} \\ w_{\gamma\alpha}\mathbb{1}_{1 \times N} & \mathbf{0}_{1 \times N} & 0 \end{pmatrix}. \tag{6.8}$$

We find that for the case $(-, +, +)$, the matrix $\mathbb{1} - aW$ is invertible and that the solution for the stationary point $\bar{\mathbf{V}} = (\mathbb{1} - aW)^{-1}\mathbf{I}$ does indeed permit us to linearize the system (6.3). In the case $(+,-,-)$, however, it turns out that this solution yields values that lie outside of the linear regime

of the firing rate function, and the linearization (6.7) is therefore not valid. Next, we analyze the stability of the stationary point for the case $(-, +, +)$ by making the ansatz $\mathbf{V}(t) = \bar{\mathbf{V}} + \mathbf{c}e^{\lambda t}$, which leads to the equation $\left[ae^{-\lambda\tau}W - (1 + \lambda)\mathbb{1} \right]\mathbf{c} = \mathbf{0}$. In order to determine the conditions for a nontrivial solution to this equation to exist, we must solve the characteristic equation for the matrix $M = ae^{-\lambda\tau}W - \mathbb{1}$, i.e., we have to solve

$$\det(M - \lambda\mathbb{1}) = \begin{vmatrix} \tilde{M} & \mathbf{v} \\ \mathbf{u} & -(1+\lambda) \end{vmatrix} = 0 \,, \tag{6.9}$$

where we have introduced the abbreviations

$$\tilde{M} = \begin{pmatrix} -(1+\lambda)\mathbb{1}_{N\times N} & aw_{\alpha\beta}e^{-\lambda\tau}\mathbb{1}_{N\times N} \\ aw_{\beta\alpha}e^{-\lambda\tau}\mathbb{1}_{N\times N} & -(1+\lambda)\mathbb{1}_{N\times N} \end{pmatrix}, \tag{6.10}$$

$$\mathbf{u} = \left(aw_{\gamma\alpha}e^{-\lambda\tau}\mathbb{1}_{1\times N}, \mathbf{0}_{1\times N} \right), \qquad \mathbf{v} = \begin{pmatrix} aw_{\alpha\gamma}e^{-\lambda\tau}\mathbb{1}_{N\times 1} \\ aw_{\beta\gamma}e^{-\lambda\tau}\mathbb{1}_{N\times 1} \end{pmatrix}. \tag{6.11}$$

Solving (6.9) is facilitated by applying the identity [30]

$$\det(M) = -\det(\tilde{M})\left[1 + \lambda - \mathbf{u}\tilde{M}^{-1}\mathbf{v} \right]. \tag{6.12}$$

The inverse of $\tilde{M}$ is given by

$$\tilde{M}^{-1} = -\frac{1}{(1+\lambda)^2 - a^2 w_{\alpha\beta}w_{\beta\alpha}e^{-2\lambda\tau}} \begin{pmatrix} (1+\lambda)\mathbb{1}_{N\times N} & aw_{\alpha\beta}e^{-\lambda\tau}\mathbb{1}_{N\times N} \\ aw_{\beta\alpha}e^{-\lambda\tau}\mathbb{1}_{N\times N} & (1+\lambda)\mathbb{1}_{N\times N} \end{pmatrix}, \tag{6.13}$$

and we thus obtain

$$\begin{aligned} \det(M - \lambda\mathbb{1}) &= Na^2 w_{\gamma\alpha}e^{-2\lambda\tau}\left[aw_{\alpha\beta}w_{\beta\gamma}e^{-\lambda\tau} + w_{\alpha\gamma}(1+\lambda) \right] \\ &\times \left[(1+\lambda)^2 - a^2 w_{\alpha\beta}w_{\beta\alpha}e^{-2\lambda\tau} \right]^{N-1} - (1+\lambda)\left[(1+\lambda)^2 - a^2 w_{\alpha\beta}w_{\beta\alpha}e^{-2\lambda\tau} \right]^N. \end{aligned} \tag{6.14}$$
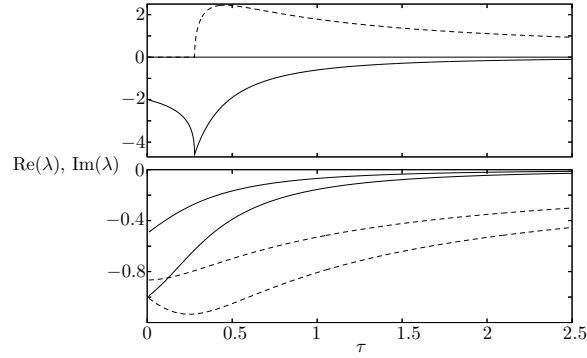
Figure 6.6: Eigenvalues of M as a function of the delay τ. Real parts of eigenvalues are shown by solid lines, imaginary parts by dashed lines. The upper panel shows real and imaginary part of λ_3, and the lower panel shows real and imaginary of λ_{1-} and λ_{2-}.

For the case $(-,+,+)$ the characteristic equation simplifies to

$$\left[1 + e^{3\lambda\tau}(1+\lambda)^3\right]\left[e^{-2\lambda\tau} + (1+\lambda)^2\right]^N = 0\,. \tag{6.15}$$

Its solutions, the eigenvalues of M, are given by

$$\lambda_{1\pm} = -1 + \frac{1}{\tau}W(\pm i\tau e^\tau),\ \ \lambda_{2\pm} = -1 + \frac{1}{\tau}W\left[\left(\frac{1}{2} \pm i\frac{\sqrt{3}}{2}\right)\tau e^\tau\right],\ \ \lambda_3 = -1 + \frac{1}{\tau}W(-e^\tau\tau). \tag{6.16}$$

Here, $W(z)$ is the inverse function to $W^{-1}(z) = ze^z$, which is usually called the Lambert W-Function. Figure 6.6 shows the real and imaginary parts of the eigenvalues of M as a function of the delay τ. For all values of τ there is no eigenvalue with a positive real part and the fixed point $\bar{\mathbf{V}}$ is thus stable for arbitrary delays. However, the real parts of the eigenvalues tend to zero faster than their respective imaginary parts as the delay is increased. Therefore, with increasing delay, the relaxation time for the system's return to the stationary point grows more rapidly than the time scale for oscillations. Thus, with increasing delay, the system will spiral toward the fixed point, explaining the observed oscillatory behavior.

6.6   Summary and discussion

We have investigated the circumstances under which the isthmic system can function as a WTA network. We have constructed a rate-model of the isthmotectal feedback loop and have analyzed the temporal evolution of the model system in response to a static stimulus. We have shown that time delays can be crucial to the dynamical behavior of the system. In particular, delay-induced oscillations can lead to transient WTA selection in our model. Finally, we have performed a linear stability analysis explaining the origin of the oscillatory behavior.

It has been conjectured for a long time that the isthmotectal feedback loop constitutes a WTA network. Our results show that the isthmic circuitry is indeed set up to perform such a selection rule. In the case where global inhibition and local excitation are present in the system, this result is quite intuitive. However, a network with global excitation and local inhibition might not appear to be well-suited as WTA selector. Yet, precisely such a scenario was discussed in the literature. Temporal delays can be crucial for the behavior of a dynamical system, and, as we have shown in our investigation, they are particularly important for the case of global excitation and local inhibition, as they induce transient WTA behavior in the network. Transmission and synaptic delays for the projections between Ipc and TeO are estimated to be around 15ms [31], whereas membrane time constants in the Ipc may be as short as a few milliseconds [32], which is within the range of typical neuronal membrane time constants [33]. When the synaptic and transmission delays are of the same order of magnitude as the membrane time constants involved, the degree to which our model for the isthmic system functions as a WTA network, can depend crucially on the delays (cf. Fig. 6.5). Therefore, temporal delays should not be neglected when the neuronal dynamics of the isthmotectal feedback loop are assessed and its potential for WTA selection is discussed.

6.7   Acknowledgments

References

[1] L. Itti, and C. Koch, Nat. Rev. Neurosci. **2**, 194 (2001).

[2] C. Koch and S. Ullman, Hum. Neurobiol. **4**, 219 (1985).

[3] A. Amari and M. A. Arbib in *Systems Neuroscience* edited by J. Metzler (Academic Press, New York, 1977), p. 119.

[4] R. Coultrip, R. Granger, and G. Lynch, Neural Networks **5**, 47 (1992).

[5] S. Kaski and T. Kohonen, Neural Networks **7**, 973 (1994).

[6] C. Indiveri and T. Delbrück in *Analog VLSI: Circuits and Principles* edited by S.-C. Liu et al. (MIT Press, Cambridge, 2002), Chap. 6.

[7] D. I. Standage, T. P. Trappenberg, and R. M. Klein, Neural Networks **18**, 620 (2005).

[8] L. Itti, C. Koch, and E. A. Niebur, IEEE T. Pattern. Anal. **20**, 1254 (1998).

[9] D. L. Sparks, Physiol. Rev. **66**, 118 (1986).

[10] R. H. Wurtz and J. E. Albano, Annu. Rev. Neurosci. **3**, 189 (1980).

[11] I. T. Diamond, D. Fitzpatrick, and M. Conley, J. Comp. Neurol. **316**, 375 (1992).

[12] Y. Wang, D. E. Major, and H. J. Karten, J. Comp. Neurol. **469**, 275 (2004).

[13] Y. Wang, H. Luksch, N. C. Brecha, and H. J. Karten, J. Comp. Neurol. **494**, 7 (2004).

[14] G. Marín, J. Mpodozis, E. Sentis, T. Ossandón, and J. C. Letelier, J. Neurosci. **25**, 7081 (2005).

[15] P. Andersen, J. C. Eccles, and Y. Løyning, J. Neurophysiol. **27**, 608 (1964).

[16] C. Hauptmann and M. C. Mackey, Biol. Cybern. **88**, 459 (2003).

[17] B. D. Coleman and G. H. Renninger, SIAM J. Appl. Math. **31**, 111 (1976).

[18] K. P. Hadeler and J. Tomiuk, Arch. Rat. Mech. Anal. **65**, 87 (1977).

[19] U. an der Heiden, J. Math. Bio. **8**, 345 (1979).

[20] M. Schanz and A. Pelster, Phys. Rev. E **67**, 056205 (2003).

[21] W. Wischert, A. Wunderlin, A. Pelster, M. Olivier, and J. Groslambert, Phys. Rev. E **49**, 203 (1994).

[22] J. Milton, *Dynamics of Small Neural Populations* (Amer. Math. Soc., Providence, 1996).

[23] Y.-C. Wang and B. J. Frost, Exp. Brain Res. **87**, 624 (1991).

[24] S.-R. Wang, Y.-C. Wang, and B. J. Frost, Exp. Brain Res. **104**, 376 (1995).

[25] Y. Wang, J. Xiao, and S.-R. Wang, J. Comp. Physiol. A, **186**, 505 (2000).

[26] S.-R. Wang, Brain. Res. Rev. **41**, 13 (2003).

[27] J. J. Hopfield, Proc. Natl. Acad. Sci. U.S.A. **81**, 3088 (1984).

[28] C. M. Marcus and R. M. Westervelt, Phys. Rev. A **39**, 347 (1989).

[29] G. B. Ermentrout, Rep. Prog. Phys. **61**, 353 (1998).

[30] V. V. Pasolov *Problems and Theorems in Linear Algebra* (Amer. Math. Soc., Providence, 1994).

[31] U. Netzel, R. Wessel, and H. Luksch, poster presented at the 36th annual SfN meeting (Atlanta, 2006), abstract 240.3.

[32] J. Shao (personal communication).

[33] C. Koch, *Biophysics of Computation: Information Processing in Single Neurons* (Oxford Univ. Press, New York, 1999).

Chapter 7

The isthmotectal feedback loop as a winner-take-all and novelty detection circuit

Recent experiments conducted in the avian isthmotectal feedback loop demonstrate that this neural circuit can gate the ascending flow of visual information. Furthermore, it was shown that the system exhibits sensitivity to novel stimuli. In standard models of selective visual attention, the most salient stimulus in a visual scene is chosen through a 'winner-take-all' selection mechanism, and attention can then be directed towards it. Taking into account known anatomical and electrophysiological properties of the isthmotectal circuitry, we examine under which circumstances the system can function as a 'winner-take all' and novelty detection circuit. We optimize the parameters in our network model through application of a genetic algorithm and consider possible parameter combinations in the biological system.

7.1   Introduction

In their environment, animals are constantly confronted with a myriad of visual stimuli. Among the available stimuli, the animal must thus select certain ones for attention. This selection should be such that the selected stimulus or location is more likely to be important or relevant to the animal [1].

This ability to select and orient towards the most salient part in a visual environment has evolutionary significance, as it permits the organism to choose a possible prey and to detect quickly predators or mates [2]. Attentional selection can be goal-directed (top-down), such as during reading when the gaze is directed to the text locations, or mediated through autonomous mechanisms (bottom up) along the visual pathway. In models of bottom-up visual attention, the stimulus is encoded in a 'saliency map' that topographically represents the conspicuity of the stimuli over the visual scene. The most salient location is then chosen by a 'winner-take-all' (WTA) network, i.e., by a neurally implemented maximum detector [3].

The optic tectum (TeO, mammalian homolog: superior colliculus, SC) is the primary visual center in the midbrain of non-mammalian vertebrates. It has long been known to be critically involved in localizing visual objects and in the preparation of orienting responses towards these objects [4–7]. Less well-known is the fact that the TeO/SC is reciprocally connected to and strongly affected by a smaller midbrain nucleus called the nucleus isthmi (NI) in nonmammalian and parabigeminal nucleus in mammalian vertebrates [8]. In the avian visual pathway, the NI consists of three subnuclei: the nucleus pars parvocellularis (Ipc), the nucleus pars magnocellularis (Imc), and the nucleus pars semilunaris [9, 10]. In both Ipc and Imc the projection from the tectum is topographically organized such that the retinotopic map is preserved in both nuclei, with the projection to the Imc being somewhat coarser than for the Ipc. In contrast, the isthmic projections back to the TeO are very different for Ipc and Imc. Ipc neurons project back to the TeO in a precise homotopic manner, i.e., the axons of each Ipc neuron terminate in that part of the optic tectum from which their visual inputs come. Imc, on the other hand, has two populations of neurons, which make heterotopic projections but only to the TeO or Ipc, respectively. Anatomical studies furthermore indicate that a given cell in the Imc does not project back to the locus in the TeO, or to the corresponding locus in the Ipc, from which it receives input, whereas it does project to all other locations [9, 10]. In this sense, the feedback from the Imc can be termed 'antitopographic.' The anatomy of the isthmotectal feedback loop is shown in Fig. 7.1. Ipc neurons are cholinergic, whereas Imc neurons have been shown to express gamma-aminobutyric acid (GABA) as their main neurotransmitter. Thus, according to the usual role of acetylcholine and GABA, one would assume that Ipc and Imc neurons mediate excitation and inhibition onto their target cells, respectively. Taking into account the connectivity between TeO, Ipc, and Imc, it then seems immediately plausible that "the three-nuclei circuitry [...]
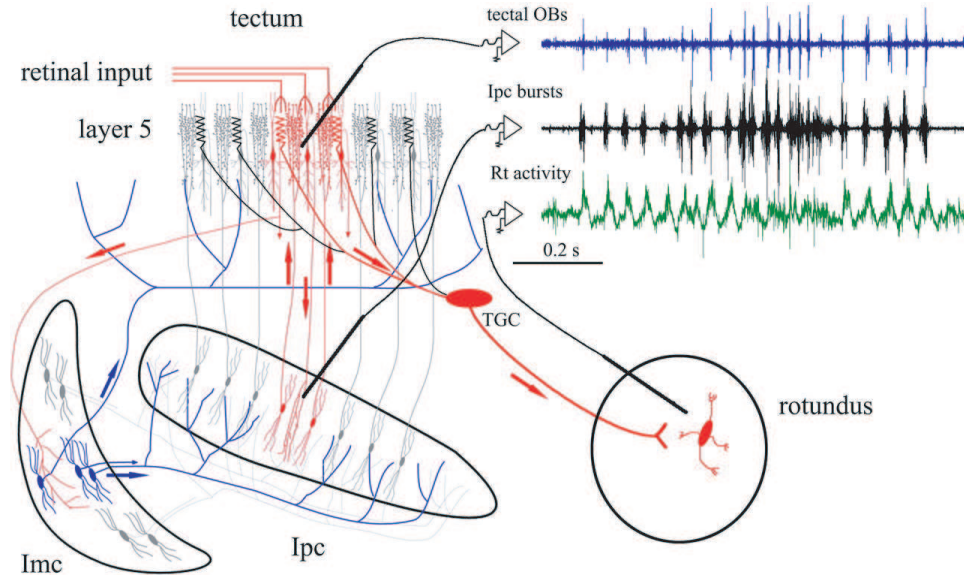
Figure 7.1: (Color) Diagram of the isthmotectal feedback loop and modulation of the ascending flow of visual activity. The schematic illustrates the synaptic connectivity between NI and TeO. Neurons in Ipc receive a topographically organized visual input from tectal 'shepherd's crook' neurons and project back to the homotopic location via cholinergic paintbrush axon terminals. Imc neurons receive a coarser projection from tectal neurons and send widely ramifying, GABAergic terminal fields on most of the Ipc and the TeO. The densest paintbrush ramifications colocalize with the retinal terminals and the dendritic bottlebrushes of type I tectal ganglion cells (TGC), whose axons project to the nucleus rotundus. The recording traces show that the synchronized, visually evoked bursting responses recorded at homotopic locations in Ipc and TeO are also synchronized to extracellular activity recorded in the dorsal anterior division of the nucleus rotundus. OB, Oscillatory bursting potential. Reprinted with permission from Ref. [8].

may constitute a winner-take-all network [3] in which local visual inputs to the Ipc are augmented by the re-entrant loop among tectal and Ipc neurons, combined with broad inhibition of the rest of the Ipc by Imc neurons [11]."

Recent experiments in birds have revealed that the Ipc crucially modulates the ascending flow of visual information from the TeO to the diencephalon by providing a gating mechanism for visual stimuli [12]. In their investigation, the authors of Ref. [12] show that local inactivation of the Ipc prevents visual responses in the nucleus rotundus, which constitutes the next level in the avian visual pathway, to objects moving in the corresponding region of visual space. Therefore, in order for a visual stimulus to be further processed by the visual system, the corresponding location in the Ipc must be active. Conversely, if the corresponding location in the Ipc is inactive, the stimulus is discarded for further processing. Furthermore, the results presented in Ref. [12] demonstrate that the

Ipc exhibits sensitivity to novel stimuli. Recording visually evoked activity in the Ipc, the authors of Ref. [12] find that when a second visual stimulus is presented, the response to a first stimulus is suppressed. They then to demonstrate that this suppression is mediated by the GABAergic Imc. These findings provide further support to the concept of the isthmotectal feedback loop as a WTA selection circuit.

The anatomy of the isthmotectal feedback loop is known in great detail and the main neurotransmitters involved in the circuit have been identified [9, 10, 18–21]. Furthermore, certain single cell properties, such as membrane time constants or resting potentials were determined in electrophysiological experiments [22, 23], and the distributions of the transmission delays between the components of the feedback loop have been measured [13]. On the other hand, quantities that determine the network behavior of the system such as the strength of synaptic interactions are unknown. In this work, based on the experimental findings described above, we study the circumstances under which the isthmotectal feedback loop can function as a WTA and novelty detection (ND) circuit. In Sect. 7.2 we describe our model for the isthmotectal feedback loop and discuss which parameters we keep fixed and which are variable in our study. In Sect. 7.3 we report what kind of simulations we performed with the network model and how we evaluated its ability to function as a WTA and ND circuit. We show how we optimized the system parameters for these tasks through a genetic algorithm (GA) in Sect. 7.4. Section 7.5 contains a discussion of what parameters appear to be crucial for the system's performance and how the different parameter values might relate to each other in the biological system. A summary concludes the paper in Sect. 7.6.

7.2 Model and Parameters

We consider a network model of integrate-and-fire neurons as described, e.g., in Ref. [24]. The model neuron behaves like an electric circuit consisting of a resistor and a capacitor in parallel. Furthermore, it is stipulated that an action potential occurs whenever the membrane potential of the model neuron reaches a threshold value V_{th}. Subsequently, the membrane potential is reset to a value V_r below the threshold potential, $V_r < V_{th}$. The temporal evolution of the membrane potential

of the ith neuron, $V_i(t)$, is then determined by the differential equation

$$\tau_{\mathrm{m},i}\frac{dV_i(t)}{dt} = E_{\mathrm{L},i} - V_i(t) + \frac{I_i(t)}{g_{\mathrm{m},i}A_i} \tag{7.1}$$

and the update rule

$$V_i(t_{0,i}+) = V_{\mathrm{r},i} \qquad \text{if} \qquad V_i(t_{0,i}-) = V_{\mathrm{th},i}\,. \tag{7.2}$$

Here, $\tau_{\mathrm{m},i}$ is the membrane time constant, $g_{\mathrm{m},i}$ the specific membrane conductance, $E_{\mathrm{L},i}$ the resting potential, A_i the membrane surface area, and $I_i(t)$ an input current; furthermore $t_{0,i}$ denotes a firing time of the ith neuron, i.e., the neuron reaches firing threshold at $t_{0,i}$ and emits an action potential. In order to number the firing times of the ith neuron, we introduce an additional index k, such that $t_{0,i}^{(k)}$ is the time at which the ith neuron emits its kth spike. The input current $I_i(t)$ consists of an external input, synaptic currents due to the coupling to other neurons in the network, a spike-rate adaptation current, and a stochastically varying current representing noise or background activity:

$$I_i(t) = I_{\mathrm{e},i}(t) + I_{\mathrm{syn},i}(t) + I_{\mathrm{sra},i}(t) + \eta_i(t)\,. \tag{7.3}$$

In the following, we briefly describe the four contributions to the input current in our model. The external input current $I_{\mathrm{e},i}(t)$ represents a stimulus and we assume that more salient stimuli give rise to stronger currents. The saliency of an object does not necessarily correspond to single stimulus features in a straightforward way. For instance, it has been reported that when confronted with two possible preys, frogs choose the one located more rostrally, even when a more caudally located but otherwise equal prey is at a much shorter distances [25]. The total synaptic current flowing into the ith neuron $I_{\mathrm{syn},i}(t)$, is obtained by summing over all currents resulting from projections onto the ith neuron: $I_{\mathrm{syn},i}(t) = \sum_j I_{ij}(t)$. Here $I_{ij}(t)$ is the current due to a projection from the jth to the ith neuron in the network. It is given by

$$I_{ij}(t) = -\bar{g}_{ij}A_iP_j(t-\tau_{ij})[V_i(t) - E_{\mathrm{s},j}]\,, \tag{7.4}$$

where $\bar{g}_{ij}$ is a specific conductance and represents the synaptic weight for the projection from the jth to the ith neuron. Furthermore, $E_{\mathrm{s},j}$ is the reversal potential for the corresponding synaptic current and τ_{ij} the transmission delay for the projection. The quantity $P_j(t)$ denotes a gating variable which describes the degree to which the synaptic conductance from the jth to the ith neuron is active. It is given by the equation

$$P_j(t) = B \sum_k \left\{ \exp[-(t - t_{0,j}^{(k)})/\tau_1] - \exp[-(t - t_{0,j}^{(k)})/\tau_2] \right\}, \tag{7.5}$$

where the sum is over all spikes emitted by the jth neuron prior to time t. The constant B is a normalization constant that assures that the peak value of P during a single synaptic event is equal to one. It is given by

$$B = \left[\left(\frac{\tau_2}{\tau_1} \right)^{\tau_{\mathrm{rise}}/\tau_1} - \left(\frac{\tau_2}{\tau_1} \right)^{\tau_{\mathrm{rise}}/\tau_2} \right]^{-1}. \tag{7.6}$$

The rise time of the synapse is determined by $\tau_{\mathrm{rise}} = \tau_1 \tau_2/(\tau_1 - \tau_2)$, while the fall time is set by τ_1. The spike-rate adaptation current I_{sra} is added to the model to include the possibility that interspike intervals lengthen over time when a constant current is injected into the cell. The spike-rate adaptation current is given by

$$I_{\mathrm{sra},i}(t) = g_{\mathrm{sra},i}(t) A_i \left[V_i(t) - E_{\mathrm{sra},i} \right]. \tag{7.7}$$

Here, $E_{\mathrm{sra},i}$ denotes the reversal potential for the spike-rate adaptation current of the ith neuron, and the specific conductance $g_{\mathrm{sra},i}(t)$ is modeled according to

$$\frac{dg_{\mathrm{sra},i}(t)}{dt} = -\frac{g_{\mathrm{sra},i}(t)}{\tau_{\mathrm{sra},i}} \tag{7.8}$$

and

$$g_{\mathrm{sra},i}(t_{0,i}+) = g_{\mathrm{sra},i}(t_{0,i}-) + \Delta g_{\mathrm{sra},i}. \tag{7.9}$$

The stochastic currents $\eta_i(t)$, finally, are modeled by Gaussian white noise, i.e.,
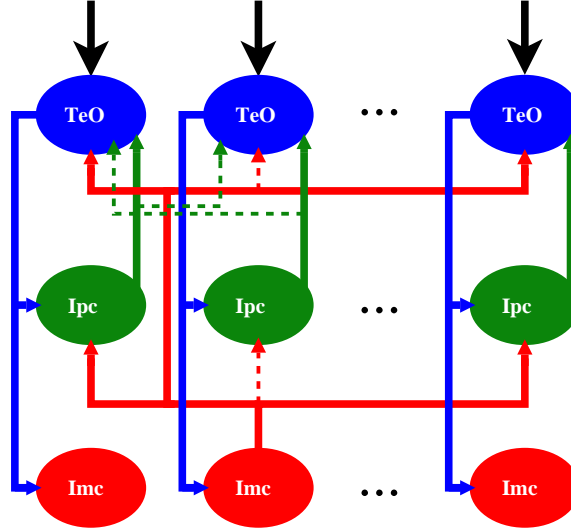
Figure 7.2: (Color) Diagrammatic representation of the synaptic connections in the isthmotectal feedback loop model. Projections that, depending on the model parameters, may be relatively weak are shown by broken lines. The black arrows indicate external input. In the Imc, the feedback projections to the TeO and Ipc are only shown for one neuron.

$$\langle \eta_i(t_1)\eta_j(t_2) \rangle = 2\sigma_i^2 A_i^2 \delta(t_1 - t_2)\delta_{ij} \,. \tag{7.10}$$

In our model, we allow for three different types of neurons: tectal neurons, Ipc neurons, and Imc neurons. The total number of neurons is $N = N_{\text{TeO}} + N_{\text{Ipc}} + N_{\text{Imc}}$. We number the neurons such that indices i with $1 \leq i \leq N_{\text{TeO}}$, $N_{\text{TeO}} + 1 \leq i \leq N_{\text{TeO}} + N_{\text{Ipc}}$, and $N_{\text{TeO}} + N_{\text{Ipc}} + 1 \leq i \leq N_{\text{TeO}} + N_{\text{Ipc}} + N_{\text{Imc}}$ label tectal, Ipc, and Imc neurons, respectively. The model parameters may differ between the three groups of neurons. However, within each group we take the parameters to be homogeneous. Furthermore, we assume an equal number of neurons in each of the three groups. For the synaptic weights $\bar{g}_{ij}$, we make the following assumptions that are motivated by biological and electrophysiological studies [22, 23]. We assume that a tectal neuron projects to one neuron in the Ipc and one neuron in the Imc each. The feedback projections from the Ipc and the Imc are chosen such that a projection from a neuron in the Ipc targets the tectal neuron from which it receives its input, but also neighboring neurons with exponentially decreasing strength. For the projection from Imc, we allow for the possibility that the tectal neuron which projects to the Imc neuron receives weaker feedback than more distant tectal neurons. The topological organization of our model network is depicted in Fig. 7.2, and the synaptic weights for the projections are given

$\bar{g}_{ij}$	$1 \le j \le N_1$	$N_1 + 1 \le j \le N_2$	$N_2 + 1 \le j \le N$
$1 \le i \le N_1$	0	$\bar{g}_{\text{Ipc}\to\text{TeO}}$ $\times e^{-(i-j+N_1)^2/w_{\text{Ipc}\to\text{TeO}}^2}$	$\bar{g}_{\text{Imc}\to\text{TeO}}$ $\times \left[1 - w_{\text{Imc}\to\text{TeO}}\, e^{-(i-j+N_2)^2/w_{\text{Imc}}^2}\right]$
$N_1 + 1 \le i \le N_2$	$\bar{g}_{\text{TeO}\to\text{Ipc}}\, \delta_{i-N_1,j}$	0	$\bar{g}_{\text{Imc}\to\text{Ipc}}$ $\times \left[1 - w_{\text{Imc}\to\text{Ipc}}\, e^{-(i-j+N_1)^2/w_{\text{Imc}}^2}\right]$
$N_2 + 1 \le i \le N$	$\bar{g}_{\text{TeO}\to\text{Imc}}\, \delta_{i-N_2,j}$	0	0

Table 7.1: Model connectivity and synaptic weights. The connections from tectal neurons to Ipc and Imc neurons are assumed to be exactly topographic. The projection from the Ipc to the TeO is also topographic but somewhat broader depending on the parameter $w_{\text{Ipc}\to\text{TeO}}$. The projections from Imc to Ipc and TeO are homogeneous or 'antitopographic' depending on the parameters $w_{\text{Imc}\to\text{TeO}}$ and $w_{\text{Imc}\to\text{Ipc}}$, respectively. For simplicity, the abbreviations $N_1 = N_{\text{TeO}}$ and $N_2 = N_{\text{TeO}} + N_{\text{Ipc}}$ were introduced.

in Tab. 7.1.

For our investigation of the system's performance as a WTA and novelty detector, we specify those neuron parameters that have been estimated in single-cell electrophysiological experiments. For other parameters, we either choose standard values from the literature or keep them variable and study their influence on the system dynamics. For those parameters we assign a minimum and maximum value, where we usually set the minimum to zero and determine the maximum according to physiological constraints.

We are especially interested in studying the synaptic connectivity of the feedback loop and therefore keep the synaptic weights for the five different projections variable. Also, the three space constants $w_{\text{Ipc}\to\text{TeO}}$, $w_{\text{Imc}\to\text{TeO}}$, and $w_{\text{Imc}\to\text{Ipc}}$, which determine to which degree the feedback from Ipc is exactly topographic and the feedback from Imc is homogeneous or 'antitopographic', will be variable parameters in our study. The spatial separation between the three elements of the feedback loop suggests that temporal delays may influence the circuits performance. Temporal delays can be crucial for the dynamics of neural systems [14–16] and have been shown to potentially influence the ability of the isthmotectal feedback loop to function as a WTA detector [17]. Therefore, they will also be variable parameters. Since experiments indicate that the isthmotectal system responds to novel stimuli, adaptation could be an important feature of the neurons in the feedback loop and we model different degrees of adaptive firing by varying the parameter Δg_{sra} within each of the three groups of neurons. Finally, electrophysiological experiments indicate that the nucleus isthmi

parameter	value/range
$\tau_{m,TeO}$, $\tau_{m,Ipc}$, $\tau_{m,Imc}$ [*]	100 ms, 25 ms, 35 ms
$E_{L,X}$ [*]	-60 mV
$V_{th,X}$ [*]	-40 mV
$V_{r,X}$ [*]	-65 mV
$g_{m,X}$ [**]	1 $\mu S/mm^2$
$E_{s,TeO}$, $E_{s,Ipc}$, $E_{s,Imc}$,	0 mV, 0 mV, -70 mV
$\tau_{1,X}$, $\tau_{2,X}$ [**]	5 ms, 0.3 ms
$E_{sra,X}$ [**]	-70 mV
$\tau_{sra,X}$ [**]	100 ms
w_{Imc}	$N_{Imc}/6$
$\Delta g_{sra,X}$	0 $\mu S/mm^2$ $\cdots$ 0.5 $\mu S/mm^2$
$\tau_{Ipc,Imc\rightarrow TeO}$, $\tau_{TeO,Imc\rightarrow Ipc}$, $\tau_{TeO\rightarrow Imc}$	0.5 ms $\cdots$ 12.5 ms
σ_X	0 nA/mm^2 $\cdots$ 671 nA/mm^2
$\bar{g}_{Ipc,Imc\rightarrow TeO}$, $\bar{g}_{TeO,Imc\rightarrow Ipc}$, $\bar{g}_{TeO\rightarrow Imc}$	0 $\mu S/mm^2$ $\cdots$ 4 $\mu S/mm^2$
$w_{Ipc\rightarrow TeO}$	$0 \cdots N_{Ipc}/4$
$w_{Imc\rightarrow TeO,Ipc}$	$0 \cdots 1$

Table 7.2: Constant and variable model parameters. The upper part of the table shows parameters and their respective values that we kept fixed in the model. The lower part shows the variable parameters and their allotted ranges. Parameters marked by [*] were determined according to experimental data [22, 23], whereas the values of parameters marked by [**] were specified according to standard values given in the literature [26]. The synaptic reversal potentials for projections from tectal as well as Ipc neurons were chosen as 0 mV assuming that these neurons mediate excitation. The GABAergic Imc was assumed to mediate inhibition and the corresponding reversal potential was set to -70 mV. The space constant w_{Imc} was given a value comparable to the one found for the space constant $w_{Ipc\rightarrow TeO}$ in the GA optimization (cf. Sect 7.4). The ranges for the variable parameters were set such that the minimal parameter value corresponds to a certain limiting case (e.g., $\bar{g}_{Imc\rightarrow TeO} = 0$ signifies that there are no projections from Imc to Ipc), while maxima were determined by inspection of the resulting network behavior and physiological constraints.

exhibits considerable spontaneous activity [23]. To explore whether this noisy or background activity plays an important role, we take the standard deviation of the noisy currents in (7.10) to be variable, which gives us three more variable parameters. For all other parameters we either take experimentally determined values or use standard numbers from the literature [26]. In total we have thus 19 free parameters of the system. Table 7.2 shows the values and ranges of the fixed and variable parameters, respectively. For each variable parameter, we allow ten possible values which are indicated by a parameter index ranging from zero to nine, where index values of zero and nine correspond to the minimal and maximal parameter values respectively.

7.3   Network Simulations and Performance Measures

The model has 19 free parameters with 10 allotted values each. Drawing parameter combinations randomly from these 10^{19} possibilities, we simulated the dynamics that resulted for a network consisting of $N = 60$ neurons, with $N_{\text{TeO}} = N_{\text{Ipc}} = N_{\text{Imc}} = 20$. We then evaluated whether a given network could perform WTA selection and ND. To this end, we examined the network's response to a stimulus represented as an external input current to the tectal cells. The stimulus consisted of two superimposed Gaussians $s_1(i)$ and $s_2(i)$ and was given as $I_{\text{e},i}(t) = s_1(i)f_1(t) + s_2(i)f_2(t)$. The two Gaussians $s_1(i)$ and $s_2(i)$ describe the spatial structure of the stimulus, while $f_1(t)$ and $f_2(t)$ give the respective temporal structures of the two components. For the spatial structure of the stimulus, we had

$$s_{1/2}(i) = \begin{cases} I_0 e^{-2(i-p_{1/2})^2/N_{\text{TeO}}} & \text{for } i \leq N_{\text{TeO}}, \\ 0 & \text{for } i > N_{\text{TeO}}, \end{cases} \tag{7.11}$$

where the peaks of these Gaussian were set at $p_1 = 6$ and $p_2 = 13$. We then specified the temporal components of the stimulus to test for both WTA and ND behavior. In particular, the two stimuli were first presented simultaneously but with different amplitudes (WTA test). Afterwards, the two stimuli were presented sequentially but with equal amplitudes. The temporal components of the stimuli are shown at the top of Fig. 7.3. We assigned a WTA and ND score to the networks based on the number of spikes emitted by the neurons in the Ipc that corresponded to the location of the peaks in the stimulus. Denoting as n_1 and n_2 the number of spikes emitted by the neurons with indices $i = p_1 + N_{\text{TeO}}$, $p_1 + N_{\text{TeO}} \pm 1$ and $i = p_2 + N_{\text{TeO}}$, $p_2 + N_{\text{TeO}} \pm 1$ during the initial simultaneous presentation of the two Gaussian stimuli, we defined the WTA score as $S_{\text{WTA}} = (n_1 - n_2)/(n_1 + n_2)$. Similarly, denoting m_1 and m_2 as the number of spikes emitted by the same groups of neurons but during the phase in which which both Gaussian stimuli were present with equal amplitudes, we defined the ND score as $S_{\text{ND}} = (m_2 - m_1)/(m_1 + m_2)$. The total score of the network was then determined by taking the smaller of the two scores. Additionally, restrictions on the minimum and maximum firing rates realized in the networks were imposed, and networks whose firing rates lay outside of this range were assigned a score of zero. For each network, five runs were simulated and the final network score S was determined by averaging the results from the five runs. Initially, we simulated 1000 randomly generated networks. Figure 7.3(a) shows the response
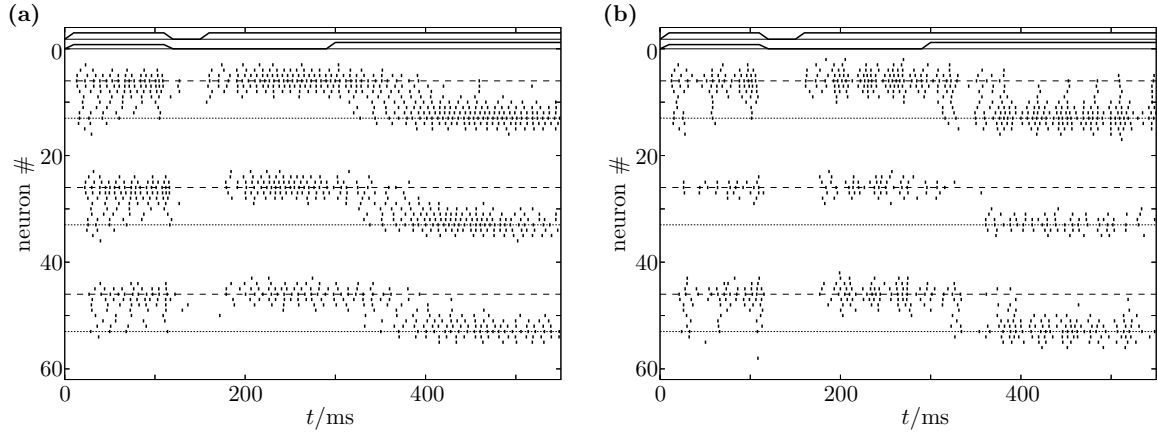
(a)

(b)

Figure 7.3: Raster plot of network output before and after GA optimization. The firing times of the sixty neurons in the network are indicated by tickmarks. The input consists of two superimposed Gaussians and the time courses for the two components are shown at the top of the figures. The position of the neurons in the TeO and the corresponding locations in the Ipc and Imc that coincide with the peaks of the Gaussians are shown by dashed and dotted lines. **(a)** shows the output of the best performing network among 1000 randomly generated networks. **(b)** shows the output of the best performing network after optimization with the GA.

dynamics of the best performing network among these 1000 random networks; it achieved a WTA score of $S_{\mathrm{WTA}} = 0.49$ and a ND score of $S_{\mathrm{ND}} = 0.85$. To examine what combinations of parameter values would lead to improved WTA and ND behavior we optimized the network performance by employing a GA.

7.4   Parameter Optimization via Genetic Algorithm

In order to optimize the performance of our model networks we used a GA to search for parameter combinations that would lead to improved WTA and ND behavior. This optimization method is inspired by evolutionary biology and is based on the principles of selection, inheritance, crossover, and mutation [27, 28]. We ran the algorithm for twenty generations of 50 networks each, where an individual network was characterized by its parameter indices for the 19 variable parameters in the model. The performance of the network in the WTA and ND tasks was then evaluated as described above. The score S was used as a fitness value in order to assign a percentile rank r_i to each network in the generation (selection). Here, the value of r_i indicates what percentage of networks received a score lower than that of the ith network. The parameter values of the networks

were then updated according to their rank (inheritance and crossover). Finally, random changes in the parameter indices were performed (mutation). In particular, we used the following scheme in order to update the parameter indices of the ith network from generation to generation:

- If $r_i \leq 0.5$: All parameters of the ith network were changed through crossover with either the best-, second-best, or third-best performing network in the generation, i.e., among the three best performing networks one was randomly chosen and then used for crossover with the ith network. Each of the parameters of the ith network was updated by either taking the value of the network chosen for the crossover or by taking the arithmetic mean between the parameter value of the 'partner' network and the ith network. Both possibilities had probability $1/2$. After this crossover was completed, for every parameter of the updated ith network a random change (mutation) occurred with probability $1/10$. If a mutation occurred, the parameter index was assigned a randomly chosen value between 0 and 9.

- If $0.5 < r_i \leq 0.7$: Each parameter index of the ith network was changed with probability $1/3$ through crossover with the best performing network. If a change occurred, the parameter index value was changed with probability $1/2$ to the value of the best performing network, and with probability $1/2$ to the mean of the values of the best performing network and the ith network. After this crossover, parameter indices were changed to a neighboring value with probability $1/10$.

- If $0.7 < r_i \leq 0.8$: Same as for $0.5 < r_i \leq 0.7$, except that the probability for a parameter change through crossover with the best performing network was only $2/15$.

- If $0.8 < r_i \leq 0.9$: Same as for $0.5 < r_i \leq 0.7$, except that the probability for a parameter change through crossover with the best performing network was only $1/15$.

- If $0.9 < r_i$: Same as for $0.5 < r_i \leq 0.7$, except that the probability for a parameter change through crossover with the best performing network was only $1/30$.

- Finally, the network with the best performance was transferred to the next generation unchanged.

Figure 7.3(b) shows the response dynamics of the best performing network after 20 generations of GA optimization. The network achieved a WTA score of $S_{\mathrm{WTA}} = 1$ and a ND score of $S_{\mathrm{ND}} = 0.96$.
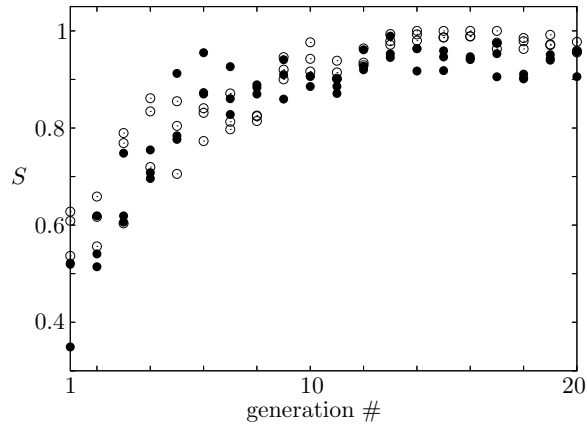
Figure 7.4: Convergence of the GA. The score S of the best three networks is shown versus the generation number. Open and filled dots depict results from two runs with different randomly chosen starting generations.

The network thus performed the assigned task almost perfectly. Figure 7.4 shows the score of the three best performing networks as a function of the generation in the GA. The algorithm converges quickly to very high performance scores. To test how sensitive the convergence of the GA would be to the randomly chosen starting generation of networks, we performed a second run with a different starting generation and obtained similar convergence behavior.

7.5 Network Parameters for WTA Selection and Novelty Detection

Applying the GA to optimize the performance of the feedback loop model in regard to WTA selection and ND yielded networks that accomplished the assigned task almost perfectly. In order to examine whether certain values of the variable parameters were preferred for these networks, we plot color coded histograms of parameter index value distributions vs. the generation number in the GA for each of the 19 variable parameters in Fig. 7.5. The histograms in Fig. 7.5 were obtained from networks with percentile rank $r > 0.5$ and results from two runs with different randomly generated starting generations are shown. Initially, all histograms are broad, which shows that the random search for networks with good performance did not yield any preferred parameter values. For most parameters, the distributions soon became narrower indicating that the GA converges to a specific region within the parameter space. However, the convergence behavior to a specific parameter value exhibits considerable variability for the individual parameters in Fig. 7.5. For instance,
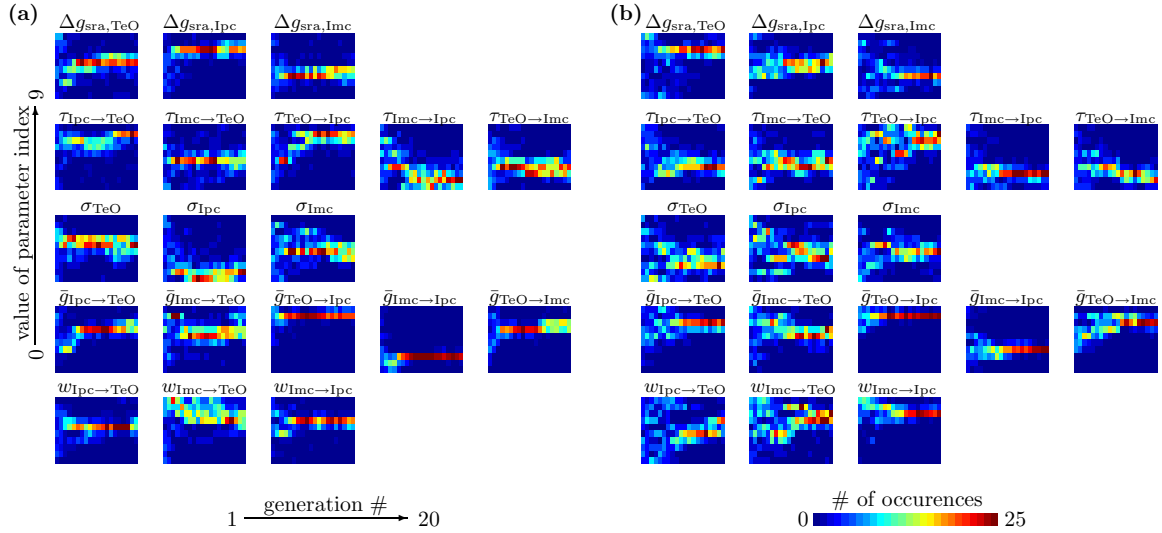
Figure 7.5: (Color) Parameter distributions and GA optimization. The distribution of parameter indices for the 19 variable parameters obtained from the 25 best performing networks in each generation is color coded and its evolution during 20 generations of the GA is shown. **(a)** and **(b)** are two runs with different randomly chosen starting generations.

the histogram for the parameter $\bar{g}_{\text{TeO}\rightarrow\text{Ipc}}$ becomes narrow very soon with the peak lying at identical parameter index values for both runs shown in Fig. 7.5. On the other hand, the histogram for the space constant $w_{\text{Imc}\rightarrow\text{TeO}}$ remains relatively broad throughout the GA optimization procedure. The two runs of the GA that we performed do not allow definite conclusions about what values of the parameters give rise to WTA and ND behavior. However, certain trends for preferred parameter values are apparent in Fig. 7.5. Assuming that a narrow histogram peaked at comparable parameter values for both runs in Fig. 7.5 indicates a preferred value for this parameter, we make the following conjectures on the cellular and connection properties of the isthmotectal feedback loop, supposing that the system is to perform WTA selection and ND: The synaptic weights are strongest for the projection TeO $\rightarrow$ Ipc, while the weakest projection is the one from Imc to Ipc. Other synaptic weights are of intermediate strength. The shortest latency in the system is the one for the projection Imc $\rightarrow$ Ipc, while the delay for the projection TeO to Ipc is considerably longer. The projections Imc $\rightarrow$ TeO and TeO $\rightarrow$ Imc are also fairly short. These results are consistent with measurements of the delay distributions in the isthmotectal feedback loop as comparison with Tab. 7.3 shows. The strength of the noise in the system seems not to be crucial, i.e., there is no preference for either high or low noise levels. The feedback projection from the Ipc to the TeO has a certain interme-

projection	Ipc → TeO	Imc → TeO	TeO → Ipc	Imc → Ipc	TeO → Imc
mean of measured delay distribution	7 ms	4.5 ms	6.5 ms	4.3 ms	5.2 ms

Table 7.3: Measured delays in the isthmotectal feedback loop. The distributions of the delays for the different projections between the elements of the isthmotectal feedback loop were measured through extracellular combined with intracellular recordings [13]. The table shows the means of the measured delay distributions.

diate width; it is not broad but it may target cells within a certain range. The projection from the Imc to both the TeO and the Ipc is not necessarily 'antitopographic;' however, it appears that less pronounced feedback to the location from which Imc cells receive their input is beneficial. There is some degree of spike rate adaptation in the system, with adaptation being weaker in Imc cells than in tectal or Ipc cells.

7.6   Summary

We have investigated the circumstances under which the isthmic system can function as a 'winner-take-all' and novelty detection network. We have simulated the dynamics of networks with randomly generated parameters. The network parameters were then optimized in regard to 'winner-take-all' selection and novelty detection by applying a genetic algorithm. We have shown that the topology of the isthmotectal feedback loop allows the system to perform both tasks almost perfectly when the parameter values in the model are optimized. We have examined the evolution of the parameter distribution histograms over the optimization process and have drawn conclusions on probable parameter combinations in the biological feedback system.

7.7   Acknowledgments

References

[1] L. Zhaoping, Network-Comp. Neural **17**, 301 (2006).

[2] L. Itti and C. Koch, Nat. Rev. Neurosci. **2**, 194 (2001).

[3] C. Koch and S. Ullman, Hum. Neurobiol. **4**, 219 (1985).

[4] G. E. Schneider, Science **163**, 895 (1969).

[5] D. Ingle, Science **181**, 1053 (1973).

[6] R. H. Wurtz and J. E. Albano, Annu. Rev. Neurosci. **3**, 189 (1980).

[7] D. L. Sparks, Physiol. Rev. **66**, 118 (1986).

[8] E. Gruberg, E. Dudkin, Y. Wang Y, G. Marín, C. Salas, E. Sentis, J. C. Letelier, J. Mpodozis, J. Malpeli, H. Cui, R. Ma, D. Northmore, and S. Udin, J. Neurosci. **26** 10368 (2006).

[9] Y. Wang, D. E. Major, and H. J. Karten, J. Comp. Neurol. **469**, 275 (2004).

[10] Y. Wang, H. Luksch, N. C. Brecha, and H. J. Karten, J. Comp. Neurol. **494**, 7 (2006).

[11] G. Marín, J. Mpodozis, E. Sentis, T. Ossandón, and J. C. Letelier, J. Neurosci. **25**, 7081 (2005).

[12] G. Marín, C. Salas, E. Sentis, X. Rojas, J. C. Letelier, and J. Mpodozis, J. Neurosci. **27**, 8112 (2007).

[13] U. Meyer, J. Shao, S. Chakrabarty, S. F. Brandt, H. Luksch, and R. Wessel, `arXiv:0712.0036 [physics.bio-ph]`.

[14] U. an der Heiden, J. Math. Bio. **8**, 345 (1979).

[15] S. F. Brandt, A. Pelster, and R. Wessel R, Phys. Rev. E **74**, 036201 (2006).

[16] S. F. Brandt, A. Pelster, and R. Wessel R, Europhys. Lett. **79**, 38001 (2007).

[17] S. F. Brandt and R. Wessel, Biol. Cybern. **97** 221 (2007).

[18] Y.-C. Wang and B. J. Frost, Exp. Brain Res. **87**, 624 (1991).

[19] S.-R. Wang, Y.-C. Wang, and B. J. Frost, Exp. Brain Res. **104**, 376 (1995).

[20] Y. Wang, J. Xiao, and S.-R. Wang, J. Comp. Physiol. A, **186**, 505 (2000).

[21] S.-R. Wang, Brain. Res. Rev. **41**, 13, (2003).

[22] U. Netzel, R. Wessel, and H. Luksch, poster presented at the 36th annual SfN meeting (Atlanta, 2006), abstract 240.3.

[23] U. Netzel and J. Shao (personal communication).

[24] D. Hansel, G. Mato, C. Meunier, and L. Neltner, Neural Comput. **10**, 467 (1998).

[25] E. Gruberg (personal communication).

[26] P. Dayan and L. F. Abbott, *Theoretical Neuroscience* (MIT Press, Cambridge, 2001).

[27] J. H. Holland *Adaptation in Natural and Artificial Systems* (MIT Press, Cambridge, 1975).

[28] M. Mitchell *An Introduction to Genetic Algorithms* (MIT Press, Cambridge, 2001).

Chapter 8

Noise-dependent stability of the synchronized state in a coupled system of active rotators

We consider a Kuramoto model for the dynamics of an excitable system consisting of two coupled active rotators. Depending on both the coupling strength and the noise, the two rotators can be in a synchronized or desynchronized state. The synchronized state of the system is most stable for intermediate noise intensity in the sense that the coupling strength required to desynchronize the system is maximal at this noise level. We evaluate the phase boundary between synchronized and desynchronized states through numerical and analytical calculations.

8.1   Introduction

Networks of coupled nonlinear oscillators provide useful model systems for the study of a variety of phenomena in physics and biology [1]. Among many others, examples from physics include solid-state lasers [2] and coupled Josephson junctions [3, 4]. In biology, the central nervous system can be described as a complex network of oscillators [5], and cultured networks of heart cells are examples of biological structures with strong nearest-neighbor coupling [6]. In particular, the emergence of synchrony in such networks [7, 8] has received increased attention in recent years.

Disorder and noise in physical systems usually tend to destroy spatial and temporal regularity. However, in nonlinear systems, often the opposite effect is found and intrinsically noisy processes, such as thermal fluctuations or mechanically randomized scattering, lead to surprisingly ordered patterns [9]. For instance, arrays of coupled oscillators can be synchronized by randomizing the phases of their driving forces [10, 11]. Synchronization in these systems is caused by the interactions between the elements and results in the emergence of collective modes. It has been shown to be a fundamental mechanism of self-organization and structure formation in systems of coupled oscillators [12]. Biological systems of neurons are subject to different sources of noise, such as synaptic noise [15] or channel noise [13]. In particular, sensory neurons are notoriously noisy. Therefore, the question arises how stochastic influences affect the functioning of biological systems. Especially interesting are scenarios in which noise enhances performance. In the case of stochastic resonance [14], e.g., noise can improve the ability of a system to transfer information reliably, and the presence of this phenomenon in neural systems has been investigated [16, 17]. Furthermore, numerous studies have addressed the effect of noise on the dynamics of limit cycle systems [12, 18–23].

Small neural circuits composed of two or three neurons form the basic feedback mechanisms involved in the regulation of neural activity [24]. They can display oscillatory activity [25, 26] and serve as central pattern generators involved in motor control [27]. Here, we consider a system of two limit cycle oscillators with repulsive coupling. We investigate the influence of the noise and the coupling strength on the dynamics of the system. We distinguish between two different classes of dynamics, a synchronized state, in which the joint probability density of the oscillator phases is characterized by a single-hump shape, and a desynchronized state. The single-hump shaped distribution of the oscillator phases has been modeled by a Gaussian distribution [12, 28], and systems consisting of a large number of oscillators were analyzed by examining the resulting dynamics for the mean of the oscillator phases [20]. In contrast, the simplicity of our two oscillator system allows us to obtain the stationary probability density function for the full system both numerically and analytically. We show that the probability distribution of the oscillator phases has the single-hump shape only for weak coupling, whereas it deviates from this shape for strong coupling. We evaluate the coupling strength at which the transition between the two forms of the probability distribution occurs as a function of the noise intensity.

In Sect. 8.2, we introduce the Kuramoto model for excitable systems. Under the influence of

noise, the dynamics of the limit cycle oscillators are described by a stochastic differential equation (SDE), and we state the Fokker-Planck equation for the system. In Sect. 8.3, we consider a single active rotator driven by noise and derive its mean angular frequency from the stationary solution to the Fokker-Planck equation. We compare our analytical results with Monte-Carlo simulations of the corresponding SDE. In Sect. 8.4, we consider two coupled deterministic rotators and perform a bifurcation analysis of the system. We show that the system possesses a fixed point that is stable for small coupling strengths but looses its stability when the coupling is increased. For some range of the coupling strength, the stable fixed point and a stable limit cycle coexist. In Sect. 8.5, we consider two coupled active rotators under uncorrelated stochastic influences. In Sect. 8.5.1, we solve the Fokker-Planck equation of the system numerically and show that the shape of the probability distribution undergoes a characteristic change, corresponding to the transition from a synchronized to a desynchronized state, as coupling is increased. We evaluate the boundary between the synchronous and the asynchronous regime through a Fourier expansion approach in Sect. 8.5.2. A summary concludes the paper in Sect. 8.6.

8.2   Excitable Systems and the Kuramoto Model

Neurons can display a wide range of behavior to different stimuli and numerous models exist to describe neuronal dynamics. A common feature of both biological and model neurons is that sufficiently strong input causes them to fire periodically; the neuron displays oscillatory activity. For subthreshold inputs, on the other hand, the neuron is quiescent. When a subthreshold input is combined with a noisy input, however, the neuron will be pushed above threshold from time to time and fire spikes in a stochastic manner. In this regime, the neuron acts as an excitable element. In general, an excitable system possesses a stable equilibrium point from which it can temporarily depart by a large excursion through its phase space when it receives a stimulus of sufficient strength [22]. Besides neurons, chemical reactions, lasers, models of blood clotting, and cardiac tissues all display excitable dynamics [29–33]. Pulse propagation, spiral waves, spatial and temporal chaos, and synchronization have been studied in these systems [34–37].

The phase dynamics of an active rotator without interaction and random forces can be described

by the model developed by Kuramoto and coworkers [38, 39]:

$$\dot{\phi}(t) = \omega - a \sin \phi(t)\,. \tag{8.1}$$

To obtain the case of the excitable system with one stationary point, one chooses the parameter $a > \omega$. When we have n coupled identical oscillators, subject to stochastic influences, the model is described by the Langevin equation [23]

$$\dot{\phi}_i(t) = \omega - a \sin \phi_i(t) - \sum_{j=1}^{n} W_{ij}(\phi_j - \phi_i) + \eta_i(t)\,. \tag{8.2}$$

Here, we take the η_i to be uncorrelated Gaussian white noise, i.e., $\langle \eta_i(t_1)\eta_j(t_2) \rangle = 2\sigma\delta(t_1 - t_2)\delta_{ij}$. We will concentrate on the simplest case, namely that the coupling functions W_{ij} are sin-functions multiplied by a coupling constant w_{ij}, i.e., $W_{ij}(\phi) = w_{ij} \sin \phi$. Then, the dynamical evolution of the system's probability density function $P(\phi, t)$ is described by the Fokker-Planck equation

$$\frac{\partial}{\partial t} P(\phi, t) = -\sum_{i=1}^{n} \frac{\partial}{\partial \phi_i} \left[D_i(\phi) P(\phi, t) \right] + \sum_{i=1}^{n} \sum_{j=1}^{n} \frac{\partial^2}{\partial \phi_i \partial \phi_j} \left[D_{ij}(\phi) P(\phi, t) \right]\,, \tag{8.3}$$

where in our case the drift terms read

$$D_i(\phi) = \omega - a \sin \phi_i - \sum_{j=1}^{n} w_{ij} \sin(\phi_j - \phi_i) \tag{8.4}$$

and the diffusion terms are given by

$$D_{ij}(\phi) = \delta_{ij}\sigma\,. \tag{8.5}$$

Since the angle variables ϕ_i describe the phases of the oscillators, the probability density function must satisfy the periodic boundary conditions

$$P(\phi_1, \cdots, \phi_i = 0, \cdots, \phi_n, t) = P(\phi_1, \cdots, \phi_i = 2\pi, \cdots, \phi_n, t)\,, \qquad i = 1, \cdots, n\,. \tag{8.6}$$

Furthermore, the normalization condition for the probability density reads

$$\int_0^{2\pi} d\phi_1 \cdots \int_0^{2\pi} d\phi_n P(\boldsymbol{\phi}, t) = 1 \,. \tag{8.7}$$

8.3   Single-Rotator System

We first exam a single rotator subject to a noisy input and, following Ref. [40], calculate the mean frequency of oscillations as a function of the noise level. In this case, the Fokker-Planck equation (8.3) reads

$$\frac{\partial}{\partial t} P(\phi, t) = -\frac{\partial}{\partial \phi} \left[D(\phi) P(\phi, t) \right] + \sigma \frac{\partial^2}{\partial \phi^2} P(\phi, t) \,, \tag{8.8}$$

with

$$D(\phi) = \omega - a \sin \phi \,. \tag{8.9}$$

We can thus write the drift term as the negative gradient of a potential, $D = -\partial V / \partial \phi$, with the potential given by

$$V(\phi) = \omega \phi + a \cos \phi + c \,. \tag{8.10}$$

Introducing the probability current

$$S(\phi, t) = D(\phi) P(\phi, t) - \sigma \frac{\partial}{\partial \phi} P(\phi, t) \,, \tag{8.11}$$

the Fokker-Planck equation takes the form of a continuity equation,

$$\frac{\partial}{\partial t} P(\phi, t) + \frac{\partial}{\partial \phi} S(\phi, t) = 0 \,. \tag{8.12}$$

We now look for a stationary solution of the form $P(\phi, t) = P(\phi)$, $S(\phi, t) = S(\phi)$. In this case, we conclude from (8.12) that the derivative of the probability current with respect to ϕ must vanish,

and we have to solve

$$S = D(\phi)P(\phi) - \sigma \frac{\partial}{\partial \phi} P(\phi) \,. \tag{8.13}$$

The constant probability current S is related to the mean drift velocity, i.e., the mean angular frequency of the active rotator system according to $\bar{\omega} = 2\pi S$. The solution to the ordinary differential equation (8.13) is given by

$$P(\phi) = Ce^{-\frac{V(\phi)}{\sigma}} - \frac{S}{\sigma} \int_0^\phi d\phi' e^{\frac{V(\phi') - V(\phi)}{\sigma}} \,. \tag{8.14}$$

The integration constant in (8.10) can thus be absorbed into the constant C in (8.14), and the two free constants S and C are determined by the periodicity and normalization conditions (8.6) and (8.7). These two conditions can be written in matrix form as

$$\begin{pmatrix} \int_0^{2\pi} d\phi \, e^{-\frac{V(\phi)}{\sigma}} & \int_0^{2\pi} d\phi \int_0^\phi d\phi' e^{\frac{V(\phi') - V(\phi)}{\sigma}} \\ e^{-\frac{V(2\pi)}{\sigma}} - e^{-\frac{V(0)}{\sigma}} & \int_0^{2\pi} d\phi \, e^{\frac{V(\phi) - V(2\pi)}{\sigma}} \end{pmatrix} \begin{pmatrix} C \\ -\frac{S}{\sigma} \end{pmatrix} = \begin{pmatrix} 1 \\ 0 \end{pmatrix} \,. \tag{8.15}$$

Denoting the determinant of the 2×2 matrix in the last expression as $\det$, the constants C and S are given by

$$C = \frac{e^{-\frac{V(2\pi)}{\sigma}}}{\det} \int_0^{2\pi} d\phi \, e^{\frac{V(\phi)}{\sigma}} \,, \tag{8.16}$$

$$S = \frac{\sigma}{\det} \left[e^{-\frac{V(2\pi)}{\sigma}} - e^{-\frac{V(0)}{\sigma}} \right] \,. \tag{8.17}$$

Specializing to the potential of the active rotator (8.10), we obtain

$$\bar{\omega} = \frac{2\pi\sigma \left(1 - e^{-\frac{2\pi\omega}{\sigma}} \right)}{\int_0^{2\pi} d\phi' \, e^{-\frac{\omega}{\sigma}\phi'} \int_0^{2\pi} d\phi \, e^{\frac{a}{\sigma}[\cos(\phi+\phi') - \cos\phi]}} \,. \tag{8.18}$$

Note that in the limit $\sigma \to \infty$ the integrand in the denominator approaches one, and $\bar{\omega}$ converges to ω. To obtain the leading order behavior of $\bar{\omega}$ in the limit of small noise, we approximate the denominator using Laplace's method described in Ref. [41]. According to Laplace's method the

asymptotic behavior of the integral

$$I(x) = \int_a^b dt\, f(t) e^{xg(t)} \tag{8.19}$$

as $x \to \infty$ is given by

$$I(x) \sim \frac{\sqrt{2\pi} f(c) e^{xg(c)}}{\sqrt{-xg''(c)}} \ . \tag{8.20}$$

Here, it is assumed that $g(t)$ has a maximum at $t = c$ with $a \le c \le b$ and that $f(c) \ne 0$ and $g''(c) < 0$. We first apply Laplace's method to the inner integral in the denominator of (8.18), which we denote as $I(\sigma)$. The function $a[\cos(\phi + \phi') - \cos\phi]$ has a maximum inside the interval $0 \le \phi \le 2\pi$ at

$$\phi_0 = \pi + \arctan \frac{\sin\phi'}{1 - \cos\phi'} \ . \tag{8.21}$$

Using (8.20) we thus obtain for $\sigma \to 0$

$$I(\sigma) \sim \sqrt{\frac{2\pi\sigma}{a}} \int_0^{2\pi} d\phi' \, \frac{e^{\frac{a}{\sigma}[\cos(\phi_0 + \phi') - \cos\phi_0] - \frac{\omega}{\sigma}\phi'}}{\sqrt{\cos(\phi_0 + \phi') - \cos\phi_0}} \ . \tag{8.22}$$

The argument of the exponential function in the last identity can be simplified to

$$\frac{(a - \cos\phi')}{\sqrt{\sin^2 \frac{\phi'}{2}}} - \omega\phi' \ , \tag{8.23}$$

whose maximum within the interval $0 \le \phi' \le 2\pi$ is at

$$\phi'_0 = 2\arccos \frac{\omega}{a} \ . \tag{8.24}$$

Using this and applying (8.20) to the intermediate result (8.22), we obtain

$$I(\sigma) \sim \frac{2\pi\sigma}{\sqrt{a^2 - \omega^2}} e^{\frac{2}{\sigma}\left(\sqrt{a^2 - \omega^2} - \omega \arccos \frac{\omega}{a}\right)} \ , \qquad \sigma \to 0 \ . \tag{8.25}$$
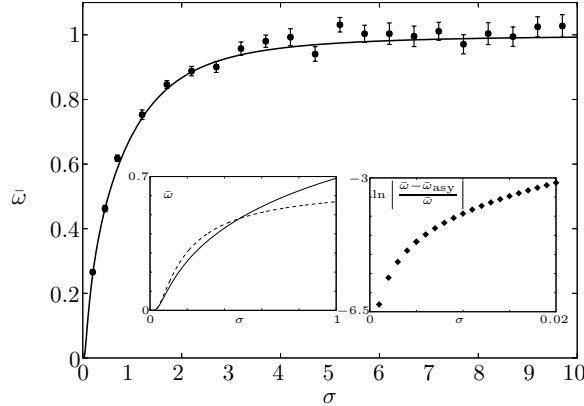
Figure 8.1: Average angular frequency of the single active rotator as a function of the noise intensity. The solid line shows the result (8.18). The dots represent results from Monte-Carlo simulations (mean ± standard error of the mean) of the Langevin equation (8.2). For each value of the noise intensity, forty runs where simulated up to $T = 400$. The first inset shows a comparison between the asymptotic expansion (8.26, dashed line) and numerical evaluations of the expression (8.18, solid lines) for small noise. The diamonds in the second inset show the logarithm of the relative deviation between the result (8.18) and its asymptotic approximation (8.26). Parameters are: $\omega = 1$, $a = 1.2$.

The leading asymptotic behavior of $\bar{\omega}$ as $\sigma \to 0$ is then given by

$$\bar{\omega}_{\mathrm{asy}} = \sqrt{a^2 - \omega^2}\, e^{-\frac{2}{\sigma}\left(\sqrt{a^2 - \omega^2} - \omega \arccos \frac{\omega}{a}\right)}\,. \tag{8.26}$$

Figure 8.1 shows the mean angular frequency $\bar{\omega}$ as a function of the noise level σ. The evaluation of

the analytical expression (8.18) yields results that are in good agreement with Monte-Carlo simula-

tions of the Langevin equation (8.2). Furthermore, the asymptotic expansion (8.26) is in excellent

agreement with numerical evaluations of (8.18) for small noise.

8.4   Deterministic Two-Rotator System

We next turn to a system of two coupled active rotators, where we first consider the deterministic

case, i.e, $\sigma = 0$. In particular, we are interested in rotators with repulsive coupling, i.e., we consider

the case w_{12}, $w_{21} > 0$. Introducing the center of mass and difference coordinates $\Phi = (\phi_1 + \phi_2)/2$

and $\Delta = (\phi_1 - \phi_2)/2$, the set of equations (8.2) takes the form

$$\dot{\Phi}(t) = \omega - a\sin\Phi(t)\cos\Delta(t) + (w_{12} - w_{21})\sin\Delta(t)\cos\Delta(t),$$

$$\dot{\Delta}(t) = -a\cos\Phi(t)\sin\Delta(t) + (w_{12} + w_{21})\sin\Delta(t)\cos\Delta(t). \tag{8.27}$$

The system has a trivial stationary point at $\Phi(t) = \Phi_0 = \sin^{-1}(\omega/a)$, $\Delta(t) = 0$, whose stability we analyze by linearizing the system (8.27). Writing $\Phi(t) = \Phi_0 + \epsilon_\Phi(t)$, $\Delta(t) = \epsilon_\Delta(t)$ we obtain to first order

$$\frac{d}{dt}\begin{pmatrix} \epsilon_\Phi(t) \\ \epsilon_\Delta(t) \end{pmatrix} = \begin{pmatrix} -\sqrt{a^2 - \omega^2} & w_{12} - w_{21} \\ 0 & w_{12} + w_{21} - \sqrt{a^2 - \omega^2} \end{pmatrix}\begin{pmatrix} \epsilon_\Phi(t) \\ \epsilon_\Delta(t) \end{pmatrix}. \tag{8.28}$$

The real parts of the eigenvalues of the 2×2 matrix on the right-hand side of the last identity determine the stability of the fixed point $(\Phi_0, 0)$. Under the assumption $a > \omega$ the first eigenvalue $\lambda_1 = -\sqrt{a^2 - \omega^2}$ is always real and negative. The second eigenvalue $\lambda_2 = w_{12} + w_{21} - \sqrt{a^2 - \omega^2}$ is also always real; for small coupling it is negative, but when the sum of the coupling strengths $w_{12} + w_{21}$ increases it becomes positive and the fixed point $(\Phi_0, 0)$ looses its stability in, as it turns out, a subcritical pitchfork bifurcation. Further fixed points of the system can be determined and turn out to be unstable for all values of the coupling strengths. In the case $w_{12} = w_{21} = w$ they are given by

$$\Phi_1 = \frac{1}{2}\sin^{-1}\left(\frac{4\omega w}{a^2}\right), \quad \Delta_1 = \cos^{-1}\left(\frac{\omega}{a\sin\Phi_1}\right). \tag{8.29}$$

Figure 8.2(a) shows a bifurcation diagram of the system. For small coupling strength, the system does not display oscillatory behavior. When the coupling strength is increased above a critical value, a stable limit cycle emerges from a homoclinic orbit. For a small range of coupling strengths, the stable fixed point coexists with the stable limit cycle. In this case, it depends on the initial conditions whether the system will converge toward the fixed point $(\Phi_0, 0)$ or the limit cycle. Figure 8.2(b) shows the attractors for fixed point and limit cycle dynamics in the (Φ, Δ)-plane for $w_{12} = w_{21} = 0.308$. In the strong-coupling limit, the minimum and maximum of Δ in Fig. 8.2(a) both converge
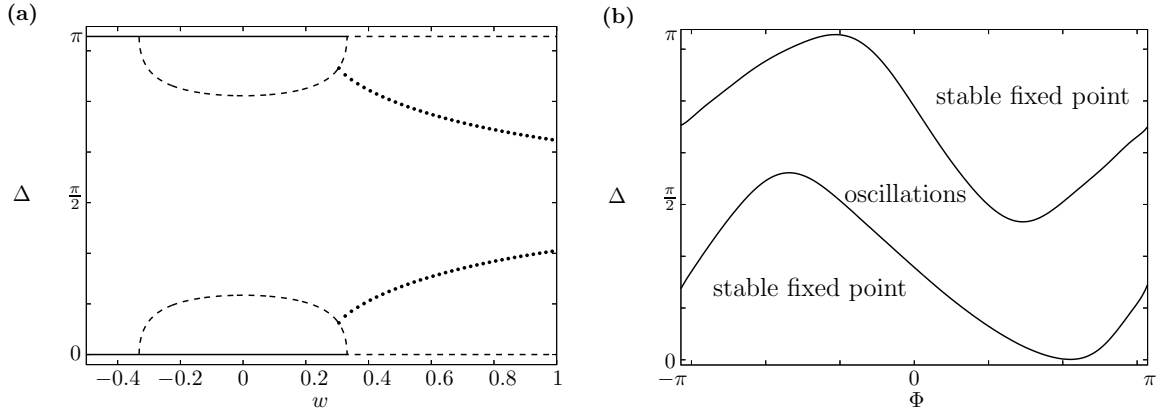
(a)

(b)

Figure 8.2: Stable and unstable fixed points and oscillations in the deterministic two-rotator system. **(a)** shows the bifurcation diagram with stable (solid lines) and unstable (dashed lines) fixed points of the system (8.27) for the choice of parameters $\omega = 1$, $a = 1.2$, $w_{12} = w_{21} = w$. Dots indicate the minimum and maximum values of oscillations in the value of Δ that result for the initial conditions $\Phi = 0$, $\Delta = \pi/2$. **(b)** depicts for $w = 0.308$ the boundaries between the regions in the space of initial conditions for which the system converges to the limit cycle or the stable fixed point.

toward $\pi/2$. Thus, the system approaches antisynchronous oscillatory dynamics, where ϕ_1 and ϕ_2 are phase shifted by π while their sum increases constantly.

8.5 Stochastic Two-Rotator System

We now consider the coupled two-rotator system in the case where both rotators receive uncorrelated stochastic driving. The temporal evolution of the probability density of this system is given by the Fokker-Planck equation (8.3) with the drift and diffusion coefficients (8.4) and (8.5).

8.5.1 Numerical Results

First, we investigate the stationary solution to the Fokker-Planck equation numerically. To this end, we numerically solve the partial differential equation (8.3) under the periodic boundary conditions (8.6) for the homogeneous initial condition $P(\phi_1, \phi_2, t = 0) = 1/4\pi^2$ and observe that the solution converges to the stationary solution after some time. Figure 8.3 shows the stationary solution in the coordinates Φ and Δ for two different values of the coupling strength. We find that, depending on the strength of the noise and coupling, two different characteristic forms of the stationary solution exist. In the case shown in Fig. 8.3(a) the probability density is peaked around the stable fixed point
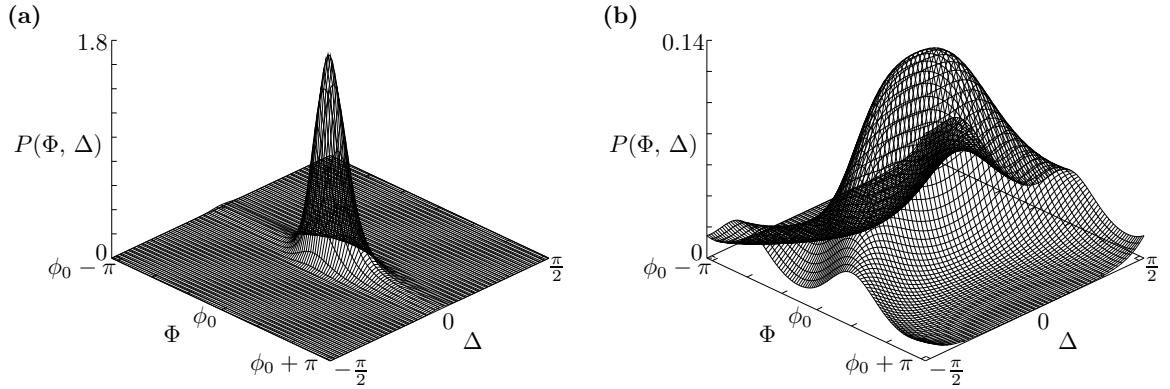
(a)

(b)

Figure 8.3: Synchronized and desynchronized modes in the stochastic two-rotator system. The stationary solution to the Fokker-Planck equation (8.3) is shown for different values of the coupling strength. In both **(a)** and **(b)**, we have $w_{12} = w_{21} = w$ and $\omega = 1$, $a = 1.2$, $\sigma = 0.4$. In **(a)** the coupling strength is $w = 0.3$ and the rotators are in a synchronized state; in **(b)** the coupling is increased to $w = 0.4$ and the two rotators desynchronize.

of the deterministic two-rotator system $(\Phi_0, 0)$. In Fig. 8.3(b), the peak at the fixed point $(\Phi_0, 0)$ is much less pronounced. Furthermore, if we consider the probability distribution for $\Delta = \pm\pi/2$, i.e., at the edge of the region shown in Fig. 8.3, we see that the probability distribution is not given by one central hump anymore. In order to distinguish between the two different scenarios in a quantitative way, we consider the marginal stationary probability density

$$\bar{P}(\Delta) = \int_{\Phi_0-\pi}^{\Phi_0+\pi} d\Phi P(\Phi, \Delta) \,. \tag{8.30}$$

Figure 8.4 shows this quantity for one level of the noise intensity σ and for different coupling strengths. For weak coupling, $\bar{P}(\Delta)$ has a pronounced maximum at $\Delta = 0$. For increasing coupling strengths, this maximum decreases and eventually turns into a minimum. We can thus classify the system dynamics as synchronized or desynchronized according to the sign of the second derivative of $\bar{P}(\Delta)$ at the origin and can label the σ-w plane accordingly. In the next section, we calculate the phase boundary between the synchronized and desynchronized regime through a Fourier expansion approach.
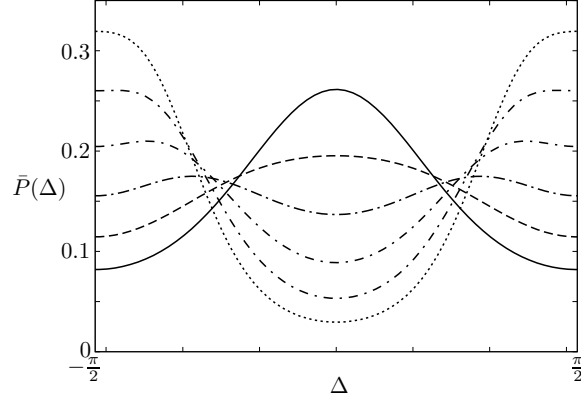
Figure 8.4: Marginal probability density for different values of the coupling strength $w = w_{12} = w_{21}$. The coupling strength for the curve with the highest value at $\Delta = 0$ (solid line) is $w = 0.1$ and increases from curve to curve in increments of $\delta w = 0.2$ to the maximum value $w = 1.1$ (dotted line). Other parameters are: $\omega = 1$, $\sigma = 0.4$, $a = 1.2$.

8.5.2 Fourier Expansion Results

The probability density $P(\phi_1, \phi_2)$ is periodic in ϕ_1 and ϕ_2, so we expand it as

$$P(\phi_1, \phi_2) = \sum_{k_1,k_2} C(k_1, k_2) e^{i(k_1\phi_1 + k_2\phi_2)} . \tag{8.31}$$

Inserting this approach into the right-hand side of (8.3) yields together with (8.4) and (8.5)

$$\begin{aligned}
0 &= \sum_{k_1,k_2} C(k_1, k_2) e^{i(k_1\phi_1 + k_2\phi_2)} \Big\{ a(\cos\phi_1 + \cos\phi_2) - (w_{12} + w_{21}) \cos(\phi_2 - \phi_1) \\
&\quad - ik_1[\omega - a\sin\phi_1 - w_{12}\sin(\phi_2 - \phi_1)] - ik_2[\omega - a\sin\phi_2 - w_{21}\sin(\phi_1 - \phi_2)] - \sigma k_1^2 - \sigma k_2^2 \Big\} .
\end{aligned} \tag{8.32}$$

The term inside the curly brackets on the right-hand-side of the last identity is itself periodic in ϕ_1 and ϕ_2 and can also be expanded as a Fourier series

$$\big\{ \cdots \big\} = \sum_{|l_1| \le 1, |l_2| \le 1} \tilde{C}(l_1, k_1, l_2, k_2) e^{i(l_1\phi_1 + l_2\phi_2)} . \tag{8.33}$$

Here, the coefficients $\tilde{C}(l_1, l_2)$ read

$$\tilde{C}(0, k_1, 0, k_2) = -i\omega(k_1 + k_2) - \sigma(k_1^2 + \sigma k_2^2) ,$$

$$\tilde{C}(\pm 1, k_1, 0, k_2) = \frac{a}{2}(1 \pm k_1) \,,$$

$$\tilde{C}(0, k_1, \pm 1, k_2) = \frac{a}{2}(1 \pm k_2) \,,$$

$$\tilde{C}(1, k_1, -1, k_2) = -\frac{1+k_1}{2}w_{12} - \frac{1-k_2}{2}w_{21} \,,$$

$$\tilde{C}(-1, k_1, 1, k_2) = -\frac{1-k_1}{2}w_{12} - \frac{1+k_2}{2}w_{21} \,,$$

$$\tilde{C}(\pm 1, k_1, \pm 1, k_2) = 0 \,. \tag{8.34}$$

We can then rewrite (8.32) as

$$0 = \sum_{k_1, k_2} e^{i(k_1\phi_1 + k_2\phi_2)} \sum_{|l_1|<1, |l_2|<1} C(k_1 - l_1, k_2 - l_2)\tilde{C}(l_1, k_1 - l_1, l_2, k_2 - l_2) \,. \tag{8.35}$$

Setting the inner sum to zero, we obtain an infinite system of algebraic equations. In order to obtain the Nth Fourier order approximation we truncate the outer sum such that we set $C_N(k_1, k_2) = 0$ for $|k_1| > N$ or $|k_2| > N$. Then, we have to solve a system of $(2N+1)^2 - 1$ algebraic equations in order to obtain the expansion coefficients to Nth order $C_N(k_1, k_2)$, where the additional index N indicates the approximation order. Finally, the coefficient $C_N(0, 0)$ is determined from the normalization condition as $C_N(0, 0) = 1/4\pi^2$.

As an illustrative example we now consider the first order in the Fourier expansion for the case $w_{12} = w_{21} = w$. The system of algebraic equations we need to solve then reads

$$a[C_1(0, -1) + C_1(-1, 0)] - 4(\sigma - i\omega)C_1(-1, -1) = 0 \,,$$

$$4\pi^2[2(\sigma - i\omega)C_1(-1, 0) + wC_1(0, -1)] = a \,,$$

$$2\pi^2\{a[C_1(-1, 0) + C_1(0, 1)] - 4\sigma C_1(-1, 1)\} = w \,,$$

$$4\pi^2[wC_1(-1, 0) + 2(\sigma - i\omega)C_1(0, -1)] = a \,,$$

$$4\pi^2[2(\sigma + i\omega)C_1(0, 1) + wC_1(1, 0)] = a \,,$$

$$2\pi^2\{a[C_1(0, -1) + C_1(1, 0)] - 4\sigma C_1(1, -1)]\} = w \,,$$

$$4\pi^2[2(\sigma + i\omega)C_1(1, 0) + wC_1(0, 1)] = a \,,$$

$$a[C_1(0, 1) + C_1(1, 0)] - 4(\sigma + i\omega)C_1(1, 1) = 0 \,. \tag{8.36}$$

From this we obtain the first order approximation

$$P_1(\phi_1, \phi_2) = \frac{1}{4\pi^2} + \alpha\{2a\beta\gamma\sigma(\cos\phi_1 + \cos\phi_2) + 4a\beta\sigma\omega(\sin\phi_1 + \sin\phi_2) + (a^2\gamma\sigma^2 - 2a^2\sigma\omega^2)$$

$$\times\cos(\phi_1 + \phi_2) + [a^2\beta\gamma - w\beta(\gamma^2 + 4\omega^2)]\cos(\phi_1 - \phi_2) + a^2\sigma(w\omega + 4\sigma\omega)\sin(\phi_1 + \phi_2)\}, \quad (8.37)$$

with the abbreviations

$$\alpha = \frac{1}{4\pi^2\sigma\beta(\gamma^2 + 4\omega^2)}, \qquad \beta = \sigma^2 + \omega^2, \qquad \gamma = w + 2\sigma. \tag{8.38}$$

Substituting the coordinates ϕ_1 and ϕ_2 according to $\phi_1 = \Phi + \Delta$ and $\phi_2 = \Phi - \Delta$ and integrating with respect to Φ we obtain the marginal probability density

$$\bar{P}_1(\Delta) = \frac{1}{2\pi} + 2\pi\alpha\beta(a^2\gamma - w\gamma^2 - 4w\omega^2)\cos(2\Delta). \tag{8.39}$$

Setting its second derivative to zero, we obtain the equation

$$a^2(w + 2\sigma) - w[(w + 2\sigma)^2 + 4\omega^2] = 0, \tag{8.40}$$

which we can solve in w or in σ. Eventually, we want to obtain w as a function of σ. However, since we have a cubic equation in w and only a quadratic equation in σ, for convenience we express σ as a function of ω:

$$\sigma = \frac{a^2 - 2w^2 \pm \sqrt{a^4 - 16w^2\omega^2}}{4w}. \tag{8.41}$$

This procedure can easily be generalized to higher orders. Figure 8.5 shows the resulting phase diagram obtained from solving the Fokker-Planck equation numerically and from the Fourier expansion. The accuracy of the Fourier expansion results improves with increasing strength of the noise. This can be seen, for instance, in the second inset of Fig. 8.5, where even the first expansion order yields very accurate results for strong noise. In general, even relatively low orders in the expansion give a good estimate for the phase boundary for a wide range of noise strengths, as can be seen from the results for the fourth expansion order in Fig. 8.5. However, for very small noise levels
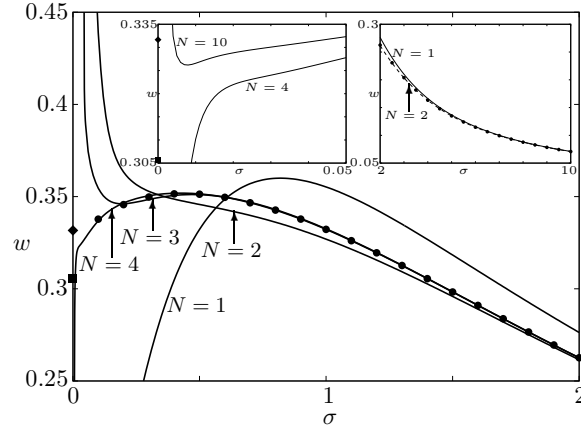
Figure 8.5: Regimes of synchronized and desynchronized dynamics. The phase boundary between the synchronized and desynchronized regimes is shown as a function of the noise strength σ. Areas below the curves correspond to the synchronized, areas above the curve to the desynchronized regime. The solid lines show the results of the first four Fourier orders, the dots represent numerical results. The diamond represents the coupling strengths for which the fixed point $(\Phi_0, 0)$ of the deterministic system becomes unstable; the square indicates the value of w at which the stable limit cycle is first observed. The insets show results for small and for large noise. In the first inset (small noise) the results from the fourth and tenth Fourier orders are shown. The second inset (large noise) shows the results from the first (solid line) and second (dashed line) Fourier orders. Parameters are $\omega = 1$, $a = 1.2$.

the Fourier expansion diverges, as is exemplified in the first inset in Fig. 8.5 for the fourth and tenth expansion orders. Considering the first inset in Fig. 8.5, we conclude that in the limit $\sigma \to 0$ the results from the Fourier expansion approach a value of the coupling strength for which the stable fixed point coexists with the limit cycle in the deterministic system. Therefore, neither the existence of the stable limit cycle nor the stability of the fixed point can be used exclusively to determine the zero-noise limit of the phase transition between the synchronized and desynchronized states. Strong noise has a desynchronizing effect on the system, as the minimal coupling for desynchronization vanishes in the limit of $\sigma \to \infty$. If the noise is weak, however, it stabilizes the synchronized state, as is indicated by the initially upward slope of the phase boundary in Fig. 8.5. In conclusion, the synchronized state of the system is most stable for intermediate noise.

8.6 Summary

We have investigated the transition from synchronized to desynchronized behavior in a system of two-coupled active rotators under stochastic influences. The two regimes are distinguished by the

sign of the second derivative of the marginal probability density at vanishing phase difference. We have evaluated the phase boundary between the two states in the (coupling strength) - (noise intensity) plane. We have shown that the synchronized state is most stable, in the sense that the coupling strength required to desynchronize the system is maximal for nonvanishing noise intensity.

8.7   Acknowledgments

References

[1] J. F. Heagy, T. L. Carroll, and L. M. Pecora, Phys. Rev. E **50**, 1874 (1994) and references therein.

[2] R. Roy and K. S. Thornburg, Jr., Phys. Rev. Lett. **72**, 2009 (1994).

[3] A.V. Ustinov, M. Cirillo, and B. Malomed, Phys. Rev. B **47**, 8357 (1993).

[4] K. Wiesenfeld, P. Colet, and S. H. Strogatz, Phys. Rev. Lett. **76**, 404 (1996).

[5] D. Amit, *Modelling Brain Function* (Cambridge University Press, Cambridge, UK, 1989); J. Hertz, A. Krogh, and R. Palmer, *Introduction to the Theory of Neural Computation* (Addison-Wesley, Redwood City, 1991).

[6] Y. Soen, N. Cohen, D. Lipson, and E. Braun, Phys. Rev. Lett. **82**, 3556 (1999).

[7] A. Pikovsky, M. Rosenblum, and J. Kurths, *Synchronization: a universal concept in nonlinear sciences* (Cambridge Univ. Press, Cambridge, 2003).

[8] S. Strogatz, *Sync: The Emerging Science of Spontaneous Order* (Hyperion, New York, 2003).

[9] T. Shinbrot and F. J. Muzzio, Nature (London) **410**, 251 (2001).

[10] S. F. Brandt, B. K. Dellen, and R. Wessel, Phys. Rev. Lett. **96**, 034104 (2006).

[11] R. Chaccón and P. J. Martínez, Phys. Rev. Lett. **98**, 224102 (2007).

[12] M. A. Zaks, A. B. Neiman, S. Feistel, and L. Schimansky-Geier, Phys. Rev. E **68**, 066206 (2003).

[13] J. A. White, J. T. Rubinstein, and A. R. Kay, Trends Neurosci. **23**, 131 (2000).

[14] L. Gammaitoni, P. Hänggi, P. Jung, and F. Marchesoni, Rev. Mod. Phys. **70**, 223 (1998).

[15] W. H. Calvin and C. F. Stevens, J. Neurophysiol. **31**, 574 (1968).

[16] J. K. Douglass, L. Wilkens, E. Pantazelou, and F. Moss, Nature **365**, 337 (1993).

[17] K. Wiesenfeld and F. Moss, Nature **373**, 33 (1995).

[18] H. Treutlein and K. Schulten, Ber. Bunsenges. Phys. Chem. **89**, 710 (1985).

[19] C. Kurrer and K. Schulten, Physica D **50**, 311 (1991).

[20] C. Kurrer and K. Schulten, Phys. Rev. E **51**, 6213 (1995).

[21] C. Kurrer and K. Schulten, Int. J. Neural Syst. **7**, 399 (1996).

[22] M. A. Zaks, X. Sailer, L. Schimansky-Geier, and A. B. Neiman, Chaos **15**, 026117 (2005).

[23] B. Lindner, J. García-Ojalvo, A. Neiman, and L. Schminasky-Geier, Phys. Rep. **392**, 321 (2004).

[24] J. Milton, *Dynamics of Small Neural Populations* (Amer. Math. Soc., Providence, 1996).

[25] S. F. Brandt, A. Pelster, and R. Wessel, Phys. Rev. E **74**, 036201 (2006).

[26] S. F. Brandt, A. Pelster, and R. Wessel, Europhys. Lett. **79**, 38001 (2007).

[27] M. Rabinovich, A. Selverston, L. Rubchinsky, and R. Huerta, Chaos **6**, 288 (1996).

[28] N. G. van Kampen, *Stochastic Processes in Physics and Chemistry*, 2nd ed. (North Holland, Amsterdam, 1992).

[29] T. Sakurai, E. Mihaliuk, F. Chirila, and K. Showalter, Science **14**, 296 (2002).

[30] H. J. Wünsche, O. Brox, M. Radziunas, and F. Henneberger, Phys. Rev. Lett. **88**, 023901 (2001).

[31] E. S. Lobanova, E. E. Shnol, and F. I. Ataullakhanov, Phys. Rev. E **70**, 032903 (2004).

[32] A. V. Panfilov, S. C. Mller, V. S. Zykov, and J. P. Keener, Phys. Rev. E **61**, 4644 (2000).

[33] C. Koch, *Biophysics of Computation: Information Processing in Single Neurons* (Oxford University Press, New York, 1999).

[34] J. D. Murray, *Mathematical Biology*, 2nd ed. (Springer, New York, 1993).

[35] A. S. Mikhailov, *Foundations of Synergetics I*, 2nd ed. (Springer-Verlag, Berlin 1994).

[36] T. R. Chay and J. Rinzel, Biophys. J. **47**, 357 (1985).

[37] B. Hu and C. Zhou, Phys. Rev. E **63**, 026201 (2001).

[38] S. Shinomoto and Y. Kuramoto, Prog. Theor. Phys. **75**, 1105 (1986).

[39] H. Sakaguchi, S. Shinomoto, and Y. Kuramoto, Prog. Theor. Phys. **79**, 600 (1988).

[40] H. Risken, *The Fokker-Planck Equation. Methods of Solution and Applications* (Springer-Verlag, Berlin, 1984).

[41] C. M. Bender and S. A. Orszag, *Advanced Mathematical Methods for Scientists and Engineers* (Springer, New York, 1999).

Chapter 9

Synchronization from disordered driving forces in arrays of coupled oscillators

The effects of disorder in external forces on the dynamical behavior of coupled nonlinear oscillator networks are studied. When driven synchronously, i.e., all driving forces have the same phase, the networks display chaotic dynamics. We show that random phases in the driving forces result in regular, periodic network behavior. Intermediate phase disorder can produce network synchrony. Specifically, there is an optimal amount of phase disorder, which can induce the highest level of synchrony. These results demonstrate that the spatiotemporal structure of external influences can control chaos and lead to synchronization in nonlinear systems.

Networks of coupled nonlinear oscillators provide useful model systems for the study of a variety of phenomena in physics and biology [1]. Among many others, examples from physics include solid state lasers [2] and coupled Josephson junctions [3, 4]. In biology, the central nervous system can be described as a complex network of oscillators [5], and cultured networks of heart cells are examples of biological structures with strong nearest-neighbor coupling [6]. In particular, the emergence of synchrony in such networks [7, 8] and the control of chaos in nonlinear systems [9–11] have received increased attention in recent years.

Disorder and noise in physical systems usually tend to destroy spatial and temporal regularity. However, in nonlinear systems, often the opposite effect is found and intrinsically disordered processes, such as thermal fluctuations or mechanically randomized scattering, lead to surprisingly ordered patterns [12]. For instance, in the phenomenon of stochastic resonance the presence of noise can improve the ability of a system to transfer information reliably [13]. Some time ago, Braiman et al. studied one- (1D) and two-dimensional (2D) coupled arrays of forced, damped, nonlinear pendula [14]. They found that when a certain amount of disorder was introduced by randomizing the lengths of the pendula the dynamics of the array ceased to be chaotic. Instead, they observed complex, yet regular, spatiotemporal patterns. Further studies of the same system showed that chaos in the array of oscillators can also be tamed by impurities [15] and that random shortcuts between the pendula lead to synchronization of the array [16].

Here, we introduce disorder by modifying the driving forces of the oscillators through phase differences. We observe the emergence of regular, phase-locked dynamics. Moreover, for intermediate spreads of the phase angles in the driving forces, we find that the oscillations become largely synchronous.

We focus our numerical analysis on arrays of forced, damped, nonlinear pendula. The 1D array (chain) is described by the equation of motion

$$ml^2\ddot{\theta}_n + \gamma\dot{\theta}_n = -mgl\sin\theta_n + \tau' + \tau\sin\left(\omega t + \varphi_n\right) + \kappa\left(\theta_{n+1} + \theta_{n-1} - 2\theta_n\right), \qquad (9.1)$$

$$n = 1, 2, \ldots N\,.$$

In order to consider a 2D lattice, we introduce an additional index, $\theta_n \to \theta_{n,m}$, n, $m = 1, 2, \ldots N$ and modify the coupling term accordingly: $\kappa(\theta_{n+1}+\theta_{n-1}-2\theta_n) \to \kappa(\theta_{n+1,m}+\theta_{n-1,m}+\theta_{n,m+1}+\theta_{n,m-1} - 4\theta_{n,m})$. For both the 1D and 2D case, we choose free boundary conditions, i.e., $\theta_0 = \theta_1$, $\theta_N = \theta_{N+1}$ and $\theta_{0,m} = \theta_{1,m}$, $\theta_{N,m} = \theta_{N+1,m}$, $\theta_{n,0} = \theta_{n,1}$, $\theta_{n,N} = \theta_{n,N+1}$, respectively. The parameter values used are the same as in previous studies [14–16]: The mass of the pendulum bob is $m = 1$, the length $l = 1$, the acceleration due to gravity $g = 1$, the damping $\gamma = 0.75$, the d.c. torque $\tau' = 0.7155$, the a.c. torque $\tau = 0.4$, the angular frequency $\omega = 0.25$, and the coupling strength $\kappa = 0.5$. For this choice of parameter values, each isolated pendulum displays chaotic behavior characterized by a positive Lyapunov exponent [14].
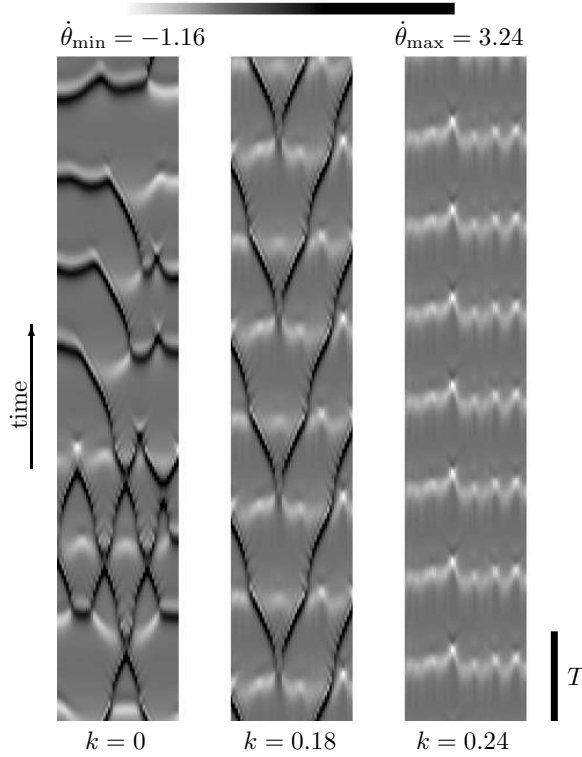
Figure 9.1: Spatiotemporal angular velocity plots for chaotic and regular dynamics in an array of $N = 50$ coupled oscillators. The chain of pendula is shown from left to right. Time increases continuously from bottom to top. Grayscales indicate the angular velocities of the oscillators. Light gray shades represent negative, dark tones positive velocities.

A particularly easy and intuitive way to visualize the global spatiotemporal behavior of a chain (or lattice) of oscillators is to consider the average velocity

$$\sigma(jT) = \frac{1}{N} \sum_{n=1}^{N} \dot{\theta}_n(jT) \tag{9.2}$$

at times that are integer multiples of the forcing period $T = 2\pi/\omega$ [15]. Considering this measure for an isolated pendulum, Gavrielides et al. performed a bifurcation analysis with respect to the pendulum length l and found that an uncoupled pendulum is chaotic for values $l = 1 \pm 0.002$ [17]. If the length of an isolated pendulum is increased to $l > 1.002$, it performs a 'libration,' in which the combined d.c. and a.c. torque are insufficient to overcome the pendulum's increased rotational inertia. On the other hand, if the pendulum's length is decreased to $l < 0.998$, the pendulum performs a 'rotation,' an overturning motion where the torques combine to rotate the pendulum over the top.
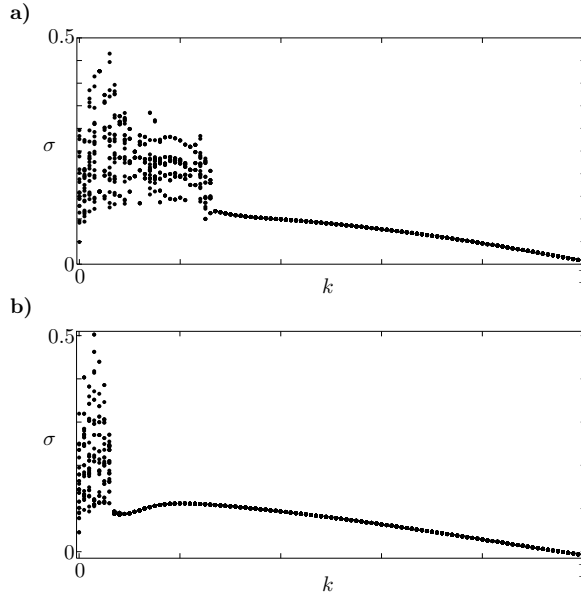
Figure 9.2: Chaotic and regular dynamics as a function of the degree of disorder. The average angular velocity at $t = 60T$, $61T$, ..., $80T$ is shown for each value of the disorder parameter k. **(a)** 1D array of $N = 50$ oscillators. **(b)** 2D lattice of 16×16 oscillators.

In our study, we do not alter any parameters that would affect the dynamics of an isolated pendulum and keep the coupling strength at its default value. Instead, we introduce disorder by randomly varying the phase angles φ_n of the driving forces in Eq. (9.1). In the case where $\varphi_n = 0$ for all driving forces, we observe chaotic dynamics in the array (Fig. 9.1) in agreement with previous studies [14]. However, when we disorder the driving forces by randomly choosing the phase angles φ_n uniformly from the interval $[-k\pi, +k\pi]$, we observe that for sufficiently large k the oscillations become regular.

Figure 9.2 shows the average angular velocity $\sigma(t)$ at $t = 60T$, $61T$, ..., $80T$ for a 1D array of $N = 50$ and a 2D lattice of 16×16 oscillators. The presence of chaos for small disorder in both the 1D and 2D array becomes manifest in a dispersed distribution of the average velocities $\sigma(60T)$, $\sigma(61T)$, ..., $\sigma(80T)$. For larger disorder, however, we observe periodic patterns in the form of $1T$-, $2T$-, $3T$-, ... 'attractors,' where the average velocity of the oscillator array repeats its value after 1, 2, 3, ... forcing periods. Ultimately, as k is increased further, a $1T$ periodic pattern is reached.

In general, the value of k for which a transition from chaotic to regular dynamics first occurs depends on the particular distribution of the random phases. We thus consider the average over
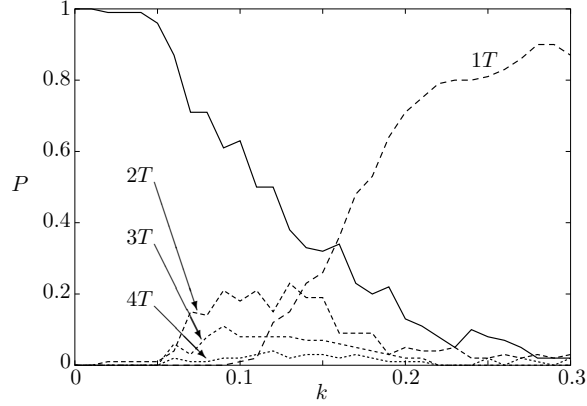
Figure 9.3: Probability P of chaotic dynamics (solid line) and different forms of regular behavior (dashed lines) vs. the disorder parameter k in an array of $N = 50$ coupled oscillators. The probabilities were determined by averaging over 100 different samplings of the phases φ_n.

several different samplings of uniform distributions in order to analyze the occurrence of different forms of periodic behavior. Figure 9.3 shows the probability for a 1D array to have reached a $1T$-, $2T$-, $3T$-, or $4T$-attractor after $t = 60T$ as a function of the disorder parameter k. For very small disorder, i.e., $k < 0.02$, we observe only chaotic dynamics, but as k passes this threshold, the first periodic patterns start to appear. For $k \geq 0.1$, we observe that $1T$-, $2T$-, $3T$-, $4T$-, ... attractors coexist with chaotic behavior. For $0.02 \leq k \leq 0.13$ the $2T$-attractor is the dominant form of dynamics if an attractor has been reached. For $k > 0.28$, the array undergoes regular oscillations with period $1T$ in the vast majority of cases.

Furthermore, in addition to the transition from chaotic to regular behavior, we observe that the oscillations become largely synchronous, i.e., the phases of the oscillations not only lock but tend to assume equal values, for intermediate values of k. In order to quantify the presence of synchrony in the array, we consider the averaged cross correlation

$$C = \frac{2}{N(N-1)} \sum_{i<j} c_{ij} \,, \tag{9.3}$$

where c_{ij} denotes the correlation between the ith and jth oscillator:

$$c_{ij} = \frac{\int_{T_0}^{T_0+T} dt \, \dot{\theta}_i(t) \dot{\theta}_j(t)}{\left[\int_{T_0}^{T_0+T} dt \, \dot{\theta}_i^2(t) \int_{T_0}^{T_0+T} dt \, \dot{\theta}_j^2(t) \right]^{1/2}} \,. \tag{9.4}$$
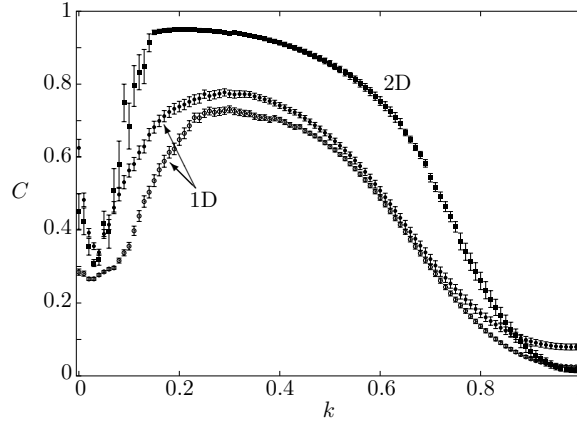
Figure 9.4: Synchronization in 1D (dots) and 2D (squares) arrays of oscillators vs. the disorder parameter k. Error bars show one standard error of the mean. Filled dots correspond to $N = 16$, open dots to $N = 50$. Averaging was performed over 200 (1D) and 10 (2D) different samplings of the phases φ_n.

Figure 9.4 shows C as a function of k for two 1D and one 2D arrays. Disordering the driving forces results in less synchronized oscillations of the array if the disorder parameter is very small. The minimum of synchrony is reached for $k \approx 0.03$. Note that the location of this minimum corresponds approximately to the first appearance of regular dynamics in Fig. 9.3. When the external forces are disordered further, synchronization in the array increases and reaches a peak value for intermediate disorder. In the 1D case, the maximum is reached for $k \approx 0.3$ and its value is $C_{\max} \approx 0.72$ for $N = 50$ and $C_{\max} \approx 0.78$ for $N = 16$ oscillators. In the case of the 2D array, the synchronization is even stronger. Here, the peak value of $C_{\max} \approx 0.95$ is reached for $k \approx 0.2$. We attribute the stronger synchronization in the 2D array to the fact that the number of couplings per oscillator is higher than in the 1D case. Furthermore, smaller arrays show a higher degree of averaged cross correlation than larger arrays. This is because oscillators that are nearest neighbors show the highest degree of synchronization, and the ratio of cross-correlation coefficients obtained from direct neighbors to all cross-correlation coefficients contributing to the averaged cross correlation C decreases with increasing size of the array like $\mathcal{O}(1/N)$.

To summarize, we have shown that disorder leads to transitions from chaotic to regular behavior in arrays of coupled oscillators when disorder is introduced in the phases of the driving forces [18]. In this investigation, each pendulum was in a regime where it behaves chaotically when uncoupled, in contrast to previous studies in which parameters were altered that affect the dynamics of an

isolated oscillator [14, 15]. In particular, Braiman et al. introduced disorder by randomly varying the lengths of the pendula [14]. Since an isolated pendulum only behaves chaotically when its length lies within a narrow range, only 2% of the oscillators remained in their chaotic regime in this approach, and the transition from chaotic to regular spatiotemporal patterns reported in Ref. [14] can be attributed to the dominance of the majority of regular pendula over the few remaining chaotic ones [15]. Our results show that disorder in the model system described by Eq. (9.1) results in regular dynamics of the array even if all individual elements are chaotic. Moreover, we find that for intermediate disorder, the oscillations show a high degree of synchronization.

Stimulus-induced synchronization of neural activity in central nervous systems has intrigued neuroscientists for decades [19, 20]. Furthermore, in many applications, such as in coupled Josephson junctions, or in the case of atrial or ventricular fibrillation, one seeks to restore periodic or steady-state behavior from chaos. It is in regard to these day-to-day circumstances that control and synchronization of chaotic dynamics have become one of the central topics of nonlinear science [21, 22]. In most situations the components of a system themselves cannot be altered, so it is desirable to establish methods by which chaos can be tamed without changing parameters intrinsic to the system. We thus believe that our proposed mechanism of controlling chaos via external forces has potential applications in these fields.

References

[1] J. F. Heagy, T. L. Carroll, and L. M. Pecora, Phys. Rev. E **50**, 1874 (1994) and references therein.

[2] R. Roy and K. S. Thornburg, Jr., Phys. Rev. Lett. **72**, 2009 (1994).

[3] A. V. Ustinov, M. Cirillo, and B. Malomed, Phys. Rev. B **47**, 8357 (1993).

[4] K. Wiesenfeld, P. Colet, and S. H. Strogatz, Phys. Rev. Lett. **76**, 404 (1996).

[5] D. Amit, *Modelling Brain Function* (Cambridge Univ. Press, Cambridge, UK, 1989); J. Hertz, A. Krogh, and R. Palmer, *Introduction to the Theory of Neural Computation* (Addison-Wesley, Redwood City, 1991).

[6] Y. Soen, N. Cohen, D. Lipson, and E. Braun, Phys. Rev. Lett. **82**, 3556 (1999).

[7] A. Pikovsky, M. Rosenblum, and J. Kurths, *Synchronization: A Universal Concept in Nonlinear Sciences* (Cambridge Univ. Press, Cambridge, 2003).

[8] S. Strogatz, *Sync: The Emerging Science of Spontaneous Order* (Hyperion, New York, 2003).

[9] E. Ott, C. Grebogi, and J. A. Yorke, Phys. Rev. Lett. **64**, 1196 (1990).

[10] K. Pyragas, Phys. Lett. **A 170**, 421 (1992).

[11] K. Pyragas, Phys. Rev. Lett. **86**, 2265 (2001).

[12] T. Shinbrot and F. J. Muzzio, Nature (London) **410**, 251 (2001).

[13] K. Wiesenfeld and F. Moss, Nature (London) **373**, 33 (1995).

[14] Y. Braiman, J. F. Lindner, and W. L. Ditto, Nature (London) **378**, 465 (1995).

[15] M. Weiss, T. Kottos, and T. Geisel, Phys. Rev. E **63**, 056211 (2001).

[16] F. Qi, Z. Hou, and H. Xin, Phys. Rev. Lett. **91**, 064102 (2003).

[17] A. Gavrielides, T. Kottos, V. Kovanis, and G. P. Tsironis, Phys. Rev. E **58**, 5529 (1998); Europhys. Lett. **44**, 559 (1998).

[18] The observed transition also occurs in other systems where the potential that governs the dynamics of a single oscillator is periodic. If, for instance, we choose a potential of the form $V(\theta) = -\alpha \cos^4(\theta/2)$ instead of the choice $V(\theta) = -mgl \cos(\theta)$ in Eq. (1), we obtain similar results for a suitable choice of the parameter α (data not shown).

[19] R. Ritz and T. J. Sejnowski, Curr. Opin. Neurobiol. **7**, 536 (1997).

[20] G. Buzsaki and A. Draguhn, Science **304**, 1926 (2004).

[21] S. Boccaletti, J. Kurths, G. Osipov, D. L. Valladares, and C. S. Zhou, Phys. Rep. **366**, 1 (2002).

[22] J. Kurths, S. Boccaletti, C. Grebogi, and Y.-C. Lai (Organizers), Focus Issue: *Control and Synchronization in Chaotic Dynamical Systems*, Chaos **13** (2003) 126.